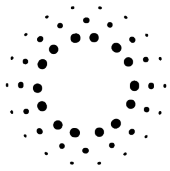

IFT - UNESP
INSTITUTO DE FÍSICA TEÓRICA

Masters Dissertation IFT–D.008/20

Prospects of a Search for Dark Higgs at CMS

Breno Orzari

Advisor

Thiago Rafael Fernandez Perez Tomei

June 2020

Orzari, Breno.
O79p Prospects of a search for dark Higgs at CMS / Breno Orzari. – São Paulo, 2020
105 f. : il.

Dissertação (mestrado) – Universidade Estadual Paulista (Unesp), Instituto de Física Teórica (IFT), São Paulo
Orientador: Thiago Rafael Fernandez Perez Tomei

1. Partículas (Física nuclear). 2. Matéria escura (Astronomia). 3. Aceleradores de partículas. I. Título

Sistema de geração automática de fichas catalográficas da Unesp. Biblioteca do Instituto de Física Teórica (IFT), São Paulo. Dados fornecidos pelo autor(a).

Dedico esta dissertação aos meus pais Marcia Candido e Wagner Gilberto Orzari

Agradecimentos

Primeiramente agradeço aos meus pais Marcia e Wagner, ao meu irmão Erick por todo apoio e confiança em minhas decisões, e por sempre me darem suporte e estarem ao meu lado nos momentos mais difíceis. Não poderia deixar de mencionar meu sobrinho Pedro, que me fez crescer como pessoa.

Agradeço à minha colega de profissão, namorada e melhor amiga Isabela pelas discussões sempre relevantes e pelo auxílio para superar mais essa etapa em minha vida. Também agradeço aos meus colegas Adriano e Gabriel pelos momentos de descontração e debates que sempre existirão apesar da distância.

Agradeço ao meu orientador Thiago Tomei por toda a ajuda profissional e pessoal que me proporcionou durante esses anos, e por ser quem me fez chegar onde estou.

Agradeço aos meus colegas de turma do IFT por todo o suporte e pelos momentos bons durante essa etapa. Em especial, gostaria de agradecer aos meus amigos: Andrei, Dean, Gabriel, Guilherme, João Paulo, Maria Gabriela, Mário, Otávio e Renato. Também gostaria de agradecer aos professores e ao pessoal técnico-administrativo do IFT.

Agradeço à todos do SPRACE e do NCC por todo o apoio nas mais diversas ocasiões. Em particular, gostaria de agradecer aos professores Eduardo, Pedro, Sandra e Sérgio cujos conselhos me guiaram na confecção deste trabalho. Agradeço também aos meus colegas do SPRACE: Ana Maria, César, Dener e Túlio por todos os bons momentos.

O presente trabalho foi realizado com o apoio da Coordenação de Aperfeiçoamento de Pessoal de Nível Superior – Brasil (CAPES) – Código de financiamento 001.

Agradeço à Fundação de Amparo à Pesquisa do Estado de São Paulo (FAPESP) pelo financiamento do projeto de pesquisa (processo n° 2018/01398-1, Fundação de Amparo à Pesquisa do Estado de São Paulo (FAPESP)), tornando possível a produção desta dissertação, e pela possibilidade de executar um projeto de pesquisa no CERN, no formato de BEPE, processo n° 2019/16401-0. As opiniões, hipóteses e conclusões ou recomendações expressas neste material são de responsabilidade do autor e não necessariamente refletem a visão da FAPESP.

"Nothing can make our life,
or the lives of other people,
more beautiful than
perpetual kindness."

Leo Tolstoy, *A Calendar of Wisdom.*

Resumo

Neste trabalho, um estudo sobre a viabilidade de uma busca por matéria escura no detector de partículas CMS é apresentado. O modelo de partícula de matéria escura escolhido é denominado modelo dark Higgs, que supõe a existência de três novos estados no setor escuro da matéria: um bóson vetorial massivo Z', um férmion de Majorana χ que deve ser o responsável pelos fenômenos de matéria escura observados atualmente, e um mediador análogo ao bóson de Higgs chamado dark Higgs (d_H) que é responsável pela geração dos termos de massa das outras duas partículas. O canal de decaimento mono-d_H foi o canal estudado, que é percebido como $\not{E}_T$ + jato gordo pelo detector CMS. Um conjunto de requerimentos de seleção retirados de outros trabalhos, junto de uma seleção alternativa na massa invariante do jato gordo foram aplicados em dados gerados por simulações de Monte Carlo, e o método de análise *cut and count* foi usado na obtenção de regiões de exclusão para diferentes conjuntos de parâmetros do modelo. Considerando dados do Run 2 do LHC (L = 150 fb^{-1}), que estão disponíveis para análise, valores de $m_{Z'}$ de até 2470 GeV, 2800 GeV e 2950 GeV podem ser sondados para m_{d_H} = 50 GeV, 70 GeV e 90 GeV, respectivamente. Valores de m_χ se estendendo até 490 GeV, 580 GeV e 600 GeV, para os mesmos valores de m_{d_H}, também podem ser explorados. Para as massas m_χ, $m_{Z'}$ fixadas em 200 GeV, 1000 GeV e 300 GeV, 1500 GeV, valores de m_{d_H} variando de 13 GeV a 178 GeV, e de 20 GeV a 174 GeV, respectivamente, podem ser explorados.

Palavras Chaves: Matéria Escura; Física de Partículas; Aceleradores de Partículas; Detectores de Partículas; Física além do Modelo Padrão.

Áreas do conhecimento: Física; Física de Partículas; Física de Altas Energias.

Abstract

In this work, a study about the feasibility of a search for dark matter particles at the CMS particle detector is presented. The dark matter particle model chosen is the dark Higgs model, which assumes three new states in the dark sector of matter: a heavy vector boson Z', a Majorana fermion χ that should be responsible for the dark matter phenomena observed nowadays, and a Higgs-like boson mediator called dark Higgs (d_H) that is responsible for generating the mass terms of the two other particles. The mono-d_H decay was the studied channel, which is perceived as $\not{E}_T$ + fat jet by the CMS detector. A set of selection requirements retrieved from other works along with an alternative selection requirement on the fat jet invariant mass were applied on Monte Carlo simulation generated data, and a cut and count analysis method was applied to obtain exclusion regions for different sets of model parameters. Concerning LHC Run 2 data (L = 150 fb^{-1}), which is already available for analysis, $m_{Z'}$ values up to 2470 GeV, 2800 GeV and 2950 GeV can be probed for m_{d_H} = 50 GeV, 70 GeV and 90 GeV, respectively. m_χ values extending to 490 GeV, 580 GeV and 600 GeV, for the same m_{d_H} values, may also be explored. For m_χ, $m_{Z'}$ masses fixed at 200 GeV, 1000 GeV and 300 GeV, 1500 GeV, m_{d_H} values ranging from 13 GeV to 178 GeV, and from 20 GeV to 174 GeV, respectively, may be explored.

Keywords: Dark Matter; Particle Physics; Particle Accelerators; Particle Detector; Beyond the Standard Model Physics.

Knowledge Areas: Physics; Particle Physics; High Energy Physics.

Contents

Chapter 1

Introduction

The search for new physics in particle colliders is a very active field nowadays. After the discovery of the Higgs boson that was the last elementary particle necessary to conclude the standard model of particles (SM), there are still some very intriguing phenomena that can not be described by the particles or the fundamental interactions of the SM.

Particle physicists and cosmologists have been worried by certain gravitational anomalies, which received the name of dark matter (DM), for the last decades. It receives this name because there are several evidences of some extra mass at very large spatial scales, such as galaxies and clusters of galaxies, which does not come from luminous matter, and very little is known about the source of this effect. One possibility is that this is caused by a new particle that is practically non-interacting with the SM.

Depending on how this DM-SM interaction occur, it is possible that it can be reproduced in High Energy Physics (HEP) experiments such as the Large Hadron Collider (LHC) and detected by modern particle detectors such as the Compact Muon Solenoid (CMS). The constant development of modern particle detectors is of extreme importance, not only for the discovery of new physics, but also for further studies and measurements of properties from the standard model constituents, and for the creation of new technologies for other knowledge areas.

Even though real data is the only way to confirm or disprove a given theory, Monte Carlo (MC) simulation of particle collisions and their interaction with particle detectors is of great importance to give an idea of what to expect when performing the analysis of real data. Data generated by this method can also simulate the signal left by the interaction of unknown particles with the detectors, and this allows the creation of an analysis method for these generated events. Using this procedure, a study about the dark Higgs model, one of the several

DM particle models that tries to predict the properties of the dark sector of matter, and the possibility of a search for its signal in the CMS detector was performed.

The structure of this work is as follows: in chapters 2, 3 and 4 there is a bibliographic review about the standard model of particles, particle colliders and accelerators (focusing on the CMS detector and the LHC), the dark matter phenomenon and the new physics model being explored. Chapters 5 and 6 describe how the MC data was generated and analyzed, and display the results obtained after checking the validity of the simulated data with other works. Finally, in chapter 7 there is a discussion and a brief conclusion about the analysis performed.

Chapter 2

Standard Model

So far, the standard model (SM) is one of the most successful theories of Modern Physics. Using the knowledge acquired in the development of this theory, it was possible to describe three of the four fundamental interactions known to date, and to predict the existence of more than half of the elementary particles known to this day.

Historical Context

The SM arises from successive successes and wrong turns in attempts to describe the fundamental interactions [1–3]. Important contributions came from the gauge symmetry present in quantum electrodynamics (QED) and from the usage of non-abelian gauge symmetry groups coming from strong interactions.

The ideas that gave rise to the SM began to emerge in the mid 50s with Fermi's 4-point interaction, which worked reasonably well in the smallest order of perturbation theory (dimensional analysis and unitarity violation show that this theory must break at a center of mass energy around 300 GeV), but had non-removable infinities at the next order of perturbation, even using the QED renormalization techniques, which appeared to work exceptionally well.

A second problem arose at the same time: perturbation theory could not be applied to residual strong interactions, even though these were renormalizable, because they are strong.

In this period, the physics community began to worry even more about understanding the symmetries of nature, specifically the approximate symmetries, being necessary to interpret them carefully. Approximate symmetries such as isospin (where neutrons and protons are considered to have the same mass), strangeness

number conservation (violated in weak interactions), and even space-time symmetries (parity - P, time reversal - T , charge conjugation - C) such as P, TP or CP, which would be approximate (CP) or even violated (P and TP) in weak interactions. Furthermore, in the early 60s, the $SU(3)$ symmetry of the so-called eightfold way was found to be only an approximation for hadrons.

Three ideas emerged in the 50s and 60s that changed the way of looking at the symmetries of nature and the growing number of hadrons discovered at the time. The first was the idea of applying local symmetries, or gauge symmetries, in quantum field theories such as QED, a quantum field theory with a $U(1)$ gauge symmetry. Yang and Mills in 1954 constructed a gauge theory based on the $SU(2)$ group, hoping that this would be the theory to best describe the residual strong interaction.

The quantization of non-abelian gauge theories (whose generators of the symmetry group do not commute) was extensively studied, but it was only in 1957-58 that these ideas began to be applied to the weak interaction, a period in which they determined that these were produced by coupling the fermions with vector bosons. Still, as gauge symmetries prohibit gauge bosons from acquiring mass, a mass term should be put into the theory, breaking the gauge symmetry, which would leave it non-renormalizable, returning to the problem of Fermi's 4-point interaction.

The second idea was the quarks model, developed in 1964 independently by Gell-Mann and Zweig. The model assumed that hadrons would be composed of other elementary particles, the quarks up (u), down (d) and strange (s), and it was crucial to classify the huge number of hadrons found in the 50s and 60s. A few years later, in 1968, in a deep inelastic scattering experiment carried out at the Stanford Linear Accelerator Center (SLAC), evidence of electrons being scattered away at large angles by nucleons began to emerge, analogous to the Rutherford's gold foil experiment in 1911, indicating a possible hadron substructure. The quark model was still questionable as these were not observed freely in nature.

The third and last idea, and particularly one of the most important ones, was that of spontaneous symmetry breaking, where Lagrangian symmetries would not be symmetries of the vacuum. In 1962, Goldstone, Salam and Weinberg proved

the Goldstone theorem (developed in 1961), showing that for every spontaneously broken symmetry there should be a massless and spin 0 particle, a Goldstone boson, something that did not exist, for example, in the strong interactions known at the time.

In 1964, Higgs and, independently, Englert and Brout, determined that Goldstone's theorem needed a different interpretation if the original symmetry was a gauge symmetry. The remaining Goldstone boson becomes the helicity 0 component of the gauge boson, which then acquires mass.

At first, these ideas were applied to strong interactions, which should have a broken $SU(2)_L \times SU(2)_R$ symmetry (usual isospin and chiral isospin acting on the left-handed and right-handed components of nucleons), which gave rise to the pions, the Goldstone bosons of these interactions. Because it is an approximate symmetry, the pions have a small mass.

Next, Weinberg, and Salam independently, developed what is called an electroweak theory, which can be seen as the first half of the SM. There should be a spontaneously broken gauge symmetry that leads to the vector bosons of weak interactions. There should also be some generator of the gauge group that would not be broken, that corresponded to a massless gauge boson, the photon.

At the time, Weinberg used only the leptons of the electron family (the left-handed electron and electron neutrino and the right-handed electron), which were to obey the group $SU(2)_L \times U(1)_Y$, something that was also done independently by Glashow in 1961 and Salam and Ward in 1964. The gauge bosons would then be the charged particles $W^{\pm}$, the neutral boson Z^0, all massive, and the null mass gauge boson, the photon.

The theory not only gave mass to the bosons of weak interactions, but also gave mass to the elementary SM fermions. In this model, the only scalar particles whose vacuum expectation value (vev) would give fermions masses should be a doublet under $SU(2)_L \times U(1)_Y$ with $+e$ and zero charges. In addition, a single doublet of complex scalar fields may be written in terms of four real fields. Three of the symmetries of $SU(2)_L \times U(1)_Y$ are broken and eliminate three Goldstone bosons associated with these fields, that is, there is still a massive scalar particle of

neutral electric charge, which would later be associated with the Higgs boson.

In 1972, t'Hooft and Veltman showed that non-abelian gauge theories with spontaneous symmetry breaking should be renormalizable, guaranteeing great predictive power to the electroweak model. However, experimental proof of the model was still needed, which was obtained in 1973 by the Gargamelle experiment at the European Organization for Nuclear Research (CERN), since the theory predicted neutral currents associated with the Z^0 boson and these were observed, supporting the theory.

The second half of the SM consists of quantum chromodynamics (QCD), a theory that describes the interaction between quarks and gluons. In 1973 Gross and Wilczek, and Politzer independently, showed that certain non-abelian gauge theories should have the property of asymptotic freedom, that is, the higher the energies of two particles interacting, the lower the intensity of the coupling constant, something that depends on the number of fermions in the theory and the possible charges of the interaction. As it was already known that there are three charges of color, it was reasonable to assume that the gauge group that acts in the strong interaction between quarks was $SU(3)_C$, a group of non-Abelian symmetry.

At about the same time, a mechanism emerges that suppresses the violation of strangeness in weak interactions. It was already known that charged semileptonic interactions violated the conservation of strangeness (S), that is, the W bosons should have couplings with changes of one unit in the strangeness ($\Delta S = 1$). With this, it should be possible, when exchanging pairs of W, that the variation in strangeness is two units ($\Delta S = 2$), generating processes such as $K \to \bar{K}$. These processes are observed in nature, but without a way to suppress their amplitude, a difference in the masses of K_1 and K_2 (mass eigenstates of K and $\bar{K}$) much higher than the one currently observed should be obtained.

The solution came from the GIM mechanism (proposed by Glashow, Iliopoulos and Maiani in 1970), which would disappear with these strangeness violations if there were two complete doublets of quarks. The fourth quark, called charm (c), was discovered in 1974 when its J/ψ bound state was observed experimentally independently by SLAC and the Brookhaven National Laboratory at the same time.

It was known that, in charged current weak interactions, the flavor of a quark could be changed to the flavor of another member of its family, and even to members of other families. In order to relate the mass eigenstates with the flavor eigenstates, the Cabibbo-Kobayashi-Maskawa matrix was developed, that was a 3×3 matrix that could be parameterized by three angles and a complex phase, where the latter allows the occurrence of CP violation in the Standard Model. This required the existence of a third family of quarks and leptons. The discoveries of τ (in 1975 by SLAC), of bottom (observation of its bound state Y in 1977 at Fermilab) and top quarks (in 1995 at Fermilab), and ν_τ (in the 2000s by the DONUT collaboration), the constituents of the third families of leptons and quarks, were crucial for the verification of the CP violation mechanism.

Finally, it remained to find a particle of the SM predicted since 1964: the Higgs boson. With its observation, the Standard Model and the spontaneous symmetry breaking and mass generation of elementary particles mechanisms would be consolidated. It was only in 2012 that CERN's ATLAS and CMS experiments observed a signal of a resonance with a mass of approximately 125 GeV. More accurate measurements of the mass, production and decay rates of this resonance, only made it clearer that the particle found was in fact the Higgs boson.

Standard Model Structure

The Standard Model (following the development in [2–5]) is a quantum field theory based on the $SU(3)_C \times SU(2)_L \times U(1)_Y$ symmetry group. It is made up of fermions (half-integer spin particles) and bosons (integer spin particles). Among the fermions, there are the three families of quarks (here denoted by u for positive electric charge quarks and d for negative electric charge quarks) and leptons (where the set of electrically neutral leptons will be denoted by ν and the set of electrically charged leptons will be denoted by ℓ) that are written as spinors. The families of leptons and quarks are divided into two components: left-handed (doublets under $SU(2)_L$) and right-handed (singlets under $SU(2)_L$). Each of these components has their respective representations under $U(1)_Y$, $SU(2)_L$ and $SU(3)_C$, shown in table 2.1 below.

In addition, the mediators of weak, strong and electromagnetic interactions are the $W^\pm$ and Z^0 bosons, the gluons (G), and the photons (γ), respectively, which

arise from the fact that the SM is a gauge theory. Finally, the Higgs boson is the only scalar particle in the theory (it has spin 0), and is responsible for the spontaneous symmetry breaking mechanism $SU(2)_L \times U(1)_Y \rightarrow U(1)_{EM}$, and for the generation of the weak interaction bosons and elementary fermions masses. The Higgs boson field also transforms as a $SU(2)_L$ doublet.

Table 2.1: Representation under $SU(3)_C$, $SU(2)_L$ and the respective hypercharge values of the Standard Model fields.

Field	$\begin{pmatrix} u \\ d \end{pmatrix}_L$	u_R	d_R	$\begin{pmatrix} \nu \\ \ell \end{pmatrix}_L$	ℓ_R	H
$SU(3)_C$	3	3	3	1	1	1
$SU(2)_L$	2	1	1	2	1	2
$U(1)_Y$	$1/6$	$2/3$	$-1/3$	$-1/2$	-1	$1/2$

Electroweak Gauge Theory

The expression for the charged current interaction was based on empirical observations. The interaction term in the Lagrangian was given by $J^{\mu}_{W} W_{\mu}$, with

$$J^{\mu}_{CC} = \overline{\psi}_{aL} \gamma^{\mu} \psi_{bL} = \psi^{\dagger}_{a} P_L \gamma^0 \gamma^{\mu} P_L \psi_b = \frac{1}{2} \overline{\psi}_a \left(\gamma^{\mu} - \gamma^{\mu} \gamma^5 \right) \psi_b, \tag{2.1}$$

where the current of this interaction only has left-handed fermionic fields (ψ_a and ψ_b), and W_{μ} is the field representing the mediators of this interaction. The fields ψ_a and ψ_b can be different particles (quarks or leptons of different flavors) with different electrical charges, the W mediators being responsible for carrying this electrical charge, as this must be preserved. Note also that this coupling is of the form $vector - pseudo\text{ - }vector$.

The idea is to build a Yang-Mills gauge theory, that contains the interaction term described above, the neutral current interactions and its gauge bosons. The group that was used to represent these interactions was $SU(2)_L \times U(1)_Y$ (the L index indicates that the $SU(2)$ group only acts on the left-handed components of fermions), which are independent transformations of isospin and a group $U(1)$ related to the hypercharge number Y. However, it is known that the z component

of isospin (T_3) is related to the electrical charge of the particles by

$$Q = T_3 + Y, \tag{2.2}$$

The Lagrangian that represents the interaction between fermions is given by

$$\mathcal{L} = \sum_f \overline{\psi}_f i\gamma^\mu D_\mu \psi_f, \tag{2.3}$$

where f runs over all elementary fermions, and, from the symmetry group and the definition of the covariant derivative in quantum field theory,

$$D_\mu = \partial_\mu - igT_i W_{i\mu} - ig'YB_\mu, \tag{2.4}$$

where $T_i = \frac{\sigma_i}{2}$, with σ_i being Pauli's matrices, the expression of 2.3 becomes

$$\begin{aligned}
&\sum_f \overline{\psi}_f i\gamma^\mu \left(\partial_\mu - ig\frac{\sigma_i}{2}W_{i\mu} - ig'YB_\mu\right)\psi_f = \\
&\begin{pmatrix} \nu_L^\dagger & \ell_L^\dagger \end{pmatrix} \gamma^0\gamma^\mu i \left(\partial_\mu - ig\frac{\sigma_i}{2}W_{i\mu} - ig'Y_L^\ell B_\mu\right) \begin{pmatrix} \nu_L \\ \ell_L \end{pmatrix} + (\ell_R^\dagger)\gamma^0\gamma^\mu i \left(\partial_\mu - ig'Y_R^\ell B_\mu\right)(\ell_R) + \\
&\begin{pmatrix} u_L^\dagger & d_L^\dagger \end{pmatrix} \gamma^0\gamma^\mu i \left(\partial_\mu - ig\frac{\sigma_i}{2}W_{i\mu} - ig'Y_L^q B_\mu\right) \begin{pmatrix} u_L \\ d_L \end{pmatrix} + (u_R^\dagger)\gamma^0\gamma^\mu i \left(\partial_\mu - ig'Y_R^u B_\mu\right)(u_R) + \\
&\qquad + (d_R^\dagger)\gamma^0\gamma^\mu i \left(\partial_\mu - ig'Y_R^d B_\mu\right)(d_R),
\end{aligned} \tag{2.5}$$

for all Standard Model fermions.

Three important properties are noticed from the above equation: the first is that the part containing $W_{i\mu}$ does not act on the right-handed components (as already seen above); the second is that ν_R has zero electric charge, zero mass (according to the Standard Model), and because it is right-handed it has $T_3 = 0$, that is, $Y = 0$, making it unable to interact with any particle of the SM, since it is not related to W_μ, B_μ or H; the third is that all terms in 2.5 are identical for leptons and quarks, which makes the weak interaction universal between them.

Using as an example only the left-handed leptons, and omitting the Dirac matrices [1], one can write

$$g' Y_L^\ell \left[\begin{pmatrix} \nu_L^\dagger & \ell_L^\dagger \end{pmatrix} \mathbb{1} \begin{pmatrix} \nu_L \\ \ell_L \end{pmatrix} \right] B_\mu + \frac{g}{2} \left[\begin{pmatrix} \nu_L^\dagger & \ell_L^\dagger \end{pmatrix} \begin{pmatrix} W_{3\mu} & W_{1\mu} - iW_{2\mu} \\ W_{1\mu} + iW_{2\mu} & -W_{3\mu} \end{pmatrix} \begin{pmatrix} \nu_L \\ \ell_L \end{pmatrix} \right], \tag{2.6}$$

where, defining $W^{\pm\dagger} = \frac{1}{\sqrt{2}} (W_1 \pm iW_2)$, it is possible to get

$$g' Y_L^\ell \left(\nu_L^\dagger \nu_L B_\mu + \ell_L^\dagger \ell_L B_\mu \right) + \frac{g}{2} \left(\nu_L^\dagger \nu_L W_{3\mu} - \ell_L^\dagger \ell_L W_{3\mu} + \sqrt{2} \nu_L^\dagger \ell_L W_\mu^{-\dagger} + \sqrt{2} \ell_L^\dagger \nu_L W_\mu^{+\dagger} \right), \tag{2.7}$$

where the third and fourth terms of the second parenthesis correspond to weak interactions of charged current. The operator $\nu_L^\dagger \nu_L$ is a current-neutral term that interacts with the gauge fields by

$$\nu_L^\dagger \nu_L \left(\frac{g}{2} W_{3\mu} + g' Y_L^\ell B_\mu \right). \tag{2.8}$$

Since neutrinos are not electrically charged, this is not an electromagnetic interaction. The linear combination of these gauge fields can be seen as a new weak interaction field, corresponding to the Z^0 boson. Using $Y_L^\ell = -\frac{1}{2}$ and writing the operator of the already normalized field (B_μ and $W_{i\mu}$ are orthogonal)

$$Z_\mu^0 = \frac{(gW_{3\mu} - g'B_\mu)}{\sqrt{g^2 + g'^2}}, \tag{2.9}$$

or, in a more convenient way

$$Z_\mu^0 = \cos\theta_W W_{3\mu} - \sin\theta_W B_\mu, \tag{2.10}$$

with $\cos\theta_W = \frac{g}{\sqrt{g^2+g'^2}}$ and $\sin\theta_W = \frac{g'}{\sqrt{g^2+g'^2}}$.

[1] All the Dirac matrices were omitted, and the fields were chosen as the dagger components $\psi^\dagger$, instead of the bar components $\overline{\psi}$

Notice that it is possible to find another linear combination of the gauge fields that corresponds to other mediator, which is orthogonal to the one obtained for Z^0_μ, and do not interact directly with neutrinos. This linear combination, that was correctly associated with the photon A_μ, is given by

$$A_\mu = \cos\theta_W W_{3\mu} + \sin\theta_W B_\mu = \frac{(gW_{3\mu} + g'B_\mu)}{\sqrt{g^2 + g'^2}}, \tag{2.11}$$

where it is possible to invert this relation and obtain

$$\begin{aligned} B^0_\mu &= \cos\theta_W A_\mu - \sin\theta_W Z^0_\mu, \\ W_{3\mu} &= \sin\theta_W A_\mu + \cos\theta_W Z^0_\mu. \end{aligned} \tag{2.12}$$

Using the relations developed above, already replacing $Y^\ell_L = -\frac{1}{2}$ and $Y^\ell_R = -1$, the couplings of the operators $\ell^\dagger_{L,R}\ell_{L,R}$ can be written as

$$\begin{aligned} \ell^\dagger_L\ell_L\left(-\frac{g}{2}W_{3\mu} - \frac{g'}{2}B_\mu\right) + \ell^\dagger_R\ell_R(-g'B_\mu) = \ell^\dagger_L\ell_L\left(A_\mu\frac{-gg'}{\sqrt{g^2+g'^2}} + Z^0_\mu\frac{g'^2-g^2}{\sqrt{g^2+g'^2}}\right) + \\ + \ell^\dagger_R\ell_R\left(A_\mu\frac{-gg'}{\sqrt{g^2+g'^2}} + Z^0_\mu\frac{g'^2}{\sqrt{g^2+g'^2}}\right), \end{aligned} \tag{2.13}$$

being possible to identify the coupling to the electromagnetic field

$$\frac{-gg'}{\sqrt{g^2+g'^2}} = -e, \tag{2.14}$$

since ℓ_R and ℓ_L couple with A_μ with the same intensity. g and g' can be written as

$$g = \frac{e}{\sin\theta_W},\ g' = \frac{e}{\cos\theta_W}. \tag{2.15}$$

To determine the coupling of quarks with the Z^0 boson, start from 2.5 taking into account only the terms that contain the gauge fields B_μ and $W_{3\mu}$. Alternatively, simply perform the replacement

$$gT_iW_{i\mu} + g'YB_\mu \to gT_3W_{3\mu} + g'YB_\mu, \tag{2.16}$$

which, using the definition $Y = Q - T_3$ and relations 2.12 and 2.15, gives

$$\frac{e}{\cos\theta_W \sin\theta_W}(T_3 - Q\sin^2\theta_W), \tag{2.17}$$

for every quark family.

The electroweak theory has successfully unified electromagnetic and weak interactions. However, no mass terms appear in this theory for the $W^{\pm}$ and Z^0 bosons, neither for the fermions of the SM, since they cannot be put by hand, which would violate gauge invariance. The solution to this problem is what is called spontaneous symmetry breaking.

Spontaneous Symmetry Breaking

The spontaneous symmetry breaking (SSB) mechanism arises from the need to break a gauge symmetry (so that the associated fields acquire mass), keeping the Lagrangian of the interaction invariant under this transformation. The gauge invariance is fundamental for the theory to be renormalizable, preserving the predictive power. Thus, an explicit symmetry breaking term does not solve this issue; the subtle alternative is SSB.

In the electroweak theory $SU(2)_L \times U(1)_Y$ the spontaneous symmetry breaking is performed by inserting a scalar field, whose vacuum state is not invariant under this symmetry, and which will be responsible for what is called the Higgs mechanism. This break in the gauge symmetry will keep electromagnetism $U(1)_{EM}$ intact, while giving mass to the Standard Model particles.

The Higgs field is written as a doublet under $SU(2)_L$, having the following scalar components

$$\phi = \begin{pmatrix} \phi^+ \\ \phi^0 \end{pmatrix}, \tag{2.18}$$

with $Y_H = \frac{1}{2}$. The Lagrangian of ϕ is given as

$$\mathcal{L}_\phi = (D^\mu\phi)^\dagger(D_\mu\phi) - \mu^2\phi^\dagger\phi - \lambda(\phi^\dagger\phi)^2, \tag{2.19}$$

where $\mu^2 < 0$ and $\lambda > 0$. These components can be written in terms of four real

fields as $\phi^+ = \frac{(\phi_1+i\phi_2)}{\sqrt{2}}$ and $\phi^0 = \frac{(\phi_3+i\phi_4)}{\sqrt{2}}$, and the Lagrangian will be

$$\mathcal{L}_\phi = \frac{1}{2}\sum_{i=1}^{4}(D^\mu\phi_i)(D_\mu\phi_i) - \frac{1}{2}\mu^2\sum_{i=1}^{4}\phi_i\phi_i - \frac{1}{4}\lambda\left(\sum_{i=1}^{4}\phi_i\phi_i\right)^2, \tag{2.20}$$

whose covariant derivative is

$$D_\mu = \partial_\mu - ig\left(\frac{\vec{\sigma}}{2}\cdot\vec{W}_\mu\right) - ig'YB_\mu. \tag{2.21}$$

The vevs of this system are given as

$$\left\langle 0|\phi^0|0\right\rangle = \sqrt{\frac{-\mu^2}{2\lambda}} = \frac{v}{\sqrt{2}},\ \langle 0|\phi^+|0\rangle = 0, \tag{2.22}$$

with $v = \sqrt{\frac{-\mu^2}{\lambda}}$. Choosing the gauge where $\phi_1 = \phi_2 = \phi_4 = 0$ and $\phi_3 = v + h(x)$, equation 2.18 becomes

$$\phi(x) = \frac{1}{\sqrt{2}}\begin{pmatrix} 0 \\ v + h(x) \end{pmatrix}, \tag{2.23}$$

which represents small disturbances of the electrically neutral component of ϕ around the vev, where $h(x)$ is the field that represents the Higgs boson. It is possible to show that ϕ_1, ϕ_2 and ϕ_4 are exactly the non-massive fields corresponding to the would-be Goldstone bosons. The mass terms of $W^\pm$ and Z^0 will arise from the interaction of ϕ with the gauge field terms of the covariant derivative like

$$(D^\mu\phi)^\dagger(D_\mu\phi) \to \left\{\left[ig\left(\frac{\vec{\sigma}}{2}\cdot\vec{W}_\mu\right) + ig'YB_\mu\right]\phi\right\}^\dagger\left\{\left[ig\left(\frac{\vec{\sigma}}{2}\cdot\vec{W}_\mu\right) + ig'YB_\mu\right]\phi\right\}. \tag{2.24}$$

Considering only the vev part of ϕ in 2.23 and the relations in 2.12, it can be shown that the mass terms will be

$$\frac{v^2g^2}{4}W^{+\mu\dagger}W^{-\dagger}_\mu + \frac{v^2g^2}{8\cos^2\theta_W}Z^{0\mu}Z^0_\mu, \tag{2.25}$$

that is, $M_W = \frac{1}{2}vg = M_Z\cos\theta_W$, and $M_A = 0$ that comes from $\langle 0|\phi^+|0\rangle = 0$. Besides that, using $\mu^2 = -\lambda v^2$ and substituting 2.23 in 2.19, the mass of the Higgs boson $M_h = \sqrt{2\lambda}v$ is obtained, where the experimentally measured value is $M_h = 125,18 \pm 0,16$ GeV [4].

The spontaneously broken electroweak theory has only four parameters: g, g', μ^2 and λ. These can be written in terms of three of the most accurately measured experimental parameters so far: α, G_F and M_Z [4], whose values are

$$M_Z = (91,1876 \pm 0,0021)\ \text{GeV};$$

$$G_F = (1,1663787 \pm 0,0000006) \times 10^{-5}\ \text{GeV}^{-2}; \tag{2.26}$$

$$\alpha^{-1} = 137,035999139 \pm 0,000000031.$$

From the weak interaction at low energies, it is possible to determine the following relation (the W propagator can be "shrunk" for a point interaction, Fermi's 4-point interaction)

$$\frac{g^2}{M_W^2 - q^2} \approx \frac{g^2}{M_W^2} = \frac{4\pi\alpha}{\sin^2\theta_W M_W^2} \equiv 4\sqrt{2}G_F, \tag{2.27}$$

and, from that,

$$v = \left(\sqrt{2}G_F\right)^{-\frac{1}{2}} = 246\ \text{GeV}, \tag{2.28}$$

then it is possible to determine λ and μ^2. Finally, the following relations can be obtained,

$$\theta_W = \frac{1}{2}\arcsin\left(\frac{2v\sqrt{\alpha\pi}}{M_Z}\right), g = \frac{2\sqrt{\alpha\pi}}{\sin\theta_W},\ g' = \frac{2\sqrt{\alpha\pi}}{\cos\theta_W}. \tag{2.29}$$

Fermions Masses

Notice that in 2.3 and, as will be seen later, in the QCD Lagrangian, there are no mass terms of the type $m_\psi\overline{\psi}\psi$ for the elementary fermions. This is because the representations of the left-handed and right-handed components under $SU(2)_L$ are distinct, that is, $m_\psi\overline{\psi}\psi = m_\psi(\overline{\psi_L}\psi_R + \overline{\psi_R}\psi_L)$ must not exist since such a term is not gauge invariant.

However, with the construction of the Higgs boson doublet, terms of that form can be constructed as

$$\mathcal{L}_Y = y_\psi[(\overline{\psi_L}\phi)\psi_R + \overline{\psi_R}(\phi^\dagger\psi_L)], \tag{2.30}$$

which are called Yukawa couplings. Using the leptons as an example, the expression 2.30 will be

$$\begin{pmatrix} \overline{\nu_L} & \overline{\ell_L} \end{pmatrix} \frac{1}{\sqrt{2}} \begin{pmatrix} 0 \\ v+h \end{pmatrix} \ell_R = \frac{1}{\sqrt{2}} \overline{\ell_L}(v+h)\ell_R,$$

$$\overline{\ell_R} \frac{1}{\sqrt{2}} \begin{pmatrix} 0 & v+h \end{pmatrix} \begin{pmatrix} \nu_L \\ \ell_L \end{pmatrix} = \frac{1}{\sqrt{2}} \overline{\ell_R}(v+h)\ell_L, \tag{2.31}$$

$$\mathcal{L}_Y^\ell = y_\ell \frac{v}{\sqrt{2}} [\overline{\ell_L}\ell_R + \overline{\ell_R}\ell_L] + y_\ell \frac{h}{\sqrt{2}} [\overline{\ell_L}\ell_R + \overline{\ell_R}\ell_L],$$

whose quadratic terms in the fields can be compared to $m_\psi(\overline{\psi_L}\psi_R + \overline{\psi_R}\psi_L)$, that is , $m_\ell = \frac{y_\ell v}{\sqrt{2}}$. The coupling constants y_ψ will be different for each flavor of each family of quarks and leptons of the SM, and can be adjusted based on experimental data.

CKM Matrix

Experimental data showed that in certain decays there was a violation of the strangeness number. An explanation for this phenomenon started to be developed in 1963 by Cabibbo, who discovered that the quark doublets that appear in the weak interaction are not mass eigenstates. At the time, he suggested that the u quark partner would be the $d' = d\cos\theta_C + s\sin\theta_C$ mixture, where θ_C is the mixing angle between the d and s quarks. Currently [4–6], using the matrix formalism, this phenomenon can be explained for the three families of quarks.

The Yukawa Lagrangian after spontaneous symmetry breaking is

$$\mathcal{L}_Y = -\left(1 + \frac{h}{v}\right)(\overline{d'_L} \cdot M_d \cdot d'_R + \overline{u'_L} \cdot M_u \cdot u'_R + \overline{\ell'_L} \cdot M_\ell \cdot \ell'_R + h.c.), \tag{2.32}$$

where M_f are complex non-diagonal mass matrices that are related to the coupling constants y_f as $[M_d, M_u, M_\ell]_{jk} = [y^d_{jk}, y^u_{jk}, y^\ell_{jk}]\frac{v}{\sqrt{2}}$, that can be diagonalized and the fields can be redefined to give rise to the mixing of families. The Yukawa Lagrangian will then be

$$\mathcal{L}_Y = -\left(1 + \frac{h}{v}\right)(\overline{d} \cdot \mathcal{M}_d \cdot d + \overline{u} \cdot \mathcal{M}_u \cdot u + \overline{\ell} \cdot \mathcal{M}_\ell \cdot \ell), \tag{2.33}$$

where $\mathcal{M}_d = \text{diag}(m_d, m_s, m_b)$, $\mathcal{M}_u = \text{diag}(m_u, m_c, m_t)$ and $\mathcal{M}_\ell = \text{diag}(m_e, m_\mu, m_\tau)$. This redefinition of eigenstates leads to changes in other terms of the SM Lagrangian. The most important changes are related to the neutral current ($\mathcal{L}_{CN}$) and charged current ($\mathcal{L}_{CC}$) terms of weak interactions

$$\overline{f'}_{L(R)} f'_{L(R)} = \overline{f}_{L(R)} f_{L(R)} \rightarrow \mathcal{L}'_{CN} = \mathcal{L}_{CN} \tag{2.34}$$

$$\overline{u'_L} d'_L = \overline{u_L} \cdot V_{CKM} \cdot d_L \ \rightarrow \ \mathcal{L}'_{CC} \neq \mathcal{L}_{CC} \tag{2.35}$$

After redefining the eigenstates, the neutral current terms remain the same. This mechanism was given the name GIM (Glashow-Iliopoulos-Maiani), in which there is no change in the flavor of quarks that participate in couplings with the Z^0 boson. This mechanism is what suppresses the amplitude of some processes that are impossible at tree level, such as $K_L(s\bar{d}) \rightarrow Z^0 \rightarrow \mu^+\mu^-$ (since the vertex $Z^0 s\bar{d}$ does not exist), but happen at the one-loop order through the exchange of two W bosons, which are suppressed because of the mixing between the quark families. Regarding the charged current term, there is the emergence of the V_{CKM} matrix that mixes the quarks of the down type, allowing interactions with flavor changes.

Firstly developed by Cabibbo-Kobayashi-Maskawa, V_{CKM} is a complex unitary 3×3 matrix (due to $N_f = 3$ families of quarks), which must have $N_f^2 = 9$ free parameters, being $\frac{1}{2}N_f(N_f - 1) = 3$ modules and $\frac{1}{2}N_f(N_f + 1) = 6$ phases. However, there are physically redundant phases that can be redefined, leaving only $\frac{1}{2}(N_f - 1)(N_f - 2) = 1$ independent phase to be considered. Defining the 3 independent modules as a function of 3 angles θ_{12}, θ_{13} and θ_{23}, and denoting δ_{13}, as the independent phase, and $s_{ij} \equiv \sin\theta_{ij}$ and $c_{ij} \equiv \cos\theta_{ij}$, the V_{CKM} matrix has the following parameterization

$$V_{CKM} = \begin{pmatrix} c_{12}c_{13} & s_{12}c_{13} & s_{13}e^{-i\delta_{13}} \\ -s_{12}c_{23} - c_{12}s_{23}s_{13}e^{i\delta_{13}} & c_{12}c_{23} - s_{12}s_{23}s_{13}e^{i\delta_{13}} & s_{23}c_{13} \\ s_{12}s_{23} - c_{12}c_{23}s_{13}e^{i\delta_{13}} & -c_{12}s_{23} - s_{12}c_{23}s_{13}e^{i\delta_{13}} & c_{23}c_{13} \end{pmatrix}. \tag{2.36}$$

Another useful parameterization is written in terms of the Wolfenstein param-

eters $s_{12} \equiv \lambda$, $s_{23} \equiv A\lambda^2$ and $s_{13} \equiv A\lambda^3(\rho - i\eta)$, as

$$V_{CKM} = \begin{pmatrix} 1 - \frac{\lambda^2}{2} & \lambda & A\lambda^3(\rho - i\eta) \\ -\lambda & 1 - \frac{\lambda^2}{2} & A\lambda^2 \\ A\lambda^3(1 - \rho - i\eta) & -A\lambda^2 & 1 \end{pmatrix} + O(\lambda^4). \tag{2.37}$$

The most recent results [4] provide the following values for the V_{CKM} elements

$$V_{CKM} = \begin{pmatrix} 0.97420 \pm 0.00021 & 0.2243 \pm 0.0005 & 0.00394 \pm 0.00036 \\ 0.218 \pm 0.004 & 0.997 \pm 0.017 & 0.0422 \pm 0.0008 \\ 0.0081 \pm 0.0005 & 0.0394 \pm 0.0023 & 1.019 \pm 0.025 \end{pmatrix}.$$

Strong Interactions Gauge Theory

The Standard Model also comprises the strong interactions between quarks and gluons, described by quantum chromodynamics. QCD is a non-abelian gauge theory based on the group $SU(3)_C$, where the subscript C denotes that the charges of interactions governed by this theory are the color charges of the particles. In the adjoint representation of $SU(3)_C$ there are eight generators, which are identified with the gluons (mediators of strong interactions).

As a non-abelian gauge theory, the gauge field intensity tensor will be given by

$$F^i_{\mu\nu} = \partial_\mu G^i_\nu - \partial_\nu G^i_\mu - g_s c_{ijk} G^j_\mu G^k_\nu;\ i = 1, ..., 8, \tag{2.38}$$

where G^i_μ are representations of gluons, g_s is the coupling constant for strong interactions and c_{ijk} are the structure constants defined by $[\lambda_i, \lambda_j] = 2ic_{ijk}\lambda_k$, where λ_i are the Gell-Mann matrices. Using 2.38 it is simple to construct the term in the Lagrangian that describes the gauge fields, which will be given as

$$\mathcal{L}_{QCD} \sim \sum_{i=1}^{8} F^{i\mu\nu} F^i_{\mu\nu} = \sum_{i=1}^{8} (\partial^\mu G^{i\nu} - \partial^\nu G^{i\mu} - g_s c_{ijk} G^{j\mu} G^{k\nu})(\partial_\mu G^i_\nu - \partial_\nu G^i_\mu - g_s c_{ijk} G^j_\mu G^k_\nu). \tag{2.39}$$

Expression 2.39 shows the appearance of couplings between three or four

gluons

$$g_s c_{ijk}(\partial_\mu G^i_\nu - \partial_\nu G^i_\mu)G^{j\mu}G^{k\nu}, \qquad g_s^2 c_{ijk}c_{ilm}(G^{j\mu}G^{k\nu}G^l_\mu G^m_\nu), \tag{2.40}$$

which make the theory much more complex, since gluons also have a color charge. Adding the quark term to $\mathcal{L}_{QCD}$, you get

$$\mathcal{L}_{QCD} = -\frac{1}{4}F^{i\mu\nu}F^i_{\mu\nu} + \sum_q \overline{\psi}_q(i\not{D} - m_q)\psi_q, \tag{2.41}$$

whose covariant derivative is defined by $D_\mu \equiv \left(\partial_\mu + ig_s\frac{\lambda^i}{2}G^i_\mu\right)$, and that, in the second term of 2.41, introduces the coupling of quarks to gluons, in which the color of the quark must be changed.

So far, free quarks have not been observed in nature, and it was only possible to know about its existence due to deep inelastic scattering experiments. The explanation for this phenomenon is found in the renormalization method developed at QED, which generated several interesting ideas. One is that the coupling constant for fundamental interactions should change with the energy scale μ^2 of the process in question.

Defining the coupling constant as $\alpha_s \equiv \frac{g_s^2}{\hbar c}$ for the strong interactions, the function that calculates the variation of α_s with the energy scale μ^2 is known as the beta function. For QCD at 1 loop, the beta function is

$$\beta(\alpha_s) = \frac{\partial\alpha_s}{\partial\log\mu^2} = \frac{\alpha_s^2}{12\pi}(2n_f - 11n_c). \tag{2.42}$$

Since n_f is the number of quarks flavors and n_c is the number of existing color charges of the Standard Model (6 and 3, respectively), $\beta(\alpha_s)$ is a negative function. At high energies (consequently at short distances), the constant α_s is very small and quarks and gluons are loosely coupled. However, at the low energy limit, α_s grows, strongly coupling quarks and gluons, and it is possible to imagine that this is what that gives rise to the confinement of quarks and gluons within hadrons.

Color confinement also gives rise to hadronic jets in a particle collision. A hadronic jet [7, 8] is a spray of particles that are collimated in a given region of

space. They arise from the hadronization of single quarks or gluons, that is, since these particles have a net color charge, they cannot be seen alone in nature and come together to form hadrons with neutral color charge. This type of HEP object had the main role in the discovery of the gluon, the top quark and several Standard Model measurements.

Standard Model Successes and Problems

A lot of new ideas arose from the construction of the standard model. Very important mathematical concepts were developed throughout many years such as the spontaneous symmetry breaking mechanism and the proof of the application possibility of renormalization on non-abelian gauge theories, that granted great predictive power to the model. A few of the most remarkable predictions were the existence of weak bosons, the Higgs boson and the definition of their masses, the necessity of quarks flavor mixture and the heavy quarks, among many others.

On the other hand, there are several phenomena that the SM cannot explain. Just to mention some of them, the neutrinos in the standard model have zero masses, which, in the last decades, was proven to be a wrong statement; it does not have a mechanism that describes the matter-antimatter asymmetry in the universe; the fermions family structure and their mass difference is also not explained; one of the greatest issues concerning quantum corrections is the Higgs boson mass fine tuning problem and the lack of clues on how to solve it; the existence of an invisible type of matter in the universe that can not be explained by any of the SM particles, etc. This work focus on this last issue, also referred to as the dark matter (DM) problem.

One way to experimentally search for answers to those questions, is through very high energy collisions of subatomic particles, as they can probe the fundamental interactions at a very small distance scale. High energy particle collisions were also crucial to verify a great amount of SM calculations, and to experimentally observe more than half of the SM predicted particles. The observation of interactions between particles is only possible through the detection of its final states, since they usually happen in extremely short time periods. Currently, particle collisions are made using particle accelerators, such as the Large Hadron Collider (LHC),

and are detected by particle detectors, such as one of the LHC's experiments, the Compact Muon Solenoid (CMS) detector, that are described in the next chapter.

Chapter 3

The CMS Experiment

The development of particle accelerators was essential for the study of elementary particles and their interactions. The great majority of the SM particles were observed using such machines. Not only it was necessary to achieve ever greater energies to produce more massive particles, but also to develop particle detectors that were capable to detect, reconstruct and analyze the particles produced in high energy collisions in a reasonable amount of time.

Currently the largest particle accelerator in the world is located at CERN. The Large Hadron Collider (LHC) [9] is a high energy particle collision ring with a 27 km circumference. In proton-proton collisions (pp), the highest center of mass energy achieved so far is $\sqrt{s} = 13$ TeV, and it was designed to achieve a peak instantaneous luminosity of $\sim 10^{34}$ cm^{-2} s^{-1} for beams of 2808 bunches with $\sim 10^{11}$ protons each.

The particles are accelerated using eight radio frequency superconducting cavities (per beam) that provides 2 MV accelerating voltage per particle passage. At a revolution frequency of approximately 11245 kHz, this corresponds to 0.18 TeV/s, and, in theory, only 33.3 s is needed to achieve the 13 TeV energy in pp collisions. In practice, this time period happens to be around 20 minutes because a very compact beam is more important than its energy, and not 100% of the 2 MV affect the protons.

The LHC ring is composed of 1232 main dipoles cooled at approximately 2 K, making them superconductors and capable of producing magnetic fields with more than 8 T to bend the particle beams. Besides that, 474 main quadrupoles focus the beams, and almost 8000 auxiliary magnets are used for the beams corrections (also cooled at ~ 2 K).

Along with the powerful magnets to bend the particles trajectories and focus the bunches, an extremely good vacuum system (called beam vacuum) is needed to clear their path inside the beam pipe. In the absence of any leaks and at cryogenic temperatures, the pressure will stabilize around 10^{-6} mbar, that is, $\sim 10^{-9}$ times the atmospheric pressure.

It has four main experiments: ALICE (A Large Ion Collider Experiment) [10], ATLAS (A Toroidal LHC AparatuS) [11], CMS (Compact Muon Solenoid) [12] and LHCb (Large Hadron Collider beauty) [13]. LHCb and ALICE are detectors with a specific purpose, that is, they were built for the analysis of B hadrons physics and heavy-ion collisions, respectively. ATLAS and CMS are general-purpose detectors and have the ability to detect, directly or indirectly, all SM particles.

The CMS Detector

CMS [12] is a cylindrical, general-purpose detector that has 15 m in diameter and is 21 m long, capable of generating a constant 3.8 T magnetic field in its center. It weighs approximately 14000 tons due to the need for enormous field return yokes to contain the return of the very high magnetic field.

Its construction was planned aiming at the resistance of the subdetectors to its extreme operating conditions, such as the high uniform magnetic field, the high radiation rate (40 million pp collisions at high energies per second generate billions of particles), and also to increase the cost-benefit ratio of each subdetector.

This experiment can be divided into four main subdetectors: the tracker, the electromagnetic (ECAL) and hadronic (HCAL) calorimeters and the muon system. Each one has a specific purpose and its development was carried out seeking excellence in the collection and precision of experimental data. In figure 3.1 there is a scheme of the CMS detector with some of its subdetectors, and the superconducting solenoid.

Tracker

The tracker (figure 3.2), as the name implies, is a silicon detector that tracks the passage of charged particles. It can be divided into two other subsections, inner

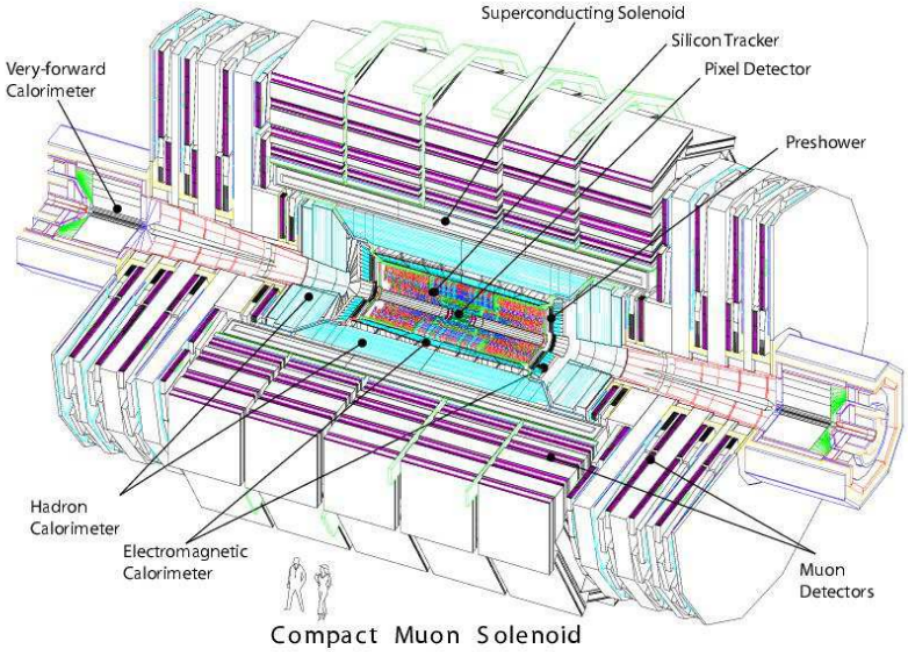

Figure 3.1: Scheme of the CMS detector showing each of its subdetectors. Retrieved from [14].

tracker (based on silicon pixels) and outer tracker (based on silicon microstrips). Both subsections are based on the same detection principle: a bias voltage is applied to a doped silicon sensor such that, if a charged particle traverses the material, it will produce electron-hole pairs that will be attracted to the cathode and anode, respectively, generating an electric current that is measured.

The choice of two subsections is due to the need of high granularity in the region closest to the Interaction Point (IP), that is, greater precision in the reconstruction of charged particles features and particle production vertices, while minimizing the cost of materials.

The pixels are divided into two regions around the IP: the barrel (BPix) that are four concentric cylinders centered on z and r - ϕ with respect to the IP (which is at the origin of the axis r, ϕ, z) and the endcaps (FPix) that are the "lids" of the detector, or rather three concentric disks on each side of the detector located at specific distances on the z axis. The pixel region covers a pseudo-rapidity of $|\eta| < 2.5$. This information takes into account the Phase I Pixel Detector Upgrade [16] (figure 3.3).

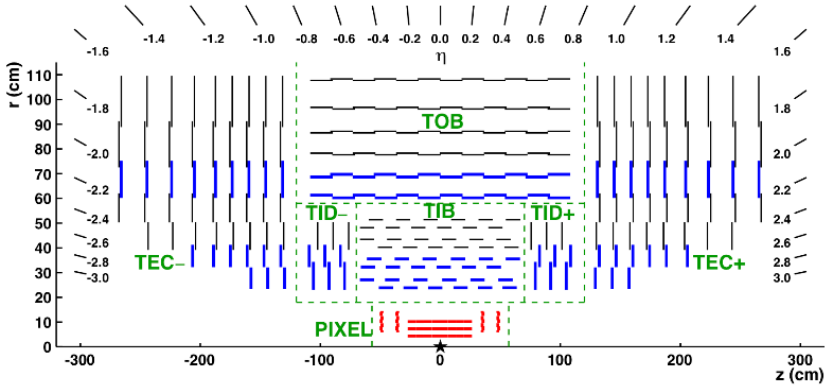

Figure 3.2: Diagram of the CMS detector tracker, showing the sections of the pixels and strips, before the Phase I Pixel Detector Upgrade (there were only three concentric cylinders in the pixels tracker). Taken from [15].

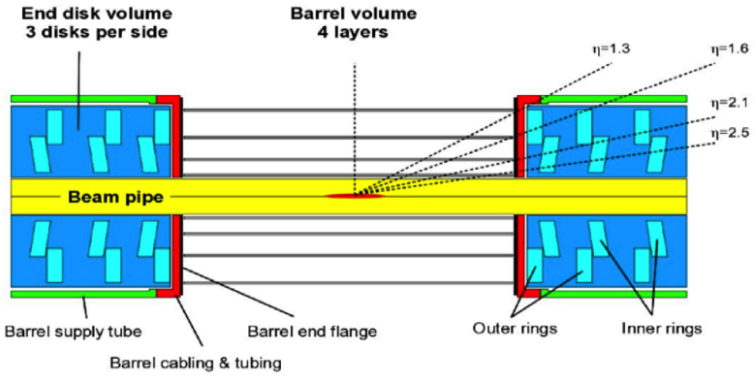

Figure 3.3: Pixel tracker after the Phase I Pixel Detector Upgrade. Retrieved from [16].

Each pixel has an area of 100 μm $\times$ 150 μm, and a thickness of 320 μm. This guarantees a spatial resolution of 15 μm - 20 μm in the measurement of the position of a charged particle when all hits on the detector are combined. The choice of silicon was due to the need for high granularity, high resistance to radiation and excellent operational capacity in regions with high magnetic fields (mainly for endcaps that are perpendicular to the solenoid magnetic field), and it is an easy material for industries to manipulate at the microscopic scale.

In the case of strips, there are 4 regions surrounding the IP and the pixels: the inner barrel (TIB; 4 concentric cylinders), the inner discs (TID; 3 concentric discs in

each side of the detector, whose position is symmetrical in relation to z = 0), the outer barrel (TOB; 6 concentric cylinders) and endcaps (TEC; 9 concentric disks in each side of the detector).

Since the granularity of this subsection does not have to be as high (due to the pixels) and the reduction in material costs must also be taken into account, micro-strips were used, that is, silicon bands for charged particles detection with dimensions of 10 cm $\times$ 80 μm in the inner region and 25 cm $\times$ 180 μm in the outer region. This subsection also covers a pseudo-rapidity of $|\eta| < 2.5$.

In addition, the entire tracker must have its temperature controlled with high precision for better functioning of silicon sensors and electronic components, high resolution in spatial measurements (due to the variation in the dimension of the subdetector with variations in temperature) and control of the influence of the incident radiation on the components.

Electromagnetic Calorimeter

The second subdetector is ECAL (figure 3.4) whose function is to measure the energy of electrons, positrons and photons that fly into it. An electromagnetic calorimeter should be a detector with high electromagnetic interaction capacity, high resistance to radiation, good accuracy on the measurement of the signals received to determine the incident particle energy and low response time. Particularly, the ECAL also needs good performance in the 3.8 T magnetic field region, since it is inside the CMS solenoid.

It is made of approximately 80000 crystals of $PbWO_4$ that have high density (8.28 g/cm^3) and a radiation length of 8.9 mm; Molière radius of 22 mm, that is, the showers of electromagnetic particles will be "contained" within that region; they are resistant to radiation, because even with darkening due to the time of exposure to radiation, this effect can be calibrated; and have a scintillation time of approximately 25 ns (which is not affected by the darkening of the crystal). A key characteristic of these crystals is that they are transparent to their own scintillation light.

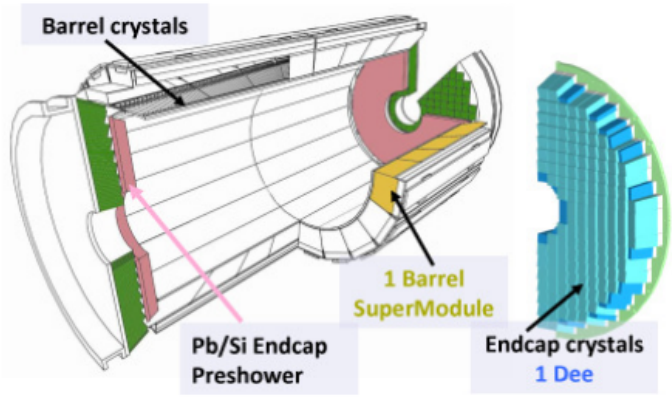

Figure 3.4: ECAL scheme. The crystals are assembled in modules that are then allocated in the barrel and in the endcaps. The CMS preshower detector is also shown in the image. Retrieved from [17].

The measurement of photons and electrons (positrons) energy is based on the scintillation of crystals. When a charged particle, such as the electron (positron), interacts with the medium, electromagnetic interaction processes such as Bremsstrahlung, Cherenkov radiation, Moller scattering, etc., emit a photon and another electron (positron) which ends up interacting again generating several other particles. In the case of photons, the production of electron-positron pairs, Compton scattering and the photoelectric effect are the processes responsible for generating a shower of other particles. The intensity of the signal generated by the shower of generated particles is proportional to the energy of the incident particle.

ECAL crystals are divided into 2 regions: the barrel (EB), where the crystals are arranged radially with respect to the IP, with a certain inclination depending on the pseudo-rapidity; and the endcaps (EE), where the crystals that are closest to the IP (high pseudo-rapidity) are almost parallel to the beam axis and the others (as the pseudo-rapidity decreases) have an angle with the z axis that depends on $|\eta|$. The barrel covers a region of $|\eta| < 1{,}479$ and has trapezoidal crystals of 230 mm in length whose face closer to the IP measures 22 mm $\times$ 22 mm and the distant face measures 26 mm $\times$ 26 mm. Endcaps cover a region of $1{,}479 < |\eta| < 3.0$ and has crystals of the same shape as the barrel, but with 220 mm in length, and the faces closest and farthest from the IP have sizes of 28.62 mm $\times$ 28.62 mm and 30 mm $\times$ 30 mm, respectively.

An avalanche photodiode is placed on the face of the crystal that is farthest from the IP, which absorbs the particles generated by the interaction of the incident particle, turns that pulse into an electrical signal, amplifies that signal and sends it to be analyzed. In the endcaps, due to the high inhomogeneity of the magnetic field, the devices used for this function are vacuum phototriodes, that behave satisfactorily under such conditions.

In addition, the CMS preshower detector is part of ECAL. This detector, located in the endcaps, covers a region of $1,653 < |\eta| < 2.6$ and has the purpose of detecting neutral pions, whose most likely decay product is two photons.

In the case of ECAL, temperature control is also of importance. The gain of photodiodes and phototriodes depends on the operating temperature and small variations in temperature generate large variations in the measured energy. To optimize the resolution of the subdetector, the temperature must be maintained at $18.00\,^{\circ}\mathrm{C} \pm 0.05\,^{\circ}\mathrm{C}$.

Hadronic Calorimeter

The HCAL (figure 3.5) is separated into four regions: the barrel (HB), the endcaps (HE), the outer calorimeter (HO) and the forward calorimeter (HF). All of them have the purpose of measuring the energy deposited by hadronic jets, the difference is in its location and the type of absorbing and active medium used (due to the amount of radiation received by the HF, for example).

The regions consist of an absorbent medium (brass and steel plates) and an active medium (plastic scintillators in the case of HB and HO and quartz-based scintillators in the case of HEs and HFs) merged. Steel plates are the first and the last component of each region, then there are the brass plates with the respective active medium between them. As an example, in HB are, in order of closest to the furthest plate to the IP: a 40 mm thick steel plate, 14 brass plates with thicknesses of 50.5 mm for the first 8 and 56.5 mm for the last 6 with the active medium (plastic scintillator) between them, and another steel plate with 75 mm thick.

The absorbing medium is used to guarantee the interaction of incident hadrons within the detector (approximately 10 interaction lengths λ_I in all HCAL regions),

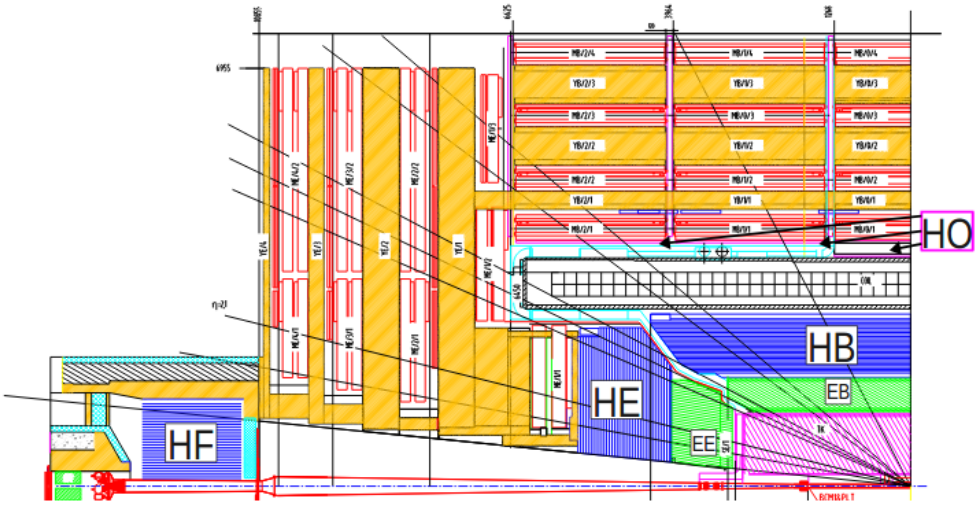

Figure 3.5: HCAL scheme showing each of its sections. The colors indicate the CMS subdetectors (blue for the HCAL regions, green for ECAL, pink for tracker, red and orange for muon system). Retrieved from [18].

generating a jet of other hadronic and electromagnetic particles that, in contact with the active medium, emit a rapid light pulse (fluorescence or Cherenkov light, depending on the active medium), and can be detected by photosensitive devices called hybrid photodiodes (changed to silicon photomultipliers in the Phase 1 Upgrade of the HCAL [18]). Similar to the ECAL, the intensity of the detected signal is a function of the energy of the incident particle.

Each HCAL region covers different pseudo-rapidity values, and this is what dictates the absorbent and active medium to be used. The greater the pseudo-rapidity, the greater the incident radiation on HCAL components. Furthermore, in the high $|\eta|$ regions the magnetic field becomes highly non-uniform. For these reasons absorbers are used with a specific brass alloy and quartz scintillators in HFs and HEs, which are more tolerant to radiation, in contrast to plastic scintillators that have moderated tolerance, and are capable of operating without major influences from the magnetic field. All HCAL regions cover a total region of $|\eta| < 5$, where HB reaches $|\eta| < 1.3$, HO also covers $|\eta| < 1.3$, HEs reach $1.3 < |\eta| < 3$ and HFs cover $3 < |\eta| < 5$ (very high incident radiation on them).

In the region up to $|\eta| = 1.3$, EB and HB are still not enough to detect all the hadronic jets, and the development of another calorimeter to stop these jets was necessary. The HO is placed after the first iron wall necessary for the return of the

magnetic field. This wall helps containment of hadrons and the development of showers that will be detected by the HO.

The calorimetry system (ECAL+HCAL) was designed to stop almost every product of a particle collision, with the exception of muons and neutrinos, and to be hermetic, that is, to cover as much of the area around the IP as possible .

Muons System

The CMS experiment was specially developed to detect events containing muons by using another spectrometer. Since it is after the calorimeters, it is expected that only muons will leave its footprints in this subdetector. The CMS muon detection system (figure 3.6) must have a low response time, high capacity to detect, recognize and reproduce the trajectories and vertices of muons, also allowing accurate measurements of the muon momentum. Besides that, because it has a huge active detection area (approximately 25,000 m^2), its components should be inexpensive, but still extremely reliable.

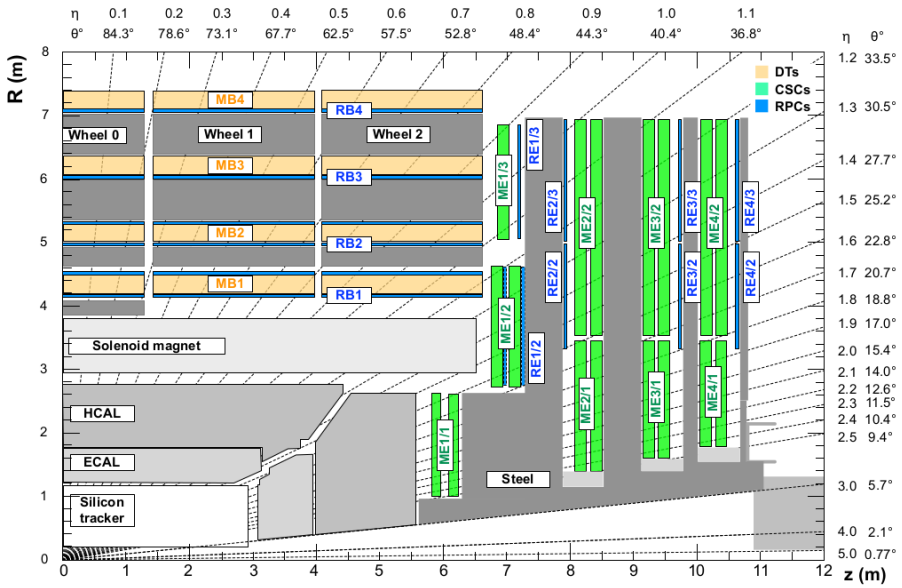

Figure 3.6: Quarter view of the muon detection system. The types of detectors are separated by color: DTs - yellow; CSCs - green; and RPCs - blue. Also indicated are length, radius and some pseudo-rapidity values. Retrieved from [19].

The muon system consists of three types of detectors based on the same detection principle: drift tubes (DT), which provide position measurements with high resolution; cathode strip chambers (CSC), which measure the position of charged particles and are able to operate in regions with a high and non-uniform magnetic field; and resistive plate chambers (RPC), which are able to recognize muon events at a very high rate (faster than 25 ns). With all these three systems working together, it is possible to quickly guarantee the recognition of muon events and accurately measure their position and momentum.

The detection of muons is done as follows by the three types of detectors: a certain gas mixture (that mixture differs for each one) is ionized through the passage of a muon whose energy is greater or equal than that of a MIP. Cathodes and anodes with high and very specific potential differences are used to generate an electric field (in some cases electrodes are also used for the containment of this electric field and to prevent the generation of electrical discharges), causing the positive ion to be attracted to the cathode and the electron to be attracted to the anode, generating an electrical signal capable of recognizing events with muons and measuring their position.

All systems have some subtle differences, including changes in granularity and the way they are assembled, for example, the RPCs were developed with a double chamber detection system, which optimizes its operation at the necessary high rates.

DTs and RPCs are merged around the IP, parallel to the beam in the form of barrels, and the CSCs are arranged like the detector endcaps. DTs cover a region of $|\eta| < 1.2$; the CSCs cover $0.9 < |\eta| < 2.4$; and RPCs cover $|\eta| < 1.6$ allowing high resolution on detection of muons at almost any solid angle.

The Trigger System

In the LHC's CMS experiment, the first stage where events begin to be selected receives the name of trigger [20]. Normally, the beams inside the LHC cross at a rate of 40 MHz, and, depending on the luminosity, more than one pp collision occurs at each crossing. Given the huge amount of data produced by the collisions, not all of it can be stored, and some selection must be performed. The trigger

system was developed to select only the events of interest among all the produced events.

The trigger can be divided into two steps: the Level 1 Trigger (L1T) and the High Level trigger (HLT). The L1T is a set of selections applied directly to the detector (hardware), where the data is collected after the event and immediately afterwards the L1T comes into action. It was designed to reduce the 40 MHz event rate to less than 100 kHz, and takes at most 4 μs to process each event.

Its selection is made by finding e/γ and jets candidates, using information from the ECAL and the HCAL and muon candidates from the muon system information. In the case of the e/γ, an variable that is associated with its isolation is provided, and the muon candidates pass through a track finding algorithm in this stage. The output of an event that passed the trigger is the candidates information and several global variables that are also calculated. Different selections can be performed at this stage, depending on the type of physics to be studied.

After the L1 trigger, there is still a large number of events to be discarded, and a second trigger is necessary. The HLT is performed by computer algorithms (software) after the selections made by the L1T. Its goal is to reduce the event rate of 100 kHz to less than 1 kHz. The events processing is performed by 13000 CPUs at an average of 200 ms processing time per event. As in the L1T, different selection algorithms are used depending on the events of interest wanted.

Chapter 4

Dark Matter

Even though the SM is one of the most successful theories of science, and it has the capability to describe the dynamics of every known subatomic particle and almost all interactions between them, there are some phenomena that it can not characterize. One of them is the "missing" matter in the universe, also known as dark matter (DM).

We know the amount of DM that exists in the universe, globally speaking, and in some specific regions, as in dwarf galaxies. We also know that, in addition to gravitationally, DM can possibly interact weakly, or not interact at all with SM particles, and that it must be stable on cosmological time scales. In this chapter there is a review of the evidences for DM, based on their chronological appearance as described in [21], that provided the clues for these properties, some ideas of how to detect this dark matter, and why no SM candidate fits as a DM particle.

Evidences and Properties

The first evidence (following the approach in [22]) comes in 1930 with the astronomer Fritz Zwicky, who, when applying the virial theorem to the movement of galaxies (at the time called nebulae) in clusters of galaxies, realized that the luminous matter present in the clusters did not correspond to the total mass of the cluster, but only a fraction. The virial theorem is obtained by studying the equations of motion of a galaxy i of mass M_i at a distance r_i:

$$\vec{r}_i \cdot \left(M_i \frac{d^2\vec{r}_i}{dt^2} = \vec{F}_i \right) \rightarrow \frac{1}{2}\frac{d^2(M_i r_i^2)}{dt^2} - M_i \left(\frac{dr_i}{dt}\right)^2 = \vec{r}_i \cdot \vec{F}_i. \tag{4.1}$$

Summing over all the galaxies in the cluster, and defining $\Theta \equiv \sum_i M_i r_i^2$ (polar moment of inertia), $Vir \equiv \sum_i \vec{r}_i \cdot \vec{F}_i$ ("virial" of the cluster) and $K_T = \frac{1}{2}\sum_i M_i \left(\frac{dr_i}{dt}\right)^2$

(total kinetic energy),

$$\frac{1}{2}\frac{d^2\Theta}{dt^2} = Vir + 2K_T. \tag{4.2}$$

If the cluster is stationary, the time average of the time derivative of Θ is zero, and only what is called the virial theorem will remain

$$\overline{Vir} = -2\overline{K_T}. \tag{4.3}$$

Assuming

$$Vir = U = -\sum_{i<j} G_N \frac{M_i M_j}{r_{ij}} \rightarrow \text{Law of Universal Gravitation}, \tag{4.4}$$

where $r_{ij} \equiv |\vec{r}_j - \vec{r}_i|$, and that the mass of the cluster M_T is uniformly distributed in a sphere of radius R_T ($\rho = M_T/V_T = \frac{3M_T}{4\pi R_T^3}$), the virial will be

$$\begin{aligned} U = \int V(r)dm = -\int_0^{R_T} \frac{G_N}{r}\frac{4\pi r^3\rho}{3}4\pi r^2\rho dr = \frac{-16\pi^2 G_N \rho^2 R_T^5}{15} = \\ = \frac{-16\pi^2 G_N R_T^5}{15}\left(\frac{3M_T}{4\pi R_T^3}\right)^2 = -\frac{3G_N M_T^2}{5R_T}. \end{aligned} \tag{4.5}$$

Since $2\overline{K_T} = \sum_i \overline{M_i v_i^2} = \sum_i M_i \overline{v_i^2}$, by averaging the velocities of all galaxies in the cluster, one can finally determine

$$\sum_i M_i \overline{v_i^2} = M_T \overline{\overline{v^2}} \rightarrow M_T = \frac{5R_T \overline{\overline{v^2}}}{3G_N}. \tag{4.6}$$

Taking as an example the Coma cluster for a simple calculation, whose average speed of galaxies observed at the time was $\overline{\overline{v_s^2}} = \overline{\overline{v^2}}/3 \approx 10^{12}\ m^2/s^2$ and the total radius is $R_T \approx 10.000.000$ light years, the value of M_T will be approximately

$$M_T \approx \frac{5 \times 9,46 \times 10^{22} \times 10^{12}\frac{m^3}{s^2}}{6,67 \times 10^{-11}\frac{m^3}{kg \cdot s^2}} \approx 7 \times 10^{45}\ kg \approx 3.5 \times 10^{15}\ M_\odot, \tag{4.7}$$

where $M_\odot$ is a solar mass.

However, the divergence lies in the fact that, on average, there are about 10^{11}

stars in each galaxy, and since the Coma cluster has approximately 1000 galaxies, the ratio of the cluster's mass to its luminosity (taken as the number of stars) is in the order of 35 $M_\odot/L_\odot$, where the expectation, if there was no DM in the universe, should be 1 $M_\odot/L_\odot$. Currently, using more accurate values for all these quantities, it is possible to estimate that this ratio can reach 400 $M_\odot/L_\odot$ depending on the cluster being considered.

The second evidence (also following the approach in [22]) was discovered due to the extensive work of Vera Rubin and her collaborators in the late 70s [23], in measuring the rotation velocity of about 20 galaxies (in one of her most important works). The problem arises due to the unexpected profile of these curves, suggesting that there should be more mass outside the galaxies than the mass coming from luminous matter.

The rotation velocity of a particle in circular orbit in a galaxy with a symmetrical axis must vary with the radius (distance to the nucleus of the galaxy) as follows:

$$v_c^2(r) = \frac{G_N M(r)}{r}, \tag{4.8}$$

where $M(r)$ is the mass within a sphere of radius r. For a punctual mass M, the ratio will be

$$v_c(r) = \sqrt{\frac{G_N M}{r}}. \tag{4.9}$$

For a spherical galaxy of radius R with constant density ρ (simplest case), v_c is given by

$$v_c(r) = \begin{cases} \sqrt{\frac{4\pi G_N \rho}{3}} r & , \mathrm{r} \leq \mathrm{R}, \\ \sqrt{\frac{4\pi G_N R^3 \rho}{3r}} \propto r^{-1/2} & , \mathrm{r} > \mathrm{R}. \end{cases} \tag{4.10}$$

However, the mass distribution of a symmetrical axis spiral galaxy like the Milky Way is very different from a spherical galaxy. The above calculation would involve special functions, elliptical integrals, or even more sophisticated mathematical objects. Even so, the result should approach v_c growing almost linearly to small r, and a $r^{-1/2}$ behavior for large r.

With the advancement of radio telescopes, Rubin was able to measure and catalog the rotation velocity of symmetrical axis spiral galaxies. This was possible due to the Doppler effect of the 21 cm line of the hydrogen atom, which allowed

the measurement of velocities at distances up to 120 kpc (depending on the size of the galaxy) from the center of the galaxies, where 1 parsec is equivalent to approximately 3.26 light years. The result was unexpected: in small galaxies (0 kpc $\leq R \leq$ 35 kpc) v_c grew rapidly to small r ($r \approx 5$ kpc) and kept growing for larger r; in the larger galaxies ($R \geq 50$ kpc), v_c also grows rapidly to smaller values of r ($r \approx 5$ kpc) and then tends to remain constant; both contradict the behavior $r^{-1/2}$, as shown in figure 4.1 below.

Some results prior to Rubin's already outlined a difference in the form of v_c, and even in 1970, astronomer Ken Freeman had already proposed a solution to this divergence, in which there should be a spherical "halo of DM around the galaxies, where $M_{DM}(r) \propto r$ for large r.

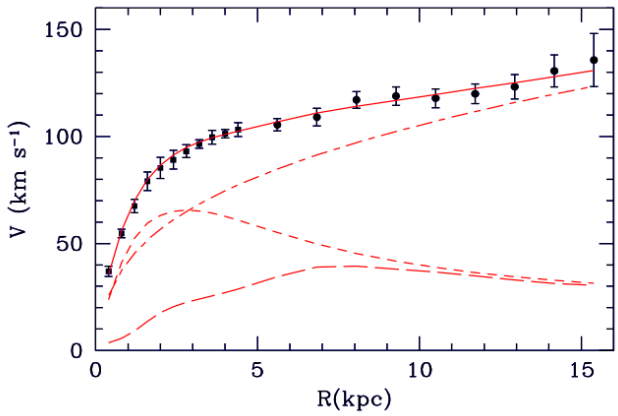

Figure 4.1: Data obtained from the rotation velocity of the galaxy M33 as a function of the distance to its center. The red curves represent the adjustment of the data points (solid line), the contribution of dark matter (dot-line), the contribution of the stars (short line) and the contribution of intra-galactic gas (long line). Retrieved from [24].

Currently, the mostly used model in simulations for the mass density profile of these halos is that of Navarro-Frenk-White (NFW) [25, 26], given by:

$$\rho(r) = \frac{\rho_0}{\frac{r}{R_s}\left(1+\frac{r}{R_s}\right)^2}, \tag{4.11}$$

where ρ_0 and R_s are parameters that change depending on the halo.

The third evidence is extremely relevant, and was able to determine some important constrains in the properties of DM. It has to do with collisions of galaxy clusters that, after the discovery and the improvements in the observations of the phenomenon of gravitational lensing, could be seen in a different aspect [27].

The phenomenon of gravitational lensing occurs due to the deflection that the light from a very distant source undergoes when passing through a very massive object, distorting the image that will be seen by an observer. There are two types of final image: those that suffer a weak effect from gravitational lenses, that is, the deflection is too small to cause a visible distortion in the image, and the light ends up having only a small amplification in its intensity; and those that suffer a strong effect from gravitational lenses, where the final image appears clearly distorted, or even, multiple images of the same object are seen.

One of the most famous examples to show the usefulness of gravitational lenses when talking about DM is the bullet cluster (figure 4.2). In addition to galaxies that emit visible light, most of the visible mass of the clusters is composed of intra-cluster gas. In collisions of galaxy clusters (such as the bullet cluster), this gas heats up and emits X-rays, which allows one to accurately estimate its location, quantity and, consequently, its mass. However, using the bullet cluster as an example, gravitational lensing measurements suggests that, first, not all of the cluster's mass is made up of the visible mass, and second, most of the cluster's mass is not where the intra-cluster gas is, but it is further away from the center of the collision.

This image suggests the existence of at least one important constrain in the properties of a DM particle. From it, it is possible to notice that the galaxies (which do not collide) follow the highest concentration of mass (given by the green contour lines), and the gas (represented by the color scale from blue to white), which collides, ends up being trapped in the center of the collision. From the region containing a higher mass concentration, determined by gravitational lensing, and using detailed hydrodynamic simulations, it is possible to determine the density of the DM contained in the cluster and a limit for the self-interaction cross section of this type of matter, estimated at $\sigma_{\chi\chi}/m_\chi \lesssim 1\ \mathrm{cm}^2/\mathrm{g}$.

The latest evidence comes from Cosmic Microwave Background (CMB) mea-

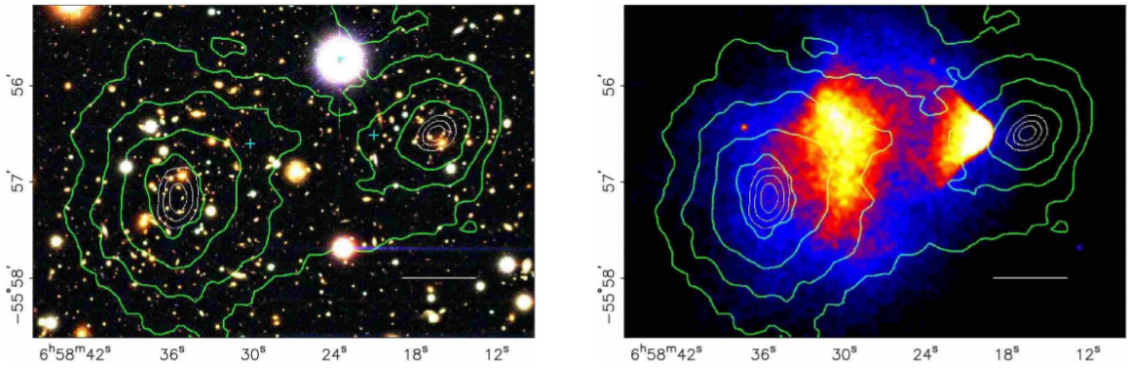

Figure 4.2: Left: comparison between the image obtained in the visible light spectrum of the bullet cluster with the contour lines (in green) obtained by gravitational lensing. Right: X-ray image comparison (blue to white color scale) and the result obtained by gravitational lensing (green contour lines). Retrieved from [27].

surements [28–30]. The Concordance Cosmological Model [31] proposes that shortly after the Big Bang there should be a quarks and gluons soup known as Quark-Gluon Plasma, charged and neutral leptons, photons and some massive bosons. As it cooled, it became possible to create new structures such as mesons, baryons, nuclei of atoms, etc.

Before 380000 years of expansion, the universe was composed of positive ions, electrons, photons and neutrinos. In this period, the environment was conducive to the interaction of photons with all these charged particles and none could escape. The period right after those years is known as the recombination epoch, when the temperature of the universe becomes lower than the energy required to ionize hydrogen, and neutral atoms began to appear that were "transparent" to the radiation existing at the time, which started to travel throughout space.

These first photons are the components of the CMB, and have valuable information about the expansion and composition of the universe. When measuring this background radiation, it was possible to perceive an important characteristic. Its temperature (∼2.725 K on average) is *almost* isotropic throughout space. There are tiny variations, of 1 part in 10000, in that temperature. In figure 4.3 is an image obtained by the Planck experiment, of the variations in the temperature of the CMB.

From these variations, it is possible to obtain the angular power spectrum,

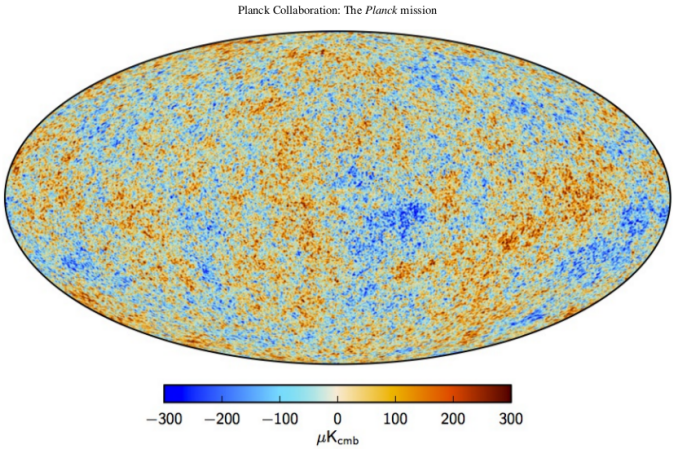

Figure 4.3: Variations in CMB temperature measured by the Planck collaboration. Notice that the scale is in μK. Retrieved from [29].

defined from the coefficients of an expansion in spherical harmonics of the temperature variation

$$\Delta T(\hat{n}) = \sum_{\ell=0}^{\ell_{max}} \sum_{m=-\ell}^{\ell} a_{\ell m}^{TT} Y_{\ell m}(\hat{n}), \tag{4.12}$$

as:

$$C_\ell^{TT} = \frac{1}{2\ell+1} \sum_{m=-\ell}^{\ell} |a_{\ell m}^{TT}|^2. \tag{4.13}$$

Figure 4.4 shows the data obtained by the Planck collaboration. The unit chosen, by convention, is

$$\mathcal{D}_\ell^{TT} = \frac{C_\ell^{TT} \ell(\ell+1)}{2\pi}. \tag{4.14}$$

The theoretical prediction, represented by the blue curve, is given by what is called the Concordance Cosmological Model. Currently, the model that best describes all available cosmological data is the ΛCDM, which says that the universe must be composed of visible matter (baryons, electrons, photons and neutrinos), "cold" dark matter (non-relativistic nowadays) and a cosmological constant Λ. It also takes general relativity as the correct way to describe gravitational interactions.

Based on this adjustment, the model determines the quantity of each of these elements using everything we know about the visible matter, and respecting other constrains concerning the DM production at the early universe. This hypothesis is also necessary for the growth of gravity wells at the beginning of the universe that

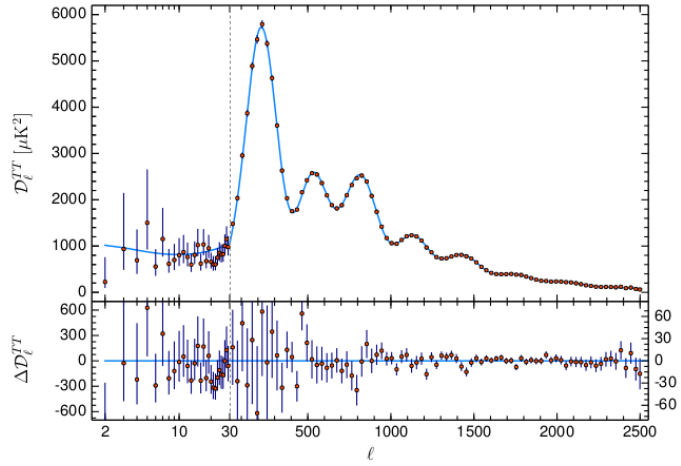

Figure 4.4: The orange dots are the data obtained by the Planck collaboration for $\mathcal{D}_\ell^{TT}$ as a function of ℓ. The blue curve is the adjustment given by the ΛCDM model. Retrieved from [30].

were deep enough to evolve to the existing structures.

To summarize, from all of these evidences it is possible to infer some of the properties of a possible DM particle:

- Stable on cosmological time scales: should exist at least before the epoch of recombination;
- Electrically neutral: doesn't interact with photons;
- "Cold" to produce the structures seen in the universe and the correct DM density observed nowadays using the ΛCDM model;
- Interacts with SM particles gravitationally, and may interact through a very faint coupling not known yet.

One could think that one of the SM particles is the responsible for the missing matter phenomena. However, the features described above are enough to discard this possibility. First of all, a DM particle can not interact electromagnetically, ruling out every quark, charged lepton, the $W^\pm$ bosons and the photon. It also can not interact through the strong force, excluding the gluons, and it has to be stable on cosmological scales, that is, the Z and H bosons are not possible candidates. Neutrinos were thought as possible DM particles, but they are relativistic nowadays, and do not fit in the ΛCDM model.

Possible Ways to Detect Dark Matter

If the missing matter phenomenon is indeed caused by a cold DM particle, there are three different ways to perceive that particle, as seen in figure 4.5:

- Direct Detection (DD): a signal can be generated by the interaction of a DM particle with a SM particle;
- Indirect Detection (ID): the annihilation or decay of DM particles into SM particles;
- DM production at colliders: if the DM particle can somehow interact with a SM particle, it can potentially be produced at particle collisions.

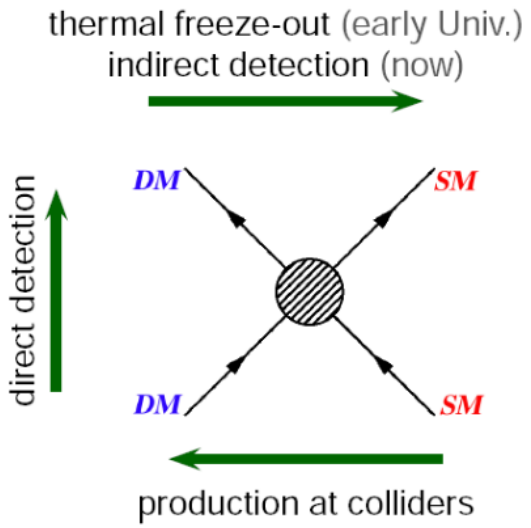

Figure 4.5: Scheme for DM detection. Left to right: DM annihilation (indirect detection); bottom to top: DM interaction with SM particles (direct detection); right to left: DM production at particle colliders.

A DD [32, 33] signal can probe the DM particle mass, since the type of signal in a given detector will be dependent of it. Also, its spin might be determined by the number of interactions with a given material in the detector, which is directly dependent of this interaction cross section, thereby, its participants spins.

This signal can be in the form of photons emitted by an excited nucleus after being hit by a DM particle, scintillation light from the nucleus recoil, atom ionization or lattice vibration in the form of phonons from MeV to GeV DM particles

masses; electron transitions in crystals band gaps or its recoil from the DM-SM scattering and phonon excitation in crystals from a few keV to a few MeV DM particles masses. Examples of experiments relying on this type of DM detection are in [34–37].

An ID [38] signal will be different depending on the DM particle considered. Some of them are: excess of gamma-ray photons, excess of neutrinos or excess of cosmic-rays. Their detection can be performed using neutrino detectors and telescopes on Earth or particle detectors as telescopes located on Earth orbit such as the ones described in [39–42].

The last one, and the focus of this work, is the DM particles production at particle colliders and their "detection" in particle detectors [43]. The challenging part of this type of DM detection is the production of the DM particles, since a sizeable cross section is needed for its production at a particle collider.

Also, since they only rarely interact with SM particles, no particle detector in a collision experiment can produce a signal of its interaction with a DM particle, but those particles production can be perceived through a detailed analysis of the collisions performed in a particle detector.

The Dark Higgs Model

With the usage of particle accelerators and particles detectors, it is possible to search for DM particles candidates. There is an enormous amount of DM models and types of particles to be looked for, as it can be seen in figure 4.6, and search recommendations are given for each of these models [43–45]. Also, several DM particle candidates searches in particle colliders have already been performed using modern particle detectors such as the ones described in [46–53]. An overview on DM particle searches can be found in [54–56].

The new physics model chosen as a reference for this work is called dark Higgs model [57, 58]. It proposes that there are three new particles in the dark sector of matter, where, one of those particles, called χ, is the DM particle that should cause all the missing matter phenomena that is observed in cosmology. It can be shown to meet all the DM particle requirements, that is, it does not interact with photons,

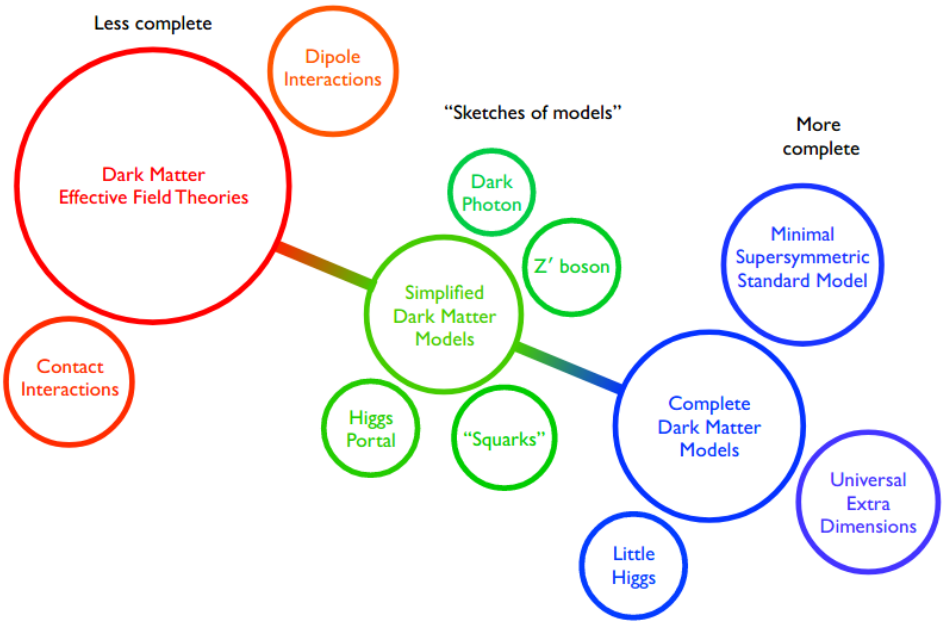

Figure 4.6: DM types of models separated by completeness. Retrieved from [45].

it is stable on cosmological time scales, its mass is on the GeV scale (it is cold), and it interacts gravitationally with SM particles.

The two other particles are a heavy vector boson called Z', just like the one in simplified DM models, such as [59], and a Higgs boson analogous that received the name dark Higgs (d_H). This d_H is responsible for a spontaneous symmetry breaking of the dark sector symmetry group, giving explicit mass terms for the Z' boson and the DM particle, instead of needing to put those terms by hand in the Lagrangian. The reason for choosing this model is that this mechanism goes beyond the simplified models, providing an explanation for the masses of the dark sector particles. Besides that, even though Z' couples to the SM quarks, the d_H particle is also assumed to decay into SM particles, providing a distinct signature for this model study in particle colliders.

Model Lagrangian

The model is composed of three new fields in the dark sector of matter: one associated to a vector boson Z', a Majorana fermion χ that should be the DM that currently exists in the universe (electrically neutral, very weak interaction with the

SM, cold, etc.), and a new complex Higgs field $\mathrm{D_H}$. The existence of a Higgs boson analogous field provides the opportunity to explain the mass generation mechanism of the vector boson and the DM fermion through a spontaneous symmetry breaking of the group that govern their interactions, giving rise to a new physical Higgs boson analogous $\mathrm{d_H}$, defined by $\mathrm{D_H} = \frac{1}{\sqrt{2}}(\mathrm{d_H} + w)$, where w is the $\mathrm{D_H}$ vev.

In this case, since there is only one gauge boson to acquire mass, the simplest gauge group is $U_{DM}(1)$, and the field $\mathrm{D_H}$ will carry a charge $q_{\mathrm{D_H}}$ under it. Assuming that Z' couples with χ, so that every dark sector particle can couple with each other, the Lagrangian will be:

$$\mathcal{L}_\chi = -\frac{1}{2} g' q_\chi Z'^\mu \bar{\chi} \gamma^5 \gamma_\mu \chi - \frac{y_\chi}{2\sqrt{2}} \mathrm{d_H} \bar{\chi} \chi + \frac{1}{2} g'^2 q_{\mathrm{d_H}}^2 Z'^\mu Z'_\mu (\mathrm{d_H^2} + 2\mathrm{d_H} w), \tag{4.15}$$

where y_χ is the coupling strength between χ and $\mathrm{d_H}$ and g' is the $U_{DM}(1)$ gauge coupling. Also, $q_\chi = \frac{q_{\mathrm{d_H}}}{2}$ as a gauge invariance requirement. From that it is possible to extract the DM particle mass as $m_\chi = \frac{y_\chi w}{\sqrt{2}}$ and the Z' boson mass as $m_{Z'} = 2 g' q_\chi w$. With the redefinition $g_\chi \equiv g' q_\chi$, the interaction Lagrangian becomes

$$\mathcal{L}_\chi = -\frac{1}{2} g_\chi Z'^\mu \bar{\chi} \gamma^5 \gamma_\mu \chi - g_\chi \frac{m_\chi}{m_{Z'}} \mathrm{d_H} \bar{\chi} \chi + 2 g_\chi Z'^\mu Z'_\mu (g_\chi \mathrm{d_H^2} + m_{Z'} \mathrm{d_H}). \tag{4.16}$$

Assuming that Z' may couple to SM quarks by

$$\mathcal{L}_\chi = -g_q Z'^\mu \bar{q} \gamma_\mu q, \tag{4.17}$$

there are then six parameters to be defined in this theory: the masses of the three particles $m_{Z'}$, m_χ, $m_{\mathrm{d_H}}$, the couplings g_χ and g_q, and a mixing angle θ, since it is assumed that $\mathrm{d_H}$ can mix with the SM Higgs boson. Choosing the couplings as $g_\chi = 1$ and $g_q = 0.25$, to be in agreement with the ones currently used for DM searches at modern particle colliders [43], it is necessary that the masses of the particles are of the order of GeV to preserve the currently observed DM relic density, making the candidate χ to be a cold DM. Besides that, a mixing angle value of $\theta = 0.01$ will be fixed throughout this work. It is a rather small value not to give rise to any other observable phenomena, and to agree with the SM Higgs observed properties, but it is high enough to force the $\mathrm{d_H}$ to decay promptly. This mixing, combined with the $q\bar{q} \to Z'$ process, provides the possibility to observe a different

signal of this process in modern particle detectors. The process $q\bar{q} \to Z' \to q\bar{q}$ is also a possibility, and there are searches for this signature as well [47, 60, 61].

The lightest particle in the dark Higgs model is chosen to be the dark Higgs, such that the DM particle can annihilate into lighter dark sector particles ($\chi\chi \to \mathrm{d_H d_H}$). Because of the $\mathrm{d_H}$ mixing to SM particles, it will promptly decay into SM states, making this process to be of great importance to set the DM relic density currently measured. Another imposition is that Z' is the heaviest particle, such that it can decay into the DM particles. If $m_{Z'} < 2m_\chi$, the process $Z' \to \chi\chi$ is highly suppressed by the need of an off-shell Z', but, either way, both regions can be studied. To summarize, we are going to consider mainly the cases where $m_{d_H} < m_\chi < m_{Z'}$[2].

The Z' boson decay, in the absence of the dark Higgs boson, might occur to SM quarks ($Z' \to q\bar{q}$) or, if $m_{Z'} \geq 2m_\chi$, to DM particles ($Z' \to \chi\chi$). But, due to the interaction of Z′ with $\mathrm{d_H}$, three body processes can happen as $Z' \to \chi\chi\mathrm{d_H}$, in the form of a dark-Higgstrahlung, that is when a Z' spontaneously emits a dark Higgs boson (analogous to a Higgstrahlung, when a Z emits a Higgs boson). This type of decay is going to be referred to as a mono-dark Higgs process.

The interest in the mono-$\mathrm{d_H}$ processes ($\chi\chi\mathrm{d_H}$), is that it has a striking signature in a particle detector, since it is assumed that $\mathrm{d_H}$ has a mixing angle with H, so that there is a production channel through $q\bar{q} \to Z'$ and a different SM decay channel that can be reproduced and detected. Given that the largest fraction of H decay is in two b quarks, the expected signal in a modern particle detector is of the form $\not{E}_T + b\bar{b}$, as can be seen in figure 4.7 below. The missing transverse energy ($\not{E}_T$) is the kinematic variable which indicates that some particle invisible to the detector was produced in the collision, and is calculated as

$$\not{E}_T = |\vec{\not{p}}_T|, \tag{4.18}$$

with

$$\vec{\not{p}}_T = -\sum_{i=1}^{N} \vec{p}_T{}^i, \tag{4.19}$$

where N is the number of particles detected by the detector and $\vec{p_T}$ is the particle momentum in the transverse plane, defined as $\vec{p_T} = \sqrt{p_x^2 + p_y^2}$. It is called

[2]For completeness, we are also going to briefly study some cases outside this constraint.

transversal since the plane $x - y$ usually is perpendicular to the beam axis in a modern particle detector. $\not{E}_T$ may have a large uncertainty, since the uncertainties in determining the $\vec{p_T}$ of each particle in the event are being summed up.

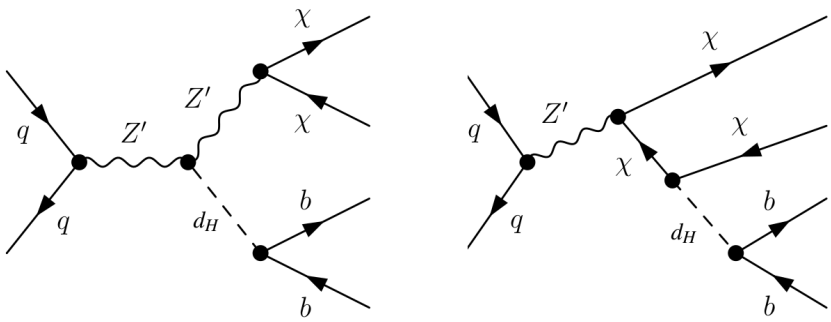

Figure 4.7: Examples of production and decay of the particles predicted by the dark Higgs model for the mono-dark Higgs process. Extracted from [57] (modified).

The mono-d_H process have a non-negligible production cross section in a particle collision, and its events can be detected by modern particle detectors. The left panel in figure 4.8 shows the mono-d_H process simulated cross section dependence with $m_{Z'}$ for $m_\chi = 100$ GeV, and three distinct values of m_{d_H} (50 GeV, 70 GeV and 90 GeV). The right panel shows the same dependence, but with $m_{d_H} = 50$ GeV and different values of m_χ (100 GeV, 200 GeV and 400 GeV). The simulation of the process with an extra jet ($pp \to Z'j \to \chi\chi d_H j$) was also performed, to match the approach of [57]. This extra jet process (where the jet comes from initial state radiation) was necessary to enhance the possibility of having a higher $\not{E}_T$ event.

In this work, the particle collisions and their detection were performed using Monte Carlo (MC) events generators. This is useful since the signal measured in the detector from events that were simulated using different choices of the model parameters can be exploited, and different data analysis techniques might be tested. In the next chapter, there is a description of how these MC simulated events were generated.

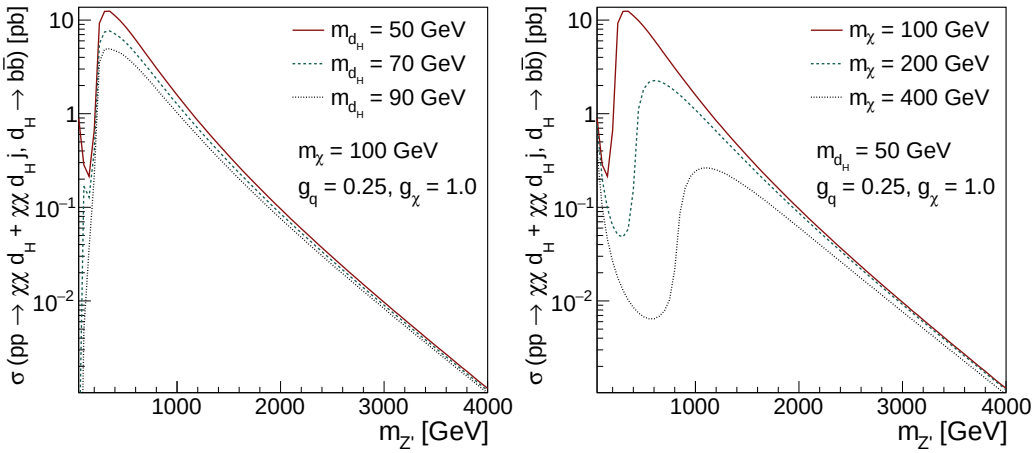

Figure 4.8: Simulated cross section dependence of the mono-d_H process (and the one with an extra jet) with $m_{Z'}$ for fixed m_χ and distinct values of m_{d_H} (left) and fixed m_{d_H} with different values of m_χ (right).

Chapter 5

Monte Carlo Events Generation

In this work, the analyzed events are not real data that comes from the CMS detector. They are generated from Monte Carlo generators that try to reproduce the real world of particle collisions and their detection. It is possible to generate only the events of interest (mono-d_H and BG) with a few generation requirements that will help on the subsequent events selection and analysis.

Nowadays, the state-of-the-art on Monte Carlo generation for HEP relies on very complete software packages. Some of them are MadGraph5_aMC@NLO [62] for the simulation of the collision process at tree level, Pythia8 [63, 64] for the simulation of hadronization and showering of particles, and GEANT4 [65] for the simulation of the detectors response to particles traversing them. The combined use of these three softwares is capable of providing generated data of particle collisions being detected by different types of detectors.

MadGraph5 is a generator of the hard process of the event to be analyzed, which calculates cross sections extremely quickly. It is possible to generate processes in leading order (LO) and next to leading order (NLO) in QCD and QED, and the software can simulate practically all known processes of the SM up to those orders with a very simple syntax.

Pythia8 is also a MC events generator, which allows the simulation of particle collisions at high energies, from the hard process (at tree level), to the hadronization of partons, including initial and final state radiation, and multipartonic interactions.

GEANT4 is a particle detector simulator that will reproduce the full interaction of the particles in a collision taking into account all the processes involving the interaction of those particles passage through matter. Its results are used by the LHC collaborations (and many other) to generate simulated events for the com-

parison with real data collected by the experiments. GEANT4 is one of the best particle detector simulator, but it takes a lot of computational resources and time (on the order of a second per event) to generate data.

An alternative to GEANT4 is the Delphes software package [66], that uses parameterized formulas for a detector's response and resolution to physics objects instead of making the simulation of the interaction of particles with matter. This approach provides moderately reliable simulated events, but it takes two to three orders of magnitude less time to simulate a collision than GEANT4. It can simulate different types of detectors, and with its modular structure it is possible to make changes in different parts of the simulation to implement and test a different response or resolution (possibly related to different reconstruction techniques) on the particles' detection.

In this work, MadGraph5_aMC@NLO (version 2.6.7), Pythia8 (version 8.244) and Delphes (version 3.4.2) were used to simulate the CMS detector response to pp collisions at a center of mass energy of 13 TeV. There was no application of any trigger selection in the generated events, that is, a trigger efficiency close to 100% is being considered. This is compatible with the findings of [67], where it is claimed that "the trigger efficiency is measured to be 97% for events passing the analysis selection for $\not{E}_T > 250$ GeV and becomes fully efficient for events with $\not{E}_T > 350$ GeV". Two other softwares packages must be used to fully reproduce the Parton Distribution Functions (PDF) of the protons colliding and to apply the jet reconstruction algorithms on the detected particles to find jets and to calculate their quantities. They are LHAPDF6 (version 6.1.6) [68] with the NNPDF (version 2.3) [69] as the PDF and FastJet (version 3.3.2) [70] with the anti-k_T [71] jet reconstruction algorithm, respectively. A last remark is that the MLM scheme [72, 73] was used for the merging of parton showers.

The generation of MC events is accompanied by some generation requirements. Depending on the application, these thresholds may remove very low $\vec{p_T}$ particles, produce HEP objects that are in a given region of space (given as η and ϕ coordinates to match the detectors coordinates system), constrain the invariant mass of pairs of particles or jets, and much more. As discussed in chapter 4, the process of interest in this work is the mono-d_H, where the dark Higgs particle decays into $b\bar{b}$ quarks.

Signal in CMS

Due to b quarks hadronization, B hadrons will be formed along with other hadrons to compose jets that are named b-jets [74, 75]. It is different from other jets because it has two very distinguishable characteristics. The first is that the life time of B hadrons is large enough for it to propagate through the inner layers of the CMS detector without leaving any signal, and then it decays. This is perceived as a secondary vertex with a large impact parameter (perpendicular distance from the vertex to the IP) by the detector. The second characteristic is that a B hadron has a probability of $\sim 20\%$ to decay to an electron or muon in a semi-leptonic decay, which turns jets containing charged leptons into very promising b-jets candidates.

In the CMS detector, a charged hadron inside a jet will leave its footprint in the tracker and deposit all of its energy in the Hadron Calorimeter (HCAL). Neutral hadrons only deposit their energy at the HCAL, since they don't interact with the tracker. Information collected using the particle signals in all subdetectors are combined into particle flow objects [76] that will be used in jet reconstruction algorithms.

Unfortunately, the two b-jets signal can be easily mimicked by the QCD multijet background. Even though it is relatively simple to separate b-jets from jets arising from light quarks and gluons (u, d, s, c, and g), the QCD background also have b-jets. An important feature of the model to suppress this type of background is the $\not{E}_T$ signature, which should not exist in QCD processes, but might happen due to events mismeasurements. However, it is highly unlikely for the QCD background processes to have a very large amount of $\not{E}_T$, something that will be useful in the events analysis. If the $\mathrm{d_H}$ recoils against a high value of $\not{E}_T$, both b-jets may merge into one large radius jet with substructure (also known as a fat jet) as can be seen in figure 5.1.

In order to detect the fat jet substructure [77] the trimming [78] technique is used, as it works as a filter. Low p_T particles often interfere in the calculation of the jets properties, such as its p_T or invariant mass, since they might come from other processes besides the process of interest. To suppress their effect in the fat jet variables calculation, trimming keeps only those subjets that pass a minimum requirement in p_T within the fat jet. This technique provides advantages in the

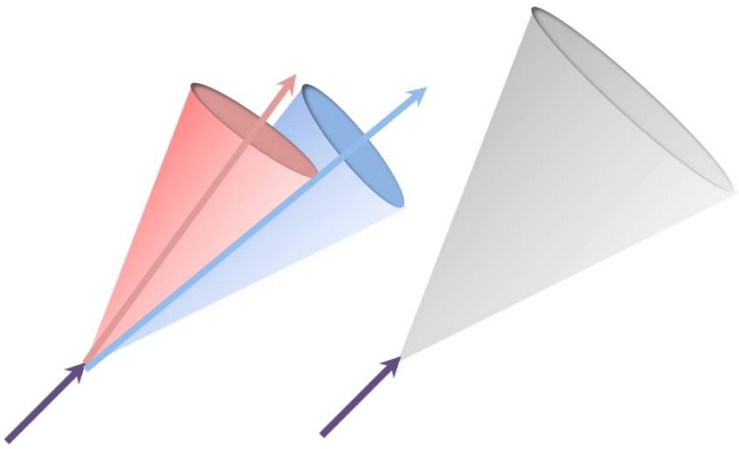

Figure 5.1: How a fat jet would look like to the detector after its two subjets merge into a large radius jet.

kinematic reconstruction of the jets and is used in events analysis to properly measure the fat jets intrinsic quantities.

It is possible to select what is the size of the reconstructed jets in an event, given by a distance parameter (or radius) $R = \sqrt{\eta^2 + \phi^2}$, that the reconstruction algorithm will use, and the minimum jet $\vec{p_T}$ for the process (this is also the case for the fat jets, with the possibility to also choose the size of the subjets to be reconstructed inside it, along with their minimum $\vec{p_T}$). A last remark about jets is that in Delphes their energy is corrected by a scaling formula defined as $p = p * \sqrt{\frac{(2.5 - 0.15 * |\eta|)^2}{p_T + 1.0}}$, where p is the jet four momentum. This is necessary since the momenta of reconstructed objects tend to be slightly different than that of the generated objects, an effect that is much more explicit in composite objects such as jets, and that is also observed in real experiments.

Delphes is used to simulate the detector response and reconstruct all the particles that the detector will see. Since jets, fat jets and $\not{E}_T$ are the most important objects for the dark Higgs search, a few restrictions are put on their reconstruction. These restrictions were applied as modifications in the Delphes

card *delphes_card_CMS.tcl* [79], that was used throughout this work to simulate the detector response. The fat jets are reconstructed using the anti-k_t algorithm, considering all the truth particles besides muons and neutrinos, with a distance parameter of $R = 1.0$. A jet reconstruction algorithm is used to build subjets using the k_t algorithm [80, 81] with $R = 0.2$, and a trimming algorithm removes those that have $p_T^j < 0.05\ p_T^J$, where j and J are references to the subjets and the fat jets, respectively. The fat jets are required to have $p_T^J > 200$ GeV and $|\eta^J| < 2.0$ after the trimming process, to ensure that those jets are inside the best efficiency region of CMS.

All the other jets are reconstructed using all charged truth final state particles using the anti-k_t algorithm with $R = 0.2$, and must have $p_T^j > 10$ GeV and $|\eta^j| < 2.5$. These p_T and η cuts are also applied to the generation of the leptons in the processes. This is an important requirement since in an analysis, high efficiency in charged particle tracks reconstruction is useful for the reduction of pile-up contribution, that is, particles that are coming from other pp collisions that happened at the same time, that do not have important information and would only interfere on a given measurement. Even though there is no pile-up simulation being performed in this work, this was used to match the procedure of a search.

A last consideration about Delphes is that it allows the tagging of jets coming from b quarks using information about the generated particles, given by MadGraph and Pythia, and the jets reconstructed by the FastJet package, which is a technique called b-tagging [82, 83]. It gives a boolean variable depending if the jet came from a b quark or from something else. As already mentioned, in the CMS experiment the b-tagging is done using displaced secondary vertices and the presence of leptons inside the jets. Since Delphes has access to the generated particles and the reconstructed jets, it associates a b to a jet if it is inside a cone of radius $R = 0.2$ centered on the jet axis. It is possible to set the efficiency to b-tag or mistakenly identify a c-jet or a light quark or gluon jet as a b-jet in Delphes. In this work, they were set as 0.7 for the b identification, 0.12 and 0.006 for the other two possibilities, respectively, to match the procedure performed in [57].

The last events generation requirement to be applied are in the $\not{E}_T$ variable that will be different for the mono-d_H and BG processes generation, as discussed further.

SM Background Generation

Something very important when searching for a new physics signal in CMS is the reduction of background (BG) processes, which, in the present case, are SM events that mimic the $\not{E}_T + b\bar{b}$ signal, or some failures in the detector system that generate false signals that may be similar to the expected signal. For the d_H model, the BG is composed of four main processes:

- $Z + b\bar{b}$: if the Z boson decays into neutrinos, the $\not{E}_T + b\bar{b}$ signal is mimicked;
- $W + b\bar{b}$: as long as the W boson decays leptonically, and the detector fails to detect the charged lepton, the $\not{E}_T + b\bar{b}$ is also reproduced;
- Diboson: this set of processes comprises $Z(\nu\bar{\nu})Z(b\bar{b})$, $W(\nu\ell)Z(b\bar{b})$ and $W^+W^- + b\bar{b}$ (from now on referred to as WW) and requires that the decays of the W bosons are leptonic and that the leptons are not identified;
- $t\bar{t} \to b\bar{b}W(q\bar{q})W(\nu\ell)$: under certain conditions, all quarks in this process can come out as if they were a single hadronic jet and, if the charged lepton is not identified, it will also reproduce the $\not{E}_T$ + fat jet signature.

In figure 5.2 are some examples of processes that can mimic the $\not{E}_T + b\bar{b}$ signal. It is important to notice here that some of those rely on leptons misidentification as $\not{E}_T$, which is a possible phenomenon to occur at a particle detector. Besides that, as seen in the d_H signal, only the processes with high $\not{E}_T$ will be relevant for. There are a few other ways to separate signal and BG events such as the $\vec{p_T}$ of the fat jet, the geometrical distance between the center of the subjets and the fat jet center, the position of the fat jet in the detector. But, first of all, the interesting events for a given study must be selected properly.

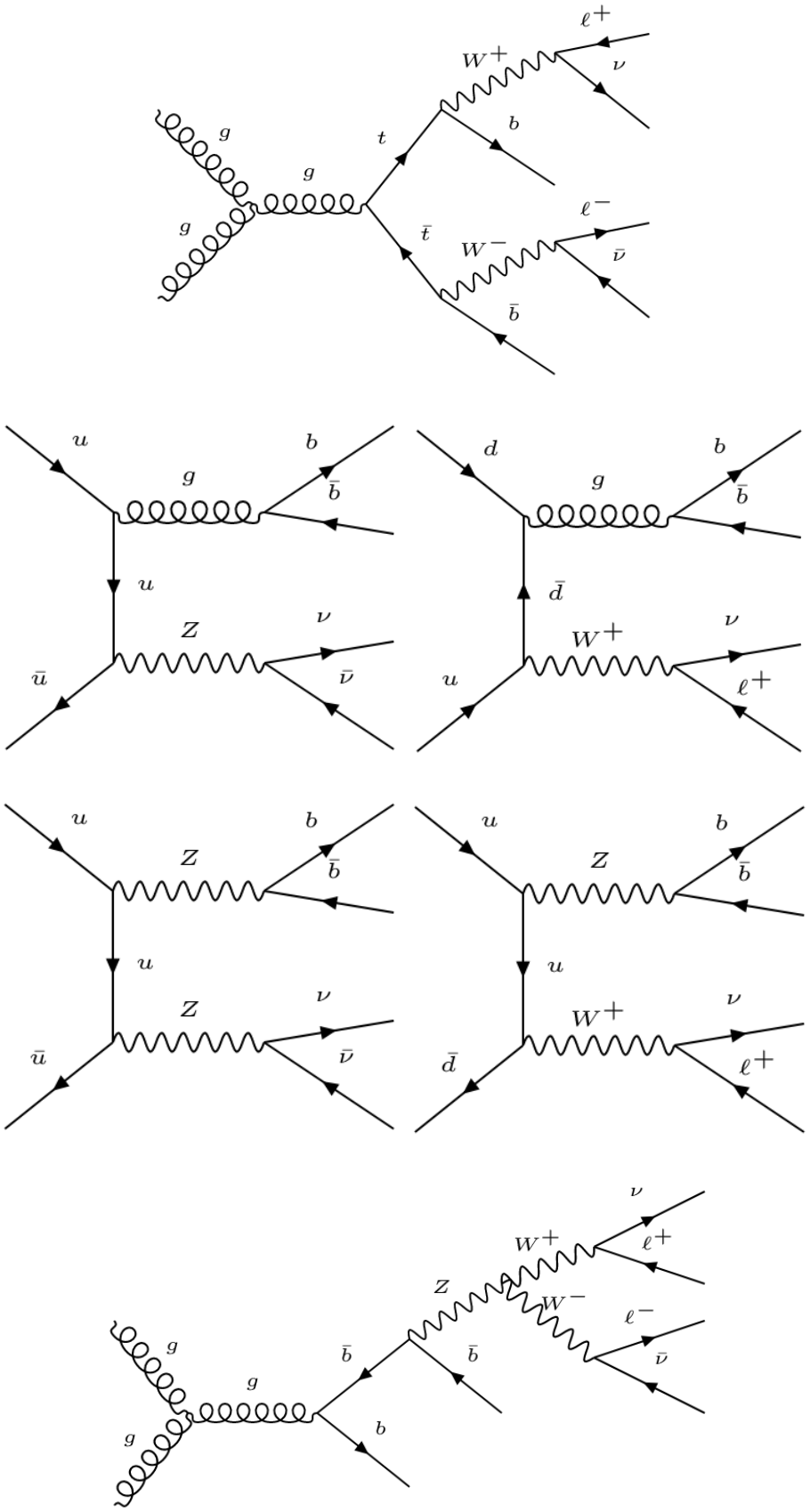

Figure 5.2: Few examples of processes that mimic the signal $\not{E}_T + b\bar{b}$ given that the leptons are misidentified. From left to right, top to bottom: $pp \to t\bar{t}$, $pp \to Zb\bar{b}$, $pp \to Wb\bar{b}$, $pp \to ZZ$, $pp \to ZW$, $pp \to b\bar{b}W^+W^-$.

Those processes were generated separately following the recommendations in [57]:

- $Z + b\bar{b}$: this process was generated at NLO, where the decay $Z \to \nu\bar{\nu}$ was performed using Madspin [84, 85], a third-party package that helps on building more complex processes in MadGraph at NLO. The cut in $\not{E}_T$ cannot be implemented at NLO, so it was required that $p_T^Z > 300$ GeV;

- $W + b\bar{b}$: generated at LO without the need of Madspin, since MadGraph allows intermediate decays in LO simulations. A requirement of $\not{E}_T > 250$ GeV was applied. The processes $W + b\bar{b}j$ and $W + b\bar{b}jj$ give large contributions to the cross section and were generated as well;

- ZZ: the $\not{E}_T$ requirement was not applied here because this process was also generated at NLO, with the subsequent decays ($Z \to b\bar{b}$ and $Z \to \nu\bar{\nu}$) being performed using Madspin. At least one of the Z bosons needs $p_T^Z > 300$ GeV;

- WZ: this process was generated at NLO, where the subsequent decays, $Z \to b\bar{b}$ and $W \to \nu\ell$ were performed using Madspin. The requirement here is that $p_T^Z > 300$ GeV or $p_T^W > 400$ GeV;

- WW: this BG process was simulated at LO using MadGraph only, with $\not{E}_T > 400$ GeV. Processes where both W bosons decayed leptonically or one decayed leptonically and the other decayed hadronically were accounted for;

- $t\bar{t}$: this last process was generated at LO as well, without the need of Madspin (MadGraph only), with $\not{E}_T > 400$ GeV. With sufficient boost, the $t\bar{t}$ decay products can merge into a fat jet with two b quarks inside. As in the two W case, the $WW \to \ell\nu\ell\nu$ and $WW \to \ell\nu q\bar{q}'$ processes were simulated.

For each BG process, 50000 events were generated using the interface MadGraph5 + Pythia8 + Delphes to simulate every step of a pp collision. The cross sections of these processes (with the generation cuts) can be seen in table 5.1. As a reminder, only the events where the prompt charged lepton was not identified properly will be relevant for the events' analysis.

Table 5.1: Cross section (σ) of each BG process given by MadGraph.

Process	σ[fb]
$W + b\bar{b}$	222
$Z + b\bar{b}$	138
$t\bar{t}$	63
WW	61
WZ	1.5
ZZ	2.6

Mono-dark Higgs Events Generation

MadGraph does not have the dark Higgs model implemented. To generate new data for the model, its Universal FeynRules Output (UFO) file is necessary. An UFO file is created through the Lagrangian of the model and contains information about every particle, decay processes, interaction vertices, etc., that MadGraph will need to perform its calculations. The UFO file used throughout this work was retrieved from [86], that was validated using the results in [57].

By generating simulated events, it is possible to select the values of the parameters of the model. As discussed in chapter 4, $\theta = 0.01$, $g_q = 0.25$ and $g_\chi = 1.0$ were fixed at first, and only the masses were changed. Several different mass points were generated, for the analysis of different phenomena. 30000 events for each mass point were simulated, with the $\not{E}_T$ threshold as $\not{E}_T > 400$ GeV to ensure the b-jets merging into fat jets. After that, m_χ and $m_{Z'}$ were fixed at 200 GeV and 1000 GeV, respectively, and 300 GeV and 1500 GeV, respectively, and g_χ and m_{d_H} were changed.

To summarize, the generation requirements on the events were the following:

- $\not{E}_T$ requirement:
  - $W + b\bar{b}$: $\not{E}_T > 250$ GeV;
  - WW: $\not{E}_T > 400$ GeV;
  - $t\bar{t}$: $\not{E}_T > 400$ GeV;
  - mono-d_H: $\not{E}_T > 400$ GeV;

- Mediator p_T:
  - $Z + b\bar{b}$: $p_T^Z > 300$ GeV;
  - ZZ: $p_T^Z > 300$ GeV;
  - WZ: $p_T^Z > 300$ GeV or $p_T^W > 400$ GeV;
- anti-k_t jets and fat jets with $R = 0.2$ and $R = 1.0$, respectively. Their p_T and η restrictions are:
  - Jet: $p_T > 10$ GeV, $|\eta| < 2.5$;
  - Fat jet: $p_T > 200$ GeV, $|\eta| < 2.0$;
- Trimming applied on the fat jets:
  - k_t subjets with $R = 0.2$ removed if $p_T^j < 0.05\ p_T^J$;
- Leptons:
  - $p_T > 10$ GeV;
  - $|\eta| < 2.5$.
- b-tagging efficiency or misidentification probability:
  - b jets: 0.7;
  - c jets: 0.12;
  - light quark or gluon jets: 0.006;

Distributions of a few variables reconstructed by Delphes are shown in figure 5.3, where the BG processes are separated, and only one of the simulated mono-d_H processes (m_{d_H} = 50 GeV, $m_{Z'}$ = 1100 GeV and m_χ = 100 GeV) was plotted. Top left image is $\not{E}_T$ histograms, top right is the fat jet p_T^J histograms, bottom left is the fat jet invariant mass m_{inv}^J, and bottom right is the difference in the ϕ angle between the $\not{E}_T$ and the fat jet given as $\Delta\phi(\not{E}_T,\ \mathrm{J})$. The histograms are normalized, fat jets are already trimmed, and a pre-selection requirement of $\not{E}_T > 400$ GeV was used to observe only the region of interest (high $\not{E}_T$).

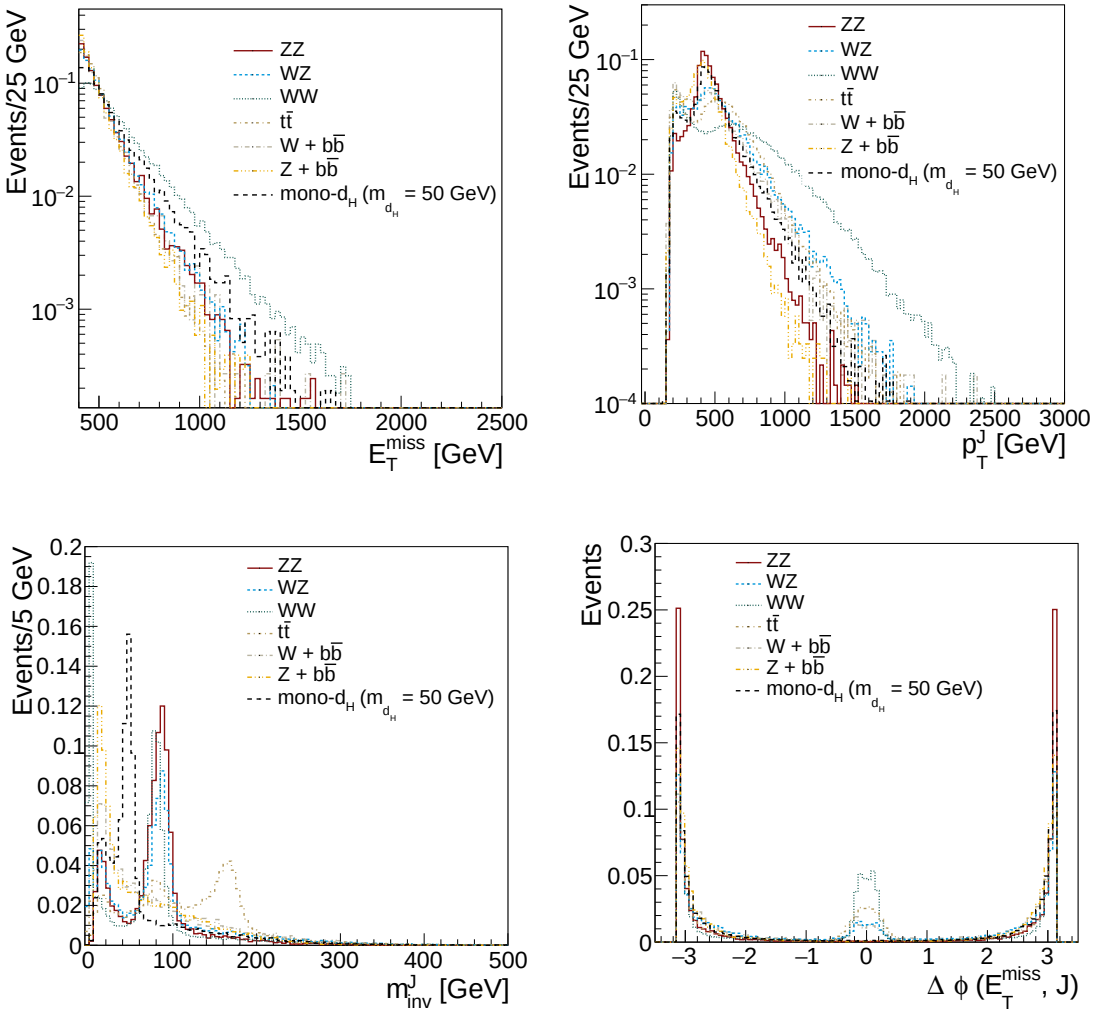

Figure 5.3: Histograms of variables of interest to the d_H model: events $\not{E}_T$ (top left), trimmed fat jet p_T (top right), trimmed fat jet invariant mass (bottom left), ϕ difference between $\not{E}_T$ and the fat jet (bottom right).

Notice that in the $\not{E}_T$, fat jet p_T and $\Delta\phi(\not{E}_T,\ \mathrm{J})$ images, the ZZ and $Z + b\bar{b}$ histograms shapes are very similar to the signal process, while the other four processes (WZ, WW, $W + b\bar{b}$ and $t\bar{t}$) show a slightly different behavior. This is due to the fact it is less probable that an event containing W bosons will produce a very well defined value of $\not{E}_T$, since its leptonic decay generates a charged lepton that may be seen as $\not{E}_T$ only if there is a mistake in its reconstruction. It also affects the fat jet p_T distribution (that is recoiling against the $\not{E}_T$), and, obviously, the $\Delta\phi(\not{E}_T,\ \mathrm{J})$ variable.

However, the fat jet invariant mass distributions are clearly very different. There are the low mass peaks of $b\bar{b}$ pairs coming from QCD processes, very evident in the WW (mainly on events with both W bosons decaying leptonically), $W + b\bar{b}$ and $Z + b\bar{b}$ BG processes, the Z and W bosons mass peaks coming from ZZ, WZ, WW (where one W decays hadronically) and $t\bar{t}$ (with a hadronically decaying W as well) events, and a highly distinct peak centered around 50 GeV, that is the chosen mass for the $\mathrm{d_H}$ particle. Since m_{d_H} is a parameter of the model and can be changed, it is expected that the m^J_{inv} peak related to the signal processes will change accordingly.

The difference on the invariant mass distributions encouraged the application of an alternative selection cut when comparing with the approach in [57]. To check its effects on the observation of the mono-$\mathrm{d_H}$ process at the CMS, the first step was to validate the simulated mono-$\mathrm{d_H}$ and BG events of the present work with the results in [57].

Model Validation

The analysis of particle collision data is performed by applying a set of selection requirements on the variables of the events. The goal of these selection requirements is to filter interesting events while removing unwanted events coming from BG. The validation of the simulated events of this work was done through the comparison of the generated events after applying the same requirements as [57].

These selection requirements, applied to the mono-$\mathrm{d_H}$ and background events, were the following:

- $\not{E}_T > 500$ GeV: to be greater than the generation requirements and to ensure that the b-jets will merge into a fat jet;
- At least one fat jet with $p^J_T > 250$ GeV and $|\eta^J| < 2.0$: after the $\not{E}_T$ cut, there must be a fat jet recoiling against it with high p_T (the η cut ensures that the fat jet is inside a high detection efficiency region in the CMS detector);
- Two or more b-tagged jets with:
    - $|\eta^j| < 2.5$: highest efficiency region of the CMS detector;

- $p_T^j > 10$ GeV: b quarks from d_H decay will have a reasonable amount of p_T;
- $\Delta R(j, J) < 1.1$: b-jets should be inside the fat jet;

- Event vetoed if there is an isolated prompt lepton (the isolation variable is defined as $I(P) = \frac{\sum_{i \neq P}^{\Delta R < R,\ p_T(i) > p_T^{min}} p_T(i)}{p_T(P)}$ where P is the particle of interest, the sum runs over every particle flow object, denoted by i, with ΔR, the geometrical distance between P and i, smaller than $R = 0.5$ and p_T higher than $p_T^{min} = 0.5$ GeV, in which the smaller its value more isolated the lepton is; it was chosen as $I^\ell < 0.1$) with $p_T^\ell > 7$ GeV and $|\eta^\ell| < 2.5$.

The first step was to check if the BG simulations make sense. Since the MC generated events are not exactly the same as what happens in reality, a global multiplication factor (known as k-factor) was used for each BG process to consider the right number of predicted events in the subsequent analysis. Note that this is an approximation, since the k-factors could depend on the kinematics of the process. To find the k-factors, the number of events in the region 80 GeV $< m_J <$ 280 GeV, that passed the selection cuts described earlier, were compared to a prediction by the ATLAS collaboration [87], as shown in table 5.2 below. This comparison was also performed in [57], and it is a reasonable choice since, even though the design of the CMS and the ATLAS detector is different, their detection efficiency is very similar.

Table 5.2: Number of predicted events in the region 80 GeV $< m_J <$ 280 GeV according to [87] and the simulations performed in this work for L = 3.2 fb^{-1}, with the selection cuts described before.

Results	Diboson	$Z + b\bar{b}$	$W + b\bar{b}$	$t\bar{t}$
BG (ATLAS [87])	1.20±0.12	3.80±0.44	2.48±0.71	4.83±0.88
BG (present work)	0.59±0.04	2.90±0.16	0.94±0.16	2.02±0.09
k-factors	2.03	1.31	2.64	2.39

Discrepancy can be noticed in every BG process. This happens due to the simple detector simulation performed by Delphes, combined with the low order simulations (specially LO). A large k-factor on $W + b\bar{b}$ is expected [88] because this process is very difficult to simulate, specially when including the $W + b\bar{b}j$

process, that has higher α_s order, and the cross section value can vary a lot with large scale uncertainties.

In figure 5.4, the comparison of the BG processes m_J stacked histograms from [57] and this work is shown. It can be seen that the number of events for each type of BG process and their respective shape in the right image is in agreement with the results of the left image.

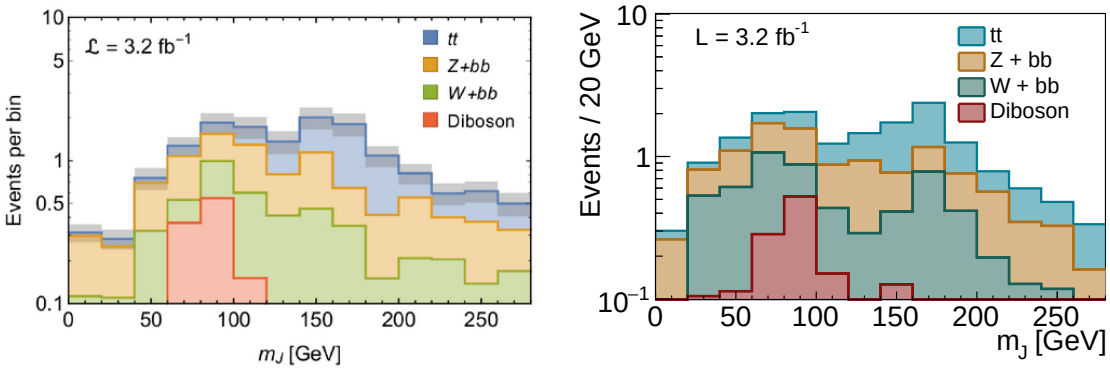

Figure 5.4: Left: m_J histogram of the various contributions to the dark Higgs model BG processes (retrieved from [57]). Right: the same histogram obtained in this work.

The validation of the mono-d_H processes was done by comparing the cross sections of simulated $m_{Z'}$ mass points (from 250 GeV to 3000 GeV) with $g_\chi = 1.0$, $g_q = 0.25$, m_{d_H} = 70 GeV and $m_\chi = 100$ GeV and the m_J histograms for three distinct m_{d_H} values (50 GeV, 70 GeV and 90 GeV) for fixed $g_\chi = 1.0$, $g_q = 0.25$, $m_\chi = 100$ GeV and $m_{Z'} = 1100$ GeV. Figure 5.5 shows the comparison of the cross section values obtained by [57] and from the simulations of this work. Selection requirements for that plot are distinct from the ones described at the beginning of this section. In the left image, [57] was comparing the cross sections of the mono-d_H search signal (orange line) with an energetic mono-jet signal ($pp \rightarrow \chi\chi + j$, blue line) using the same selection requirements applied by the ATLAS collaboration on a search for mono-jet signals [89]. These requirements, which were also applied on the mono-d_H events, were the following:

- $\not{E}_T > 500$ GeV;
- Highest p_T jet has $p_T > 250$ GeV;
- Less than four jets with $p_T > 30$ GeV and $|\eta| < 2.8$;
- Event vetoed if there is an electron (muon) with $p_T > 20$ GeV (10 GeV) and $|\eta| < 2.47$ ($|\eta| < 2.5$);
- Event rejected if $\Delta\phi(j, \not{E}_T) < 0.4$.

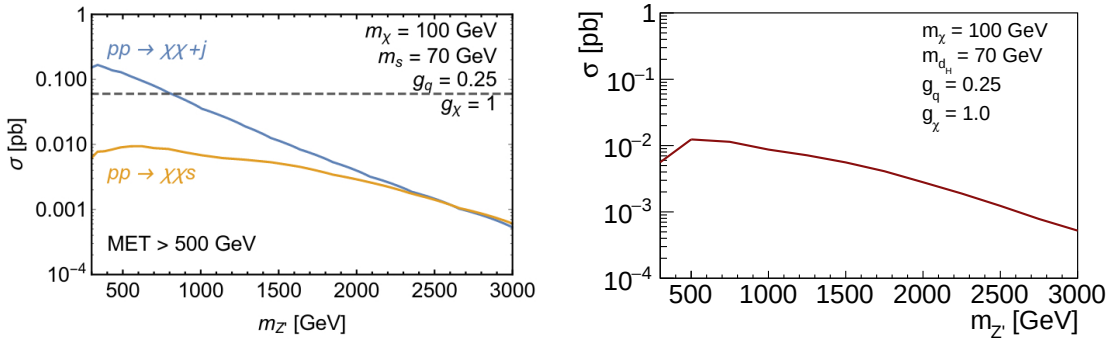

Figure 5.5: Left: comparison of the mono-jet signal cross section (blue line), with the mono-d_H signal cross section (orange line), retrieved from [57]. Right: plot of the mono-d_H signal cross section for the comparison with the results in [57]. Notice that the $pp \to \chi\chi d_H$ cross section curve of both images is in good agreement.

The dashed line represents the corresponding ATLAS detector cross section limit set by the ATLAS collaboration. Note that this selection is suitable for the mono-jet signal cross section as it is higher than that limit for small $m_{Z'}$ values. However, for large $m_{Z'}$, its cross section is very similar to the mono-d_H signal cross section values. This is due to the fact that it is harder for an event to have high $\not{E}_T$ for small $m_{Z'}$ (it would need an off-shell Z'), and an auxiliary particle improves this possibility. Since the mono-jet signal have a larger branching ratio than the mono-d_H signal, its cross section will be higher. For large $m_{Z'}$, a high $\not{E}_T$ event in the mono-d_H signal is easier to be produced, as in the mono-jet case, and its cross section decreases much slower, becoming comparable to the mono-jet one.

Right image in figure 5.5 shows the cross section for the mono-d_H signal obtained from the generated events of this work, with the mono-jet selection

described above. It is in good agreement with the orange curve from [57].

The m_J histograms comparison for the mono-d_H generated events was performed using the selection requirements of the beginning of this section. Left image of figure 5.6 shows the results obtained by [57] and the right image is the histogram obtained in the present work. The shape and the number of events for each of the m_{d_H} values are in agreement between both images. Only the events that passed the requirements described before were plotted, and this is the prediction for $L = 40\ fb^{-1}$.

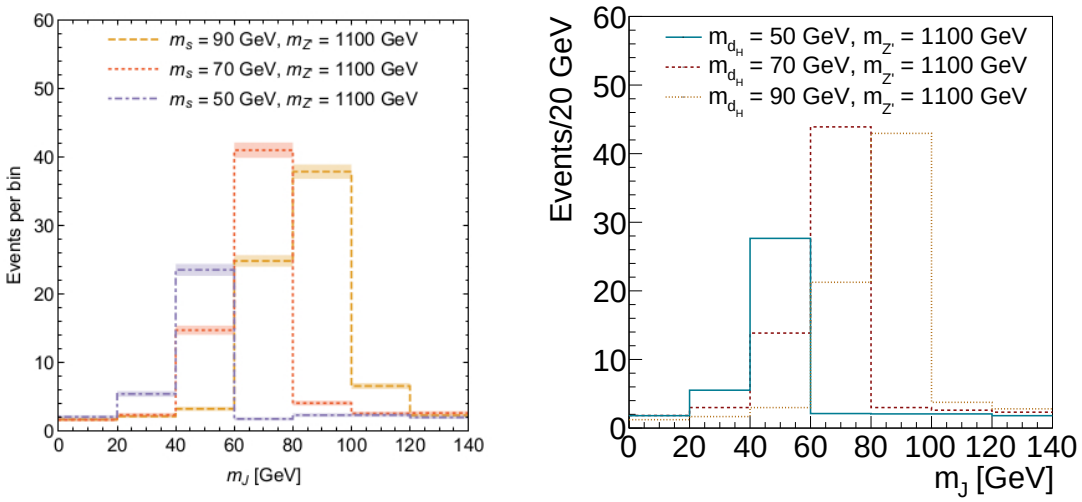

Figure 5.6: Left: m_J histogram of different m_{d_H} values (retrieved from [57]). Right: the same histogram obtained in this work. Only the events that passed the requirements described before were plotted, without considering any m_J window restriction, for $L = 40\ fb^{-1}$.

The main idea of this work was to study the feasibility of a search for the mono-d_H signal with a different requirement based on the invariant mass of the fat jet m_J. This idea arose from the fact that a resonance peak in the m_J histogram around the d_H mass should be highly distinguishable from the already existent ones, such as the Z boson. Of course that this would depend on its rest mass, but there is a very high range to be explored. The performance of an analysis using this selection requirement was compared to [57], and the results are displayed in the next chapter.

Chapter 6

Generated Events Analysis

Using the simulated events described in the last chapter, a study about the feasibility of a search for the mono-d_H signal was performed. The set of selection requirements described in the last chapter with the addition of an alternative selection on the fat jet invariant mass m_J, were used to tag the dark Higgs events while suppressing the BG events. Their purpose is to effectively separate mono-d_H from background events, which simplifies the task of defining a signal region that should contain a high number of events of interest and a small number of BG events. Since there are no previous hints on what m_J requirement to use, the first step was to find the best m_J regions that separate mono-d_H events from BG. One quantitative method to optimize a given selection requirement is to maximize the signal region significance.

For the calculation of the significance, the expression of [90] was used. It was developed for the calculation of the sensitivity of searches for new phenomena, being completely based on standard statistics concepts, suitable for optimization and it does not need any *a priori* information about the presence of a signal. These characteristics allow the determination of selection requirements that are optimal for setting limits or making discoveries. It is defined as:

$$P_S = \frac{\epsilon_S}{1 + \sqrt{N_{BG}}}, \tag{6.1}$$

where ϵ_S is the signal efficiency, that is $\frac{N_S(n \text{ cuts})}{N_S(0 \text{ cuts})}$, and N_{BG} is the number of BG events that passed the n selection requirements, also written as $N_{BG} = \mathrm{L} \cdot \sum_i \sigma_i \cdot \epsilon_i$, where L is the wanted luminosity, σ_i is a given BG process cross section, ϵ_i is $\frac{N^i_{BG}(n \text{ cuts})}{N^i_{BG}(0 \text{ cuts})}$ and i runs over every background process. From now on, this expression is going to be referred to as the Punzi significance.

Optimization of the m_J Selection Region

To find what are the best m_J regions, expression 6.1 was used to find the highest significance m_J windows in the histograms. Different d_H masses gave different windows values (center and width). At first, the m_J histograms of the events that passed the selection requirements described in chapter 5 were scanned with increasing steps of 4 GeV (0 GeV - 4 GeV, 4 GeV - 8 GeV, ...) to find the best center value m_J^C, that is, the point that gave the highest P_S value. After getting the center, a window growing with ± 2 GeV around this center value was used to get the best width m_J^W (highest P_S also).

Figure 6.1 is an example of the points searched to get m_J^C and m_J^W for $m_{d_H} =$ 90 GeV. The left image is the center scan where the plotted points are the mean of each 4 GeV region. Right image shows the total width of the window as it gets larger by summing and subtracting 2 GeV from m_J^C. Only the events that passed the other selection requirements were used to find the best m_J window. This procedure was repeated for m_{d_H} ranging from 10 GeV to 250 GeV in steps of 10 GeV with m_χ = 100 GeV and $m_{Z'}$ = 1100 GeV, and the results for m_J^C and m_J^W are summarized in table 6.1. The cross sections of these simulated processes are in table A.1 of appendix A.

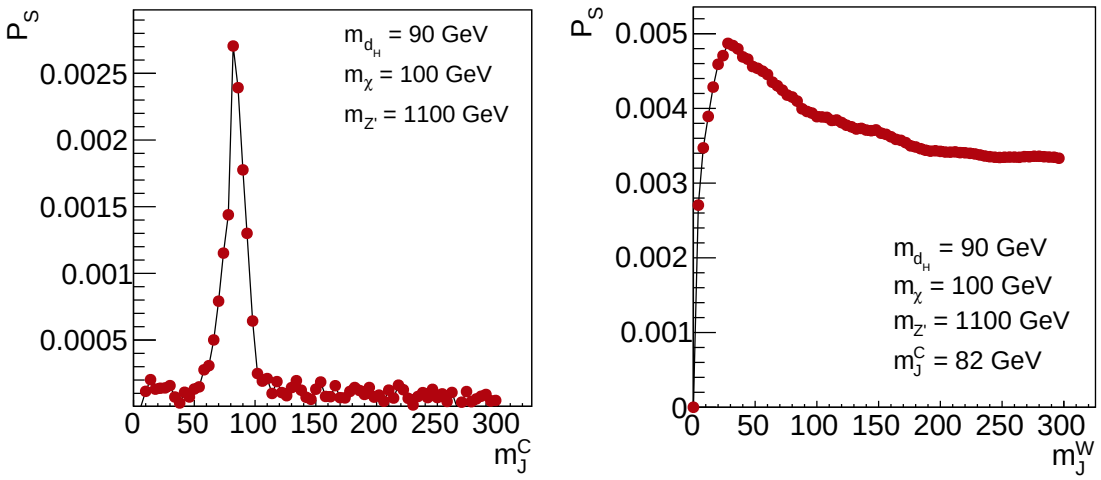

Figure 6.1: Graphs of the points used to search for the best m_J window of the $m_{d_H} = 90$ GeV, $m_\chi = 100$ GeV, $m_{Z'} = 1100$ GeV, mass point. Left: graph of the 4 GeV regions used to search for m_J^C, where the points plotted are the mean of a given region. Right: total width of the window around m_J^C. The window was growing with ± 2 GeV starting from m_J^C, and, after $m_J^W > 2m_J^C$, it starts increasing by 4 GeV to higher m_J values.

Table 6.1: Highest P_S windows for different m_{d_H}, given as $m_J^C \pm \frac{m_J^W}{2}$. Only the events that passed all the other selection cuts were considered on the calculation of P_S.

m_{d_H}	m_J^C	m_J^W
10	10	4
20	18	36
30	30	12
40	38	16
50	50	20
60	58	12
70	70	28
80	74	28
90	82	28
100	98	40
110	110	32
120	118	24
130	118	32
140	134	40
150	142	48
160	154	80
170	154	72
180	166	64
190	182	80
200	190	72
210	210	60
220	210	60
230	214	68
240	222	36
250	238	60

After finding the m_J windows, a wide range of m_χ, $m_{Z'}$ points (from 50 GeV to 1000 GeV using steps of 50 GeV and from 250 GeV to 4000 GeV using steps of 250 GeV, respectively) for different values of m_{d_H} (50 GeV, 70 GeV and 90 GeV) and g_χ, m_{d_H} points (from 0.1 to 2.0 GeV using steps of 0.1 and from 20 GeV to 240 GeV

using steps of 20 GeV, respectively; the points with m_{d_H} = 10 GeV were generated for completeness of latter results) for different values of m_χ and $m_{Z'}$ (m_χ = 200 GeV, $m_{Z'}$ = 1000 GeV and m_χ = 300 GeV, $m_{Z'}$ = 1500 GeV) were simulated (the cross section values of all the simulated points are summarized in tables A.2, A.3, A.4, A.5 and A.6 of appendix A).

The number of signal and BG events inside a given m_J window were used to perform a cut and count analysis using the *CLs* method applied with ROOT's TLimit Class [91] to find exclusion regions with 95% *CL*. This approach is distinct from the one used in [57] since their analysis method was the shape comparison of the m_J histograms containing only the events that passed the selection requirements, without considering any m_J window.

The effectiveness of the cut and count analysis method with the m_J window requirement was tested by comparing the 95% *CL* exclusion regions for different values of the model parameters obtained by this analysis and the ones obtained in [57] using the shape analysis method without a further requirement in the fat jet invariant mass.

Figures 6.2 and 6.3 show the comparison of both results of predicted events for L = 40 fb^{-1}. Left images are the exclusion regions obtained by [57] and right images are the results with the extra m_J window cut. Every mass point inside the curves is excluded with more than 95% *CL*. Notice that, even without the shape analysis, all the exclusion regions are in very good agreement, meaning that a simpler analysis method, such as cut and count, can achieve the same confidence level as a more elaborated one by using an additional selection requirement. An interpolation between the generated mass points was performed to plot the graphs on the right images. If, for a given m_χ, two subsequent $m_{Z'}$ points where one of them was excluded with more than 95% *CL* and the other was excluded with less than 95% *CL*, an interpolation, assuming that a linear function would join both points, was used to find the $m_{Z'}$ value necessary for 95% *CL*.

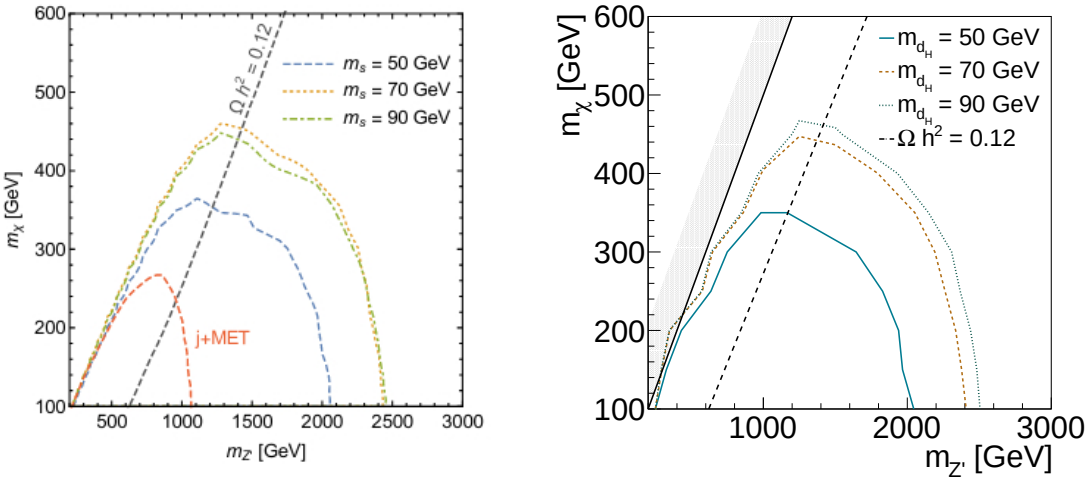

Figure 6.2: Predicted 95% CL exclusion regions for the 50 GeV (blue), 70 GeV (yellow), 90 GeV (green) m_{d_H} mass points, for L = 40 fb^{-1}. The dark diagonal line is setting the values of the model parameters that provide the right DM relic density observed nowadays using the ΛCDM model. Left: results by [57]; the red curve correspond to a standard jet + $\not{E}_T$ LHC search. Right: curves obtained in this work, using the m_J window selection cut. The hatched area corresponds to the $m_{Z'} < 2m_\chi$ region.

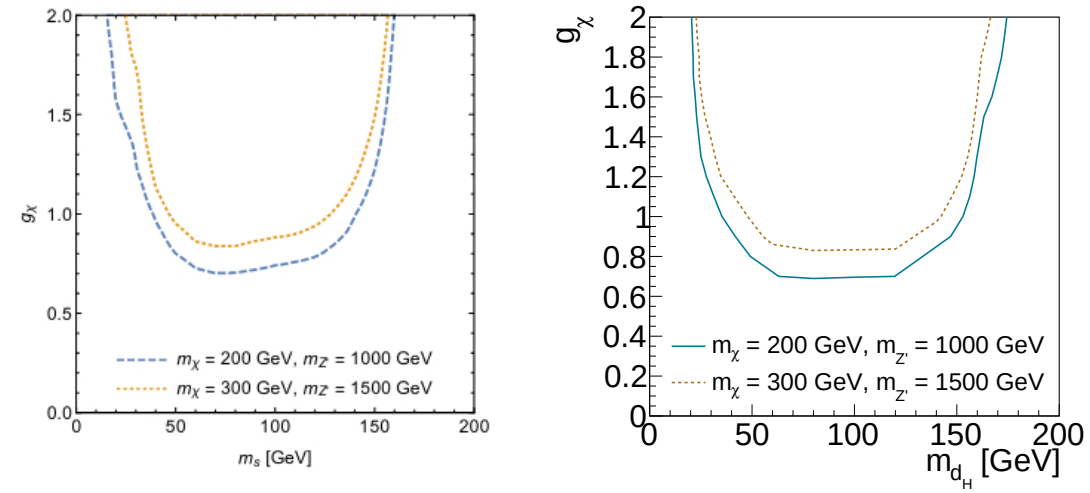

Figure 6.3: Predicted 95% CL exclusion regions for the $m_\chi = 200$ GeV, $m_{Z'} = 1000$ GeV (blue) and $m_\chi = 300$ GeV, $m_{Z'} = 1500$ GeV (yellow) mass points, for L = 40 fb^{-1}. Left: results by [57]. Right: curves obtained in this work, using the m_J window selection cut.

The hatched region in the right image of figure 6.2 represents the region where $m_{Z'} < 2m_{\chi}$, that is, the decay $Z' \to \chi\chi$ will occur only if Z' is off-shell, making the cross section of those processes very small. The dark diagonal dashed line is a reference to the values of the dark Higgs model parameters necessary to get the right DM relic density observed according to the ΛCDM model. Notice that the shape of the exclusion regions are directly related to the shape of the cross section plots, as shown in figure 6.4.

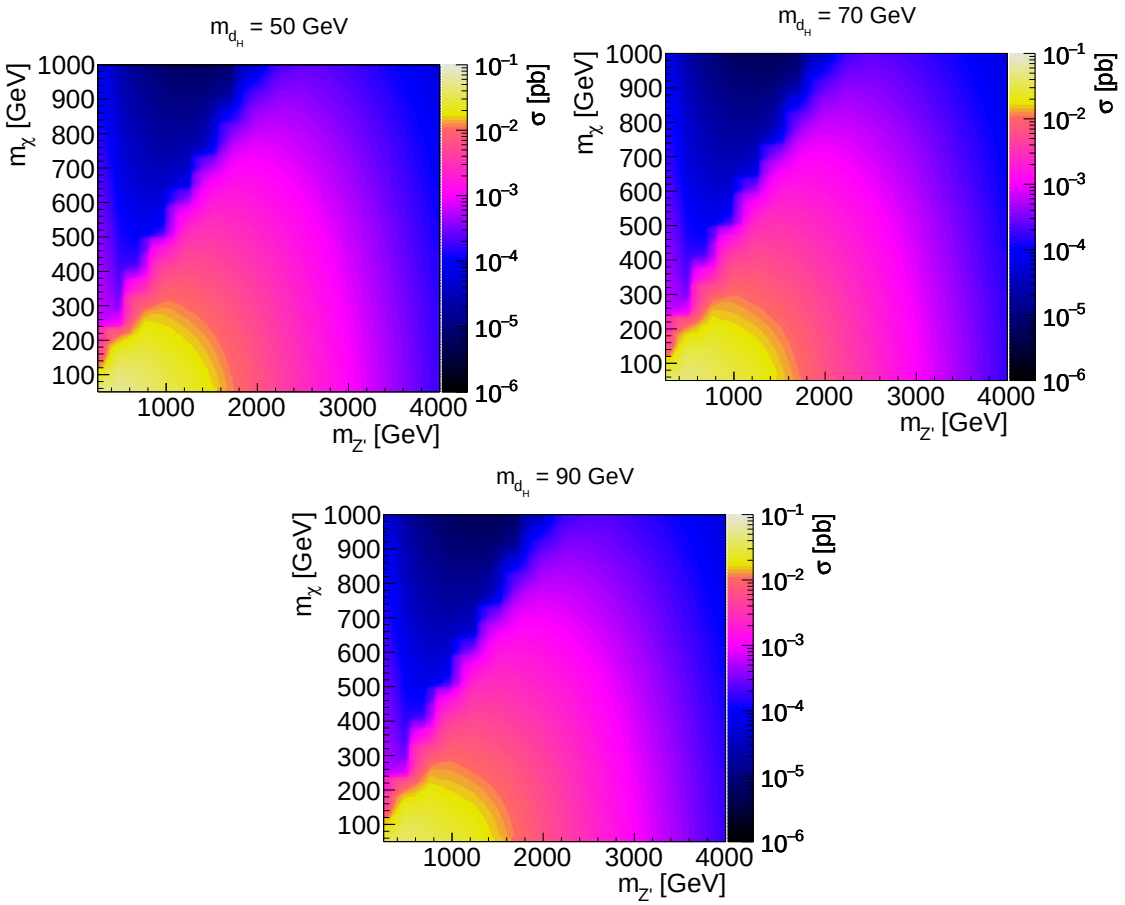

Figure 6.4: Cross section as a function of $m_{Z'}$ and m_{χ} for m_{d_H} = 50 GeV (top left), m_{d_H} = 70 GeV (top right) and m_{d_H} = 90 GeV (bottom).

In figure 6.3, there are two sudden changes in the exclusion regions for low and high m_{d_H} values. At small m_{d_H}, the boosted dark Higgs will often decay to two very collimated b quarks, that is, the jet reconstruction algorithm will not see two jets inside the fat jet, but only one jet, and these events will be excluded in the rest of the analysis, decreasing the efficiency of the mono-d_H events tagging, as it can be observed in figure 6.5. At high d_H masses ($m_{d_H} \gtrsim 150$ GeV), the decay

$d_H \to W^+W^-$ becomes available, and the cross section of the $d_H \to b\bar{b}$ process drops very quickly, decreasing the final number of events in the analysis. This decrease in cross section can be seen in figure 6.6.

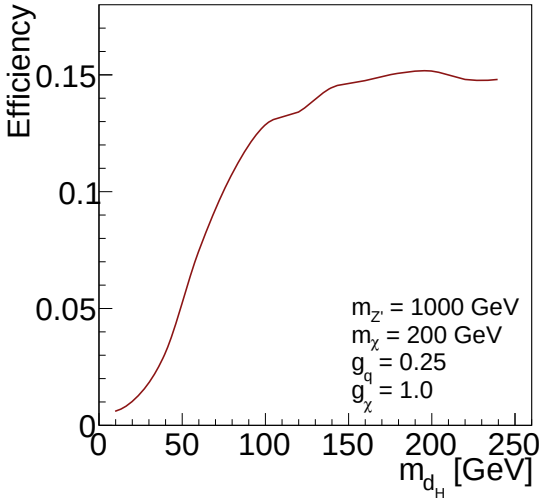

Figure 6.5: Efficiency of the selection requirements as a function of m_{d_H}. Only the m_J region requirement was not applied. The smaller m_{d_H} values have smaller efficiencies, which can be attributed to the fact that lighter d_H will recoil against the Z' with more p_T for the same $m_{Z'}$. Some of those boosted d_H decay will generate two b-jets collimated enough for the detector to observe only one jet inside the fat jet, excluding those events from the analysis. For high m_{d_H} ($\gtrsim$ 100 GeV) the efficiency is essentially constant.

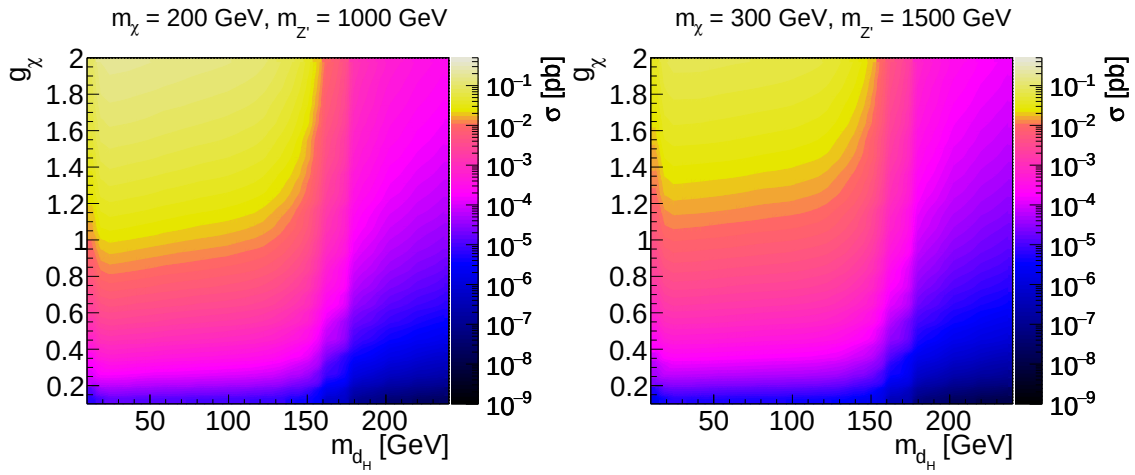

Figure 6.6: Cross section as a function of m_{d_H} and g_χ for m_χ = 200 GeV, $m_{Z'}$ = 1000 GeV (left) and m_χ = 300 GeV, $m_{Z'}$ = 1500 GeV (right). Notice the sudden decrease in the cross sections of the process $d_H \to b\bar{b}$ after $m_{d_H} \gtrsim 150$ GeV, since the decay $d_H \to W^+W^-$ becomes available.

Figure 6.7 is an example of what would happen to the exclusion region for the cut and count method with and without considering the m_J window. Notice that the m_J requirement improves the limit of the exclusion region in $10 \sim 15\%$ depending on the mass point.

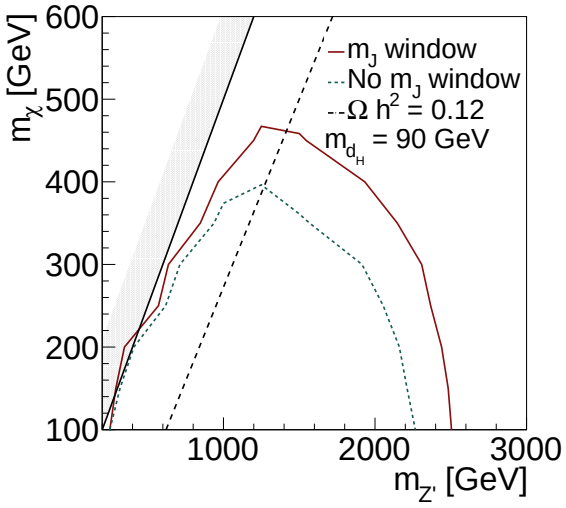

Figure 6.7: Predicted 95% *CL* exclusion regions for the mass points (m_χ, $m_{Z'}$), m_{d_H} = 90 GeV with (red solid line) and without (green dashed line) the m_J window using the cut and count analysis method on both.

Important information about the efficiency of the m_J region requirement can be obtained by the events cut flow tables. A cut flow table is generally used to display the number of events that successfully passed each requirement of a set of selection requirements that were sequentially applied. Tables 6.2, 6.3 and 6.4 are the cut flows for simulated events with g_q = 0.25, g_χ = 1.0, m_χ = 100 GeV and $m_{Z'}$ = 1100 GeV fixed, and m_{d_H} = 50 GeV, 70 GeV and 90 GeV, respectively, for L = 40 fb^{-1}. Along with the number of mono-d_H events and the number of BG events, the percentage of removed mono-d_H and background events, and the respective Punzi significance is written for each subsequent selection requirement, which are defined as $\left[1 - \frac{N_{d_H}(n \text{ cuts})}{N_{d_H}(n-1 \text{ cuts})}\right] \times 100$, $\left[1 - \frac{N_{BG}(n \text{ cuts})}{N_{BG}(n-1 \text{ cuts})}\right] \times 100$ and $P_S = \frac{\epsilon_S}{1 + \sqrt{N_{BG}(n \text{ cuts})}}$, where $\epsilon_S = \frac{N_S(n \text{ cuts})}{N_S(n-1 \text{ cuts})}$.

Table 6.2: cut flow of the simulated m_{d_H} = 50 GeV, m_χ = 100 GeV and $m_{Z'}$ = 1100 GeV.

Selection	N_{d_H}	N_{BG}	$\%N_{d_H}$ Removed	$\%N_{BG}$ Removed	Punzi Significance
Initial Events	1085.4	41931.2	0	0	4.86×10^{-3}
$\not{E}_T$	408.0	5349.1	62.4	87.2	5.07×10^{-3}
Lepton Veto	407.8	2220.9	0.04	58.5	2.08×10^{-2}
Fat Jet p_T and η	351.4	2140.0	13.8	3.6	1.82×10^{-2}
b-tagging	55.6	230.5	84.2	89.2	9.77×10^{-3}
m_J Window	27.7	17.0	50.2	92.6	9.72×10^{-2}

Table 6.3: cut flow of the simulated m_{d_H} = 70 GeV, m_χ = 100 GeV and $m_{Z'}$ = 1100 GeV.

Selection	N_{d_H}	N_{BG}	$\%N_{d_H}$ Removed	$\%N_{BG}$ Removed	Punzi Significance
Initial Events	988.1	41931.2	0	0	4.86×10^{-3}
$\not{E}_T$	362.8	5349.1	63.3	87.2	4.95×10^{-3}
Lepton Veto	362.8	2220.9	0.01	58.5	2.08×10^{-2}
Fat Jet p_T and η	334.9	2140.0	7.7	3.6	1.95×10^{-2}
b-tagging	84.3	230.5	74.8	89.2	1.56×10^{-2}
m_J Window	51.1	32.2	39.4	86.0	9.08×10^{-2}

Table 6.4: cut flow of the simulated m_{d_H} = 90 GeV, m_χ = 100 GeV and $m_{Z'}$ = 1100 GeV.

Selection	N_{d_H}	N_{BG}	$\%N_{d_H}$ Removed	$\%N_{BG}$ Removed	Punzi Significance
Initial Events	913.7	41931.2	0	0	4.86×10^{-3}
$\not{E}_T$	323.1	5349.1	64.6	87.2	4.77×10^{-3}
Lepton Veto	323.1	2220.9	0.01	58.5	2.08×10^{-2}
Fat Jet p_T and η	309.1	2140.0	4.3	3.6	2.02×10^{-2}
b-tagging	90.6	230.5	70.7	89.2	1.81×10^{-2}
m_J Window	57.4	37.8	36.6	83.6	8.87×10^{-2}

Note that, even though $\not{E}_T$ generation requirements were applied in the simulations of mono-d_H and BG events, the $\not{E}_T > 500$ GeV threshold removes more than 60% of the mono-d_H events and almost 90% of the BG events. As expected, the veto on events that had isolated leptons with $I^\ell < 0.1$, $p_T^\ell > 7$ GeV and $|\eta^\ell| < 2.5$ only affected significantly the background events since they contained leptonically decaying W bosons. Intriguing results concerning the fat jet p_T and η requirements were observed since their effect was to remove a comparable number of mono-d_H events and BG events. Even though the excluded background events number is always higher than the mono-d_H ones (approximately 80 in comparison with 56, 28 and 14 for each m_{d_H} value, respectively), the sudden decrease in ϵ_S, caused smaller P_S. This effect could be caused by the absence of other BG processes in the analysis. As stated in chapter 5, the simulated BG processes are the ones that easily mimic the signal of the mono-d_H process (fat jet + high $\not{E}_T$). But there are many other processes such as QCD multijet that have a very small possibility of mimicking the signal, but have a high cross section and can interfere in the selection of mono-d_H events. Those processes might be reduced by some of the selection requirements listed in the tables.

The consequence of the b-tagging requirement was very similar to the fat jet one, as there is a drop in the P_S value for every m_{d_H} value. This effect can be clearly perceived in the $m_{d_H} = 50$ GeV case, since (as discussed in the results of figure 6.5) the tagging of mono-d_H events gets worse for smaller m_{d_H} which decrease its efficiency. Besides that, the truly important result is the effect of the m_J requirement that, in the worst case shown, increased the Punzi significance by a factor of ~ 5. Note that the m_J window requirement removes less BG events for the $m_{d_H} = 70$ GeV and 90 GeV cases, since the best P_S m_J region, as displayed in table 6.1, starts to access the W and Z bosons mass peaks. For m_{d_H} peaked away from those regions (and the t quark mass peak), the Punzi significance should be higher.

Those results were simulating an early stage of LHC Run 2, where the expected integrated luminosity was around 40 fb^{-1}. However, since Run 2 is already over, and the CMS collaboration collected almost 150 fb^{-1} of data, it is natural to extend the excluded mass points prediction to higher luminosity, and to test for other planned LHC runs.

Projections for LHC Run 2 Data and Future LHC Runs

The prediction for the already finished Run 2 and future LHC runs were made using as reference benchmark values to the luminosity such as 150 fb^{-1}, 300 fb^{-1}, 1000 fb^{-1} and 3000 fb^{-1} that were or will be delivered by the experiment in the future [92]. This analysis is of great importance to check the feasibility of this search in the CMS experiment. No upgrades of the LHC machine or the CMS detector are being explicitly considered in these projections. But it is assumed that the performance of the detectors in the HL-LHC era will be similar to that in the present.

Figure 6.8 shows the predicted excluded regions in the plane m_χ vs $m_{Z'}$ for m_{d_H} = 50 GeV (top left), 70 GeV (top right) and 90 GeV (bottom), with luminosities equal to 40 fb^{-1}, for reference, 150 fb^{-1}, 300 fb^{-1}, 1000 fb^{-1} and 3000 fb^{-1}. Notice that for the final Run 2 luminosity, there is already a large increase in the 95% CL excluded region.

An interesting result is the large region with $m_{Z'} < 2m_\chi$ that is being accessed by the L = 3000 fb^{-1} data. This happens because, even though an off mass-shell Z' is much less probable, an enormous amount of data (years of the LHC machine running) can observe it. This also creates the possibility to study much rarer beyond standard model processes that might be probed with a particle collider.

Figure 6.9 shows the prediction for the same luminosity values, but for the parameters (g_χ, m_{d_H}), m_χ = 200 GeV, $m_{Z'}$ = 1000 GeV (left plot) and m_χ = 300 GeV, $m_{Z'}$ = 1500 GeV (right plot). The region enclosed by the lines is excluded with more than 95% CL.

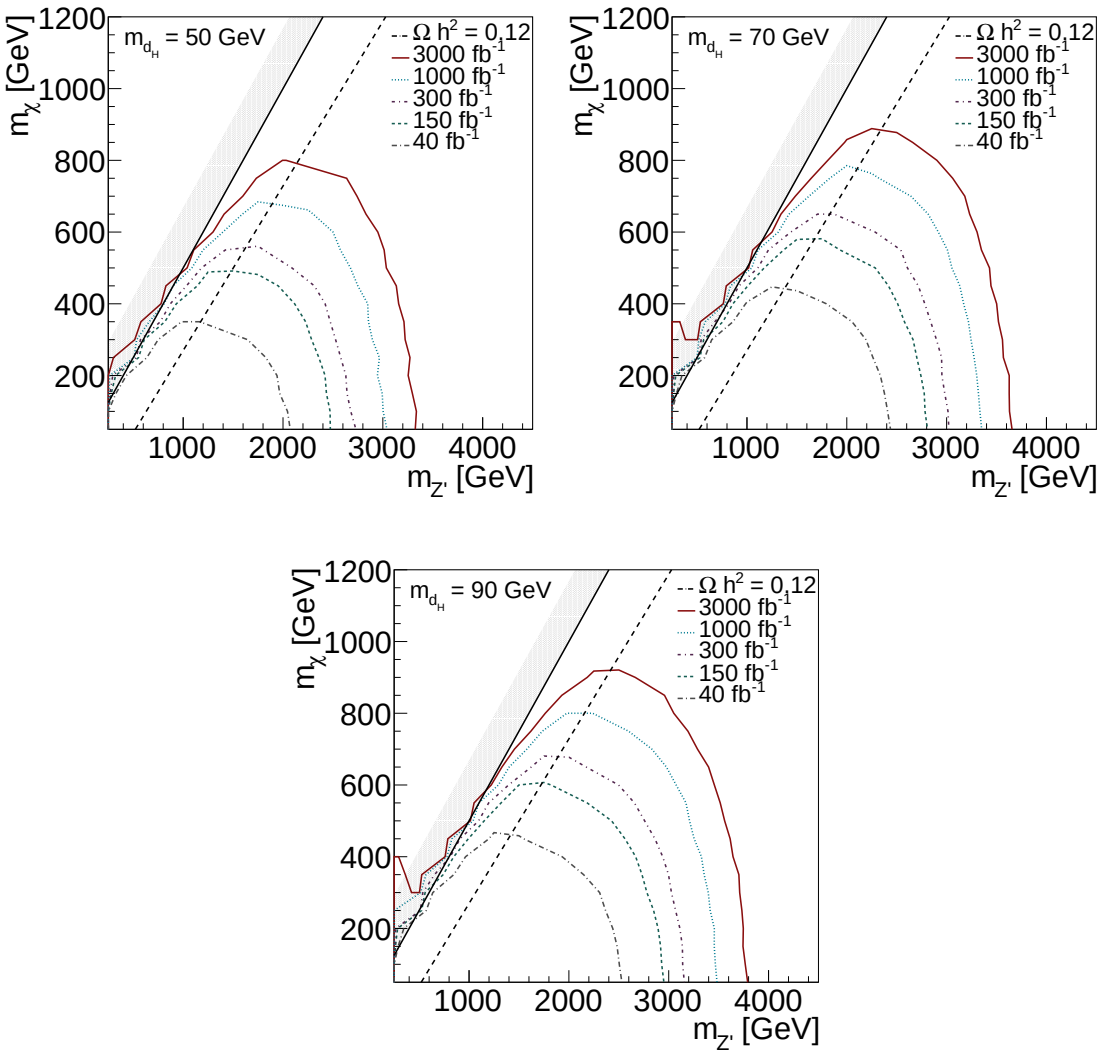

Figure 6.8: Predicted 95% CL exclusion regions of the (m_χ, $m_{Z'}$), m_{d_H} = 50 GeV (top left), 70 GeV (top right) and 90 GeV (bottom) mass points for different luminosity values. Notice that the improbable $m_{Z'} < 2m_\chi$ regions can be accessed at L = 3000 fb^{-1}.

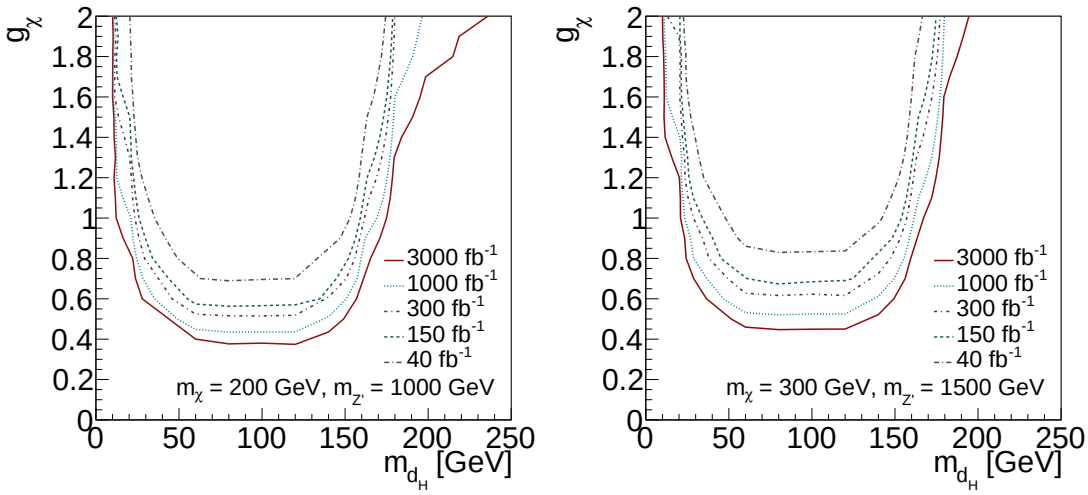

Figure 6.9: Predicted 95% CL exclusion regions of the (g_χ, m_{d_H}), m_χ = 200 GeV, $m_{Z'}$ = 1000 GeV (left), and m_χ = 300 GeV, $m_{Z'}$ = 1500 GeV mass points for different luminosity values.

Figures 6.10 and 6.11 show the cross section plots of selected sets of parameters of the model and the expected cross section to exclude the given set of parameters with 95% CL. The green and yellow areas represent the $\pm 1\sigma$ and $\pm 2\sigma$ regions, respectively. Figure 6.10 shows the cross section varying with $m_{Z'}$ ranging from 250 GeV to 4000 GeV for m_χ = 100 GeV and m_{d_H} = 50 GeV (top), 70 GeV (middle) and 90 GeV (bottom). Figure 6.11 shows the cross section varying with m_{d_H} ranging from 10 GeV to 240 GeV for g_χ = 1.0, m_χ = 200 GeV and $m_{Z'}$ = 1000 GeV (top), m_χ = 300 GeV and $m_{Z'}$ = 1500 GeV (bottom). The 95% CL exclusion limits plotted on the left images were calculated with L = 150 fb^{-1} and the same calculation on the right images was performed with L = 3000 fb^{-1}. Since the cross section of the model is luminosity independent, the red line on both columns is the same. The effect of a higher luminosity value is an increased exclusion limit CL for a given set of model parameters. That can be perceived as a shift downwards of the expected 95% CL exclusion limit bands.

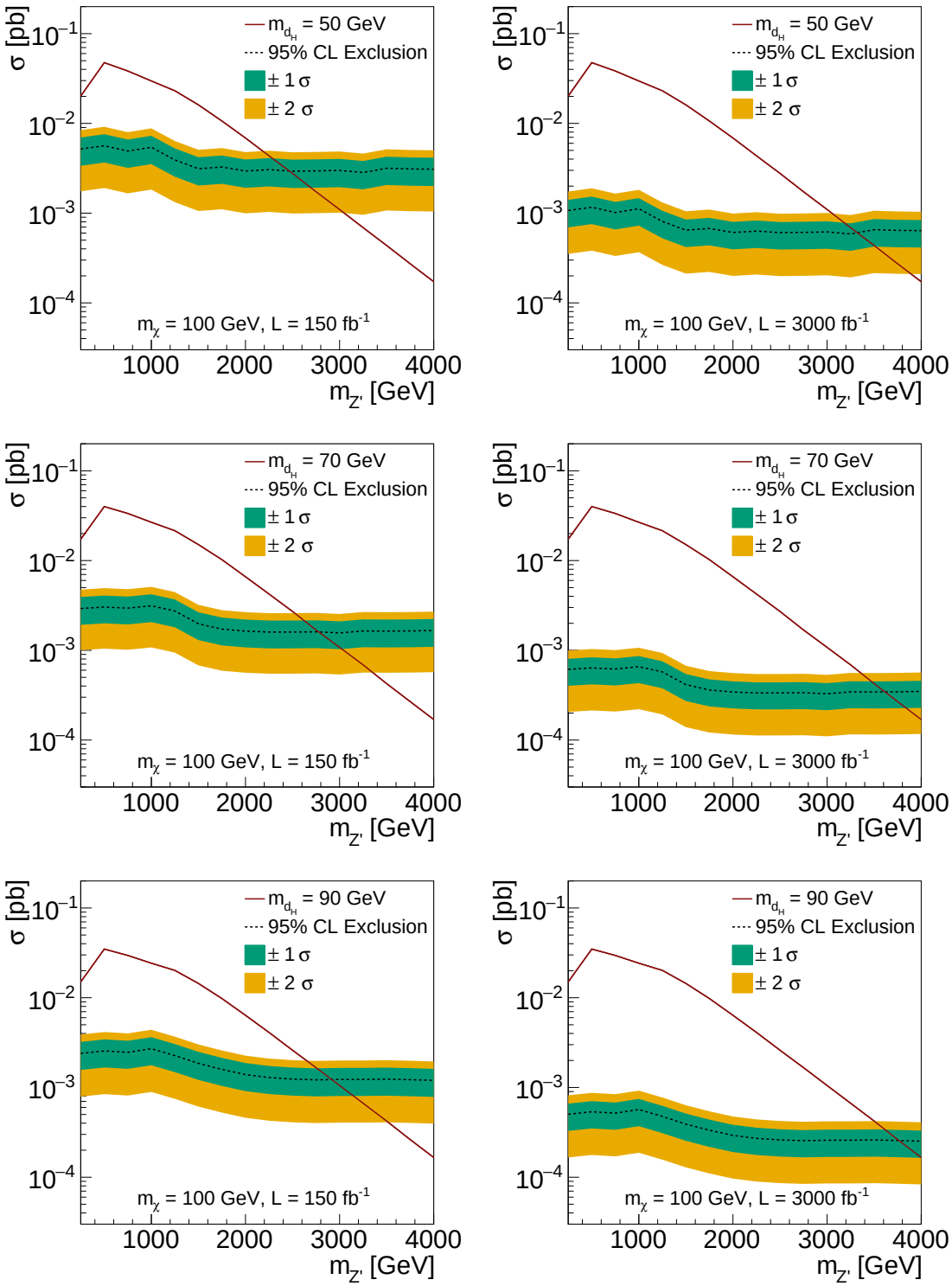

Figure 6.10: Cross section versus $m_{Z'}$ plots for m_{d_H} = 50 GeV (top), 70 GeV (middle) and 90 GeV (bottom), with L = 150 fb^{-1} (left) and L = 3000 fb^{-1} (right). The red solid line is the cross section of the simulated processes, the black dashed line represents the expected cross section for 95% *CL* exclusion and the green and yellow areas are the $\pm 1\sigma$ and $\pm 2\sigma$, respectively.

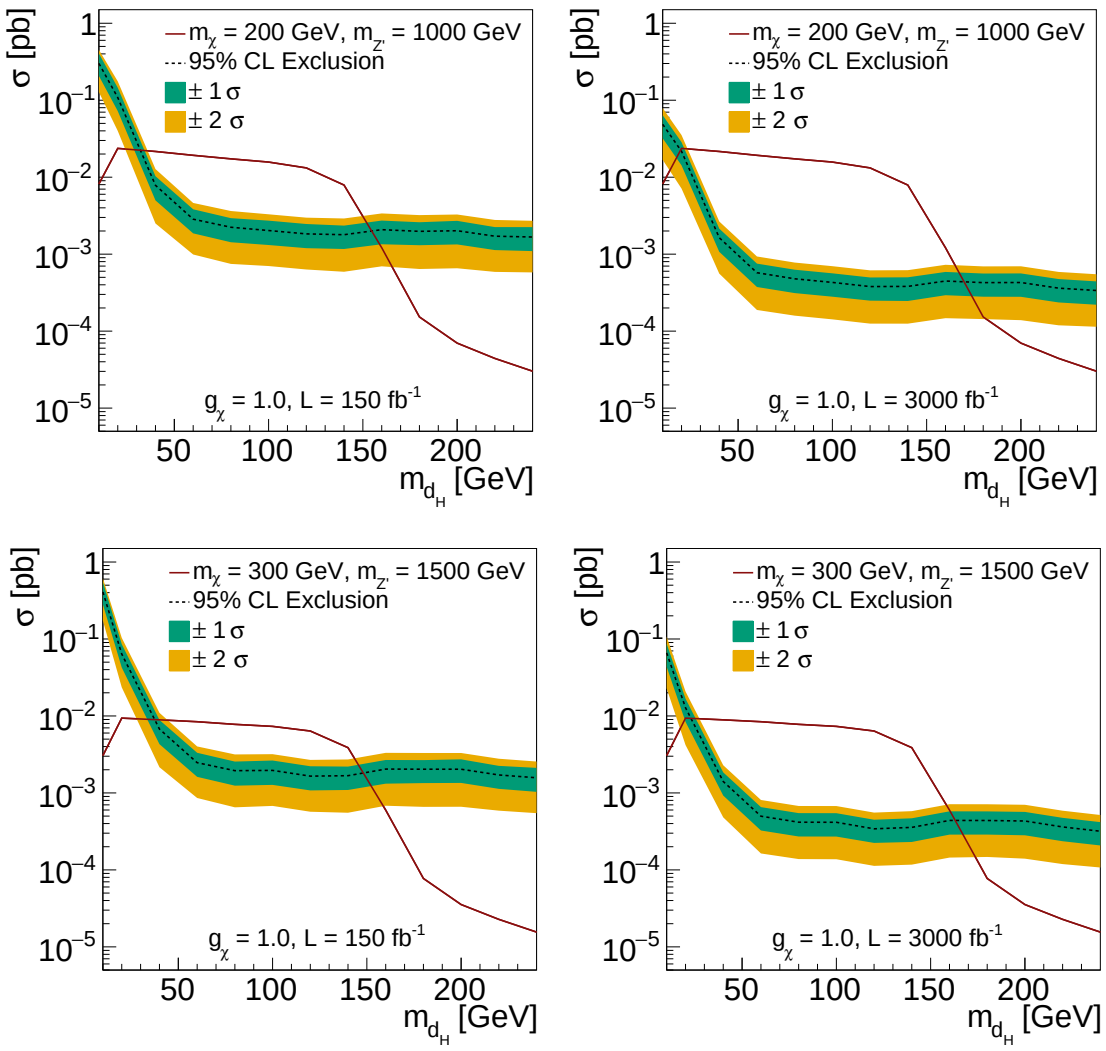

Figure 6.11: Cross section versus m_{d_H} plots for m_χ = 200 GeV, $m_{Z'}$ = 1000 GeV (top) and m_χ = 300 GeV, $m_{Z'}$ = 1500 GeV (bottom), and g_χ = 1.0, with L = 150 fb^{-1} (left) and L = 3000 fb^{-1} (right). The red solid line is the cross section of the simulated processes, the black dashed line represents the expected cross section for 95% CL exclusion and the green and yellow areas are the $\pm 1\sigma$ and $\pm 2\sigma$, respectively.

Notice that the mass point where the red solid line and the dashed black line cross each other is in agreement with the previous 95% CL regions of images 6.8 and 6.9 for the same set of model parameters and luminosity.

Chapter 7

Discussion and Conclusions

Even though the SM can describe the dynamics of every elementary particle known to date along with three of its four fundamental interactions, some phenomena are out of this scheme. One that has been bothering physicists and cosmologists for almost 90 years is the missing matter in the universe also known as dark matter. There are evidences that point to the direction of a new electrically neutral particle, stable at cosmological time scales, and that interacts very little with the standard model particles. If such a particle indeed exists, there is a chance that it can be produced in particle accelerators, such as the LHC, and detected at a particle detector, such as the CMS detector.

One DM particle model that tries to describe this new physics is the dark Higgs model, which assumes that in the dark sector of matter there should be three new particles, one of them being very similar to the SM Higgs boson, which gave the name to the model. The interactions between its particles and SM states provide the possibility of observing them at the LHC, where the CMS detector would detect a signal of $\not{E}_T$ being produced along with a large jet with substructure. In this work, no data from the experiment was used, but, using MC simulations it was possible to observe the model's characteristics and make predictions about the discovery of its particles.

The results of the last chapter were obtained with an extensive analysis of the simulated data. An interesting point that should be highlighted is the usage of a more restrictive requirement on the events selection that, not only provided the same efficiency as less selection requirements with a more elaborated analysis method such as the histograms shape comparison used in [57], but made the analysis much simpler to perform.

Besides that, the simulated processes behavior with the variation of the model parameters could be explicitly seen in the results. An important fact is the large

exclusion region covered by the analysis of data concerning L = 150 fb^{-1}, that is the data available right now for analysis from the CMS collaboration, collected in the last few years. With this data, $m_{Z'}$ values up to 2470 GeV, 2800 GeV and 2950 GeV can be probed for m_{d_H} = 50 GeV, 70 GeV and 90 GeV, respectively. m_χ values extending to 490 GeV, 580 GeV and 600 GeV, for the same m_{d_H} values, may also be probed. For m_χ, $m_{Z'}$ masses fixed at 200 GeV, 1000 GeV and 300 GeV, 1500 GeV, m_{d_H} values ranging from 13 GeV to 178 GeV, and from 20 GeV to 174 GeV, respectively, may also be explored.

This particular result obtained using a different analysis method shows that a search for this model applying the selection requirements and methods described throughout this work using CMS data is indeed feasible, and it might be performed in the near future.

Appendix A

Cross Section Tables

The cross section of every mono-d_H process simulated in this work is written in one of the six tables below. Each table contains a specific set of model parameters choice as described in its respective caption. These cross sections correspond to the simulation of 30000 events for each of the processes generated with all the generation requirements described in chapter 5 using the interface MadGraph5 + Pythia8 + Delphes.

Table A.1: Cross section values of the simulated m_χ = 100 GeV, $m_{Z'}$ = 1100 GeV mass points, for m_{d_H} varying.

m_{d_H} (GeV)	σ (pb)
10	1.01e-2
20	3.03e-2
30	2.94e-2
40	2.84e-2
50	2.71e-2
60	2.60e-2
70	2.47e-2
80	2.38e-2
90	2.28e-2
100	2.18e-2
110	2.07e-2
120	1.88e-2
130	1.58e-2
140	1.13e-2
150	6.27e-3
160	1.74e-3
170	3.38e-4
180	2.21e-4
190	1.34e-4
200	9.98e-5
210	3.47e-6
220	1.35e-6
230	7.81e-7
240	5.30e-7
250	4.01e-7

Table A.2: Cross section values of the simulated m_{d_H} = 50 GeV mass point, for m_χ and $m_{Z'}$ (both in GeV) varying.

m_χ \ $m_{Z'}$	250	500	750	1000	1250	1500	1750	2000	2250	2500	2750	3000	3250	3500	3750	4000
50	5.73e-2	5.92e-2	4.37e-2	3.43e-2	2.56e-2	1.73e-2	1.13e-2	7.20e-3	4.54e-3	2.85e-3	1.79e-3	1.12e-3	6.96e-4	4.41e-4	2.74e-4	1.73e-4
100	2.02e-2	4.75e-2	3.83e-2	2.97e-2	2.31e-2	1.61e-2	1.06e-2	6.87e-3	4.35e-3	2.77e-3	1.73e-3	1.10e-3	6.89e-4	4.36e-4	2.73e-4	1.72e-4
150	1.08e-3	3.21e-2	3.22e-2	2.48e-2	1.97e-2	1.42e-2	9.68e-3	6.41e-3	4.12e-3	2.62e-3	1.68e-3	1.07e-3	6.69e-4	4.22e-4	2.65e-4	1.67e-4
200	8.78e-4	1.49e-2	2.48e-2	2.00e-2	1.64e-2	1.25e-2	8.73e-3	5.89e-3	3.84e-3	2.49e-3	1.58e-3	1.02e-3	6.47e-4	4.12e-4	2.59e-4	1.64e-4
250	7.68e-4	1.06e-3	1.73e-2	1.64e-2	1.33e-2	1.05e-2	7.56e-3	5.26e-3	3.51e-3	2.32e-3	1.52e-3	9.65e-4	6.16e-4	3.93e-4	2.49e-4	1.58e-4
300	6.70e-4	3.60e-4	9.57e-3	1.28e-2	1.06e-2	8.67e-3	6.54e-3	4.67e-3	3.20e-3	2.10e-3	1.40e-3	9.02e-4	5.82e-4	3.78e-4	2.39e-4	1.52e-4
350	5.88e-4	2.45e-4	2.54e-3	9.22e-3	8.61e-3	7.05e-3	5.55e-3	4.08e-3	2.86e-3	1.94e-3	1.29e-3	8.41e-4	5.51e-4	3.57e-4	2.27e-4	1.46e-4
400	5.17e-4	1.88e-4	2.56e-4	5.72e-3	6.69e-3	5.73e-3	4.62e-3	3.52e-3	2.54e-3	1.75e-3	1.19e-3	7.88e-4	5.17e-4	3.37e-4	2.16e-4	1.39e-4
450	4.52e-4	1.51e-4	1.37e-4	2.43e-3	5.01e-3	4.64e-3	3.84e-3	2.99e-3	2.22e-3	1.57e-3	1.08e-3	7.31e-4	4.82e-4	3.15e-4	2.03e-4	1.32e-4
500	3.91e-4	1.25e-4	9.33e-5	2.91e-4	3.33e-3	3.70e-3	3.14e-3	2.51e-3	1.93e-3	1.39e-3	9.69e-4	6.59e-4	4.47e-4	2.95e-4	1.92e-4	1.26e-4
550	3.36e-4	1.04e-4	6.96e-5	9.66e-5	1.75e-3	2.81e-3	2.57e-3	2.09e-3	1.64e-3	1.23e-3	8.66e-4	6.06e-4	4.13e-4	2.75e-4	1.81e-4	1.18e-4
600	2.94e-4	8.72e-5	5.39e-5	5.76e-5	4.89e-4	1.97e-3	2.06e-3	1.75e-3	1.40e-3	1.07e-3	7.65e-4	5.46e-4	3.76e-4	2.52e-4	1.68e-4	1.11e-4
650	2.51e-4	7.28e-5	4.27e-5	4.00e-5	7.85e-5	1.19e-3	1.59e-3	1.44e-3	1.17e-3	9.20e-4	6.78e-4	4.86e-4	3.40e-4	2.33e-4	1.55e-4	1.03e-4
700	2.18e-4	6.20e-5	3.45e-5	2.95e-5	4.01e-5	5.00e-4	1.17e-3	1.17e-3	9.96e-4	7.91e-4	5.98e-4	4.35e-4	3.07e-4	2.15e-4	1.44e-4	9.55e-5
750	1.88e-4	5.21e-5	2.84e-5	2.25e-5	2.54e-5	8.37e-5	7.66e-4	9.34e-4	8.30e-4	6.77e-4	5.19e-4	3.86e-4	2.75e-4	1.96e-4	1.33e-4	8.94e-5
800	1.58e-4	4.40e-5	2.34e-5	1.75e-5	1.80e-5	2.98e-5	3.99e-4	6.96e-4	6.81e-4	5.76e-4	4.55e-4	3.42e-4	2.49e-4	1.76e-4	1.21e-4	8.27e-5
850	1.37e-4	3.69e-5	1.93e-5	1.39e-5	1.33e-5	1.75e-5	1.17e-4	4.86e-4	5.41e-4	4.88e-4	3.88e-4	3.03e-4	2.22e-4	1.58e-4	1.11e-4	7.59e-5
900	1.17e-4	3.12e-5	1.61e-5	1.12e-5	1.01e-5	1.16e-5	2.48e-5	2.88e-4	4.27e-4	3.97e-4	3.34e-4	2.65e-4	1.97e-4	1.43e-4	1.01e-4	7.02e-5
950	9.87e-5	2.63e-5	1.33e-5	9.02e-6	7.80e-6	8.39e-6	1.27e-5	1.23e-4	3.05e-4	3.28e-4	2.84e-4	2.27e-4	1.75e-4	1.28e-4	9.11e-5	6.42e-5
1000	8.31e-5	2.23e-5	1.11e-5	7.46e-6	6.18e-6	6.16e-6	7.94e-6	2.60e-5	1.98e-4	2.56e-4	2.38e-4	1.95e-4	1.53e-4	1.14e-4	8.27e-5	5.77e-5

Table A.3: Cross section values of the simulated m_{d_H} = 70 GeV mass point, for m_χ and $m_{Z'}$ (both in GeV) varying.

m_χ \ $m_{Z'}$	250	500	750	1000	1250	1500	1750	2000	2250	2500	2750	3000	3250	3500	3750	4000
50	4.73e-2	4.89e-2	3.77e-2	3.09e-2	2.39e-2	1.65e-2	1.09e-2	6.91e-3	4.43e-3	2.78e-3	1.76e-3	1.11e-3	6.94e-4	4.35e-4	2.74e-4	1.70e-4
100	1.73e-2	4.00e-2	3.35e-2	2.67e-2	2.15e-2	1.51e-2	1.02e-2	6.60e-3	4.24e-3	2.71e-3	1.68e-3	1.08e-3	6.89e-4	4.25e-4	2.68e-4	1.69e-4
150	9.61e-4	2.73e-2	2.78e-2	2.21e-2	1.84e-2	1.35e-2	9.29e-3	6.23e-3	3.95e-3	2.57e-3	1.63e-3	1.03e-3	6.58e-4	4.17e-4	2.62e-4	1.65e-4
200	7.73e-4	1.28e-2	2.17e-2	1.79e-2	1.51e-2	1.18e-2	8.31e-3	5.60e-3	3.73e-3	2.44e-3	1.55e-3	9.96e-4	6.33e-4	4.05e-4	2.55e-4	1.62e-4
250	6.75e-4	9.32e-4	1.51e-2	1.46e-2	1.22e-2	9.76e-3	7.21e-3	5.08e-3	3.43e-3	2.25e-3	1.46e-3	9.44e-4	6.04e-4	3.87e-4	2.47e-4	1.55e-4
300	5.87e-4	3.17e-4	8.45e-3	1.15e-2	9.76e-3	8.12e-3	6.22e-3	4.48e-3	3.12e-3	2.07e-3	1.37e-3	8.88e-4	5.74e-4	3.72e-4	2.37e-4	1.51e-4
350	5.17e-4	2.15e-4	2.26e-3	8.31e-3	7.74e-3	6.57e-3	5.24e-3	3.89e-3	2.74e-3	1.90e-3	1.25e-3	8.30e-4	5.38e-4	3.50e-4	2.21e-4	1.43e-4
400	4.47e-4	1.65e-4	2.29e-4	5.12e-3	6.12e-3	5.33e-3	4.35e-3	3.37e-3	2.45e-3	1.71e-3	1.15e-3	7.70e-4	5.04e-4	3.32e-4	2.14e-4	1.37e-4
450	3.95e-4	1.33e-4	1.22e-4	2.17e-3	4.56e-3	4.27e-3	3.58e-3	2.81e-3	2.13e-3	1.52e-3	1.05e-3	7.05e-4	4.74e-4	3.11e-4	2.00e-4	1.30e-4
500	3.42e-4	1.09e-4	8.19e-5	2.69e-4	3.05e-3	3.34e-3	2.93e-3	2.38e-3	1.84e-3	1.34e-3	9.44e-4	6.49e-4	4.40e-4	2.89e-4	1.89e-4	1.22e-4
550	2.96e-4	9.15e-5	6.12e-5	8.55e-5	1.60e-3	2.56e-3	2.38e-3	1.99e-3	1.58e-3	1.18e-3	8.42e-4	5.88e-4	4.02e-4	2.71e-4	1.79e-4	1.15e-4
600	2.57e-4	7.63e-5	4.78e-5	5.16e-5	4.44e-4	1.81e-3	1.88e-3	1.63e-3	1.33e-3	1.02e-3	7.54e-4	5.32e-4	3.65e-4	2.48e-4	1.65e-4	1.08e-4
650	2.19e-4	6.38e-5	3.75e-5	3.53e-5	7.09e-5	1.09e-3	1.47e-3	1.35e-3	1.12e-3	8.77e-4	6.63e-4	4.72e-4	3.34e-4	2.30e-4	1.53e-4	1.02e-4
700	1.89e-4	5.38e-5	3.06e-5	2.60e-5	3.54e-5	4.51e-4	1.08e-3	1.09e-3	9.44e-4	7.59e-4	5.77e-4	4.25e-4	3.03e-4	2.08e-4	1.43e-4	9.39e-5
750	1.64e-4	4.58e-5	2.51e-5	1.98e-5	2.28e-5	7.77e-5	7.08e-4	8.56e-4	7.81e-4	6.43e-4	5.06e-4	3.76e-4	2.72e-4	1.90e-4	1.30e-4	8.78e-5
800	1.41e-4	3.88e-5	2.06e-5	1.56e-5	1.58e-5	2.70e-5	3.66e-4	6.50e-4	6.37e-4	5.42e-4	4.38e-4	3.30e-4	2.43e-4	1.72e-4	1.20e-4	8.00e-5
850	1.19e-4	3.30e-5	1.72e-5	1.24e-5	1.18e-5	1.58e-5	1.09e-4	4.49e-4	5.13e-4	4.57e-4	3.70e-4	2.87e-4	2.15e-4	1.53e-4	1.09e-4	7.49e-5
900	1.02e-4	2.75e-5	1.42e-5	9.89e-6	8.88e-6	1.04e-5	2.30e-5	2.66e-4	3.98e-4	3.74e-4	3.18e-4	2.53e-4	1.90e-4	1.39e-4	9.90e-5	6.84e-5
950	8.73e-5	2.31e-5	1.17e-5	8.06e-6	6.85e-6	7.51e-6	1.15e-5	1.13e-4	2.83e-4	3.07e-4	2.72e-4	2.17e-4	1.68e-4	1.25e-4	8.92e-5	6.28e-5
1000	7.42e-5	1.98e-5	9.77e-6	6.60e-6	5.43e-6	5.52e-6	7.28e-6	2.41e-5	1.82e-4	2.42e-4	2.23e-4	1.87e-4	1.48e-4	1.11e-4	8.09e-5	5.69e-5

Table A.4: Cross section values of the simulated m_{d_H} = 90 GeV mass point, for m_χ and $m_{Z'}$ (both in GeV) varying.

m_χ \ $m_{Z'}$	250	500	750	1000	1250	1500	1750	2000	2250	2500	2750	3000	3250	3500	3750	4000
50	4.07e-2	4.23e-2	3.33e-2	2.82e-2	2.25e-2	1.57e-2	1.03e-2	6.68e-3	4.26e-3	2.69e-3	1.70e-3	1.08e-3	6.75e-4	4.28e-4	2.67e-4	1.68e-4
100	1.50e-2	3.48e-2	2.96e-2	2.42e-2	2.02e-2	1.44e-2	9.79e-3	6.37e-3	4.11e-3	2.60e-3	1.66e-3	1.05e-3	6.67e-4	4.22e-4	2.63e-4	1.66e-4
150	8.50e-4	2.44e-2	2.49e-2	2.00e-2	1.71e-2	1.28e-2	8.94e-3	5.94e-3	3.88e-3	2.49e-3	1.59e-3	1.03e-3	6.37e-4	4.12e-4	2.56e-4	1.62e-4
200	6.78e-4	1.15e-2	1.94e-2	1.63e-2	1.41e-2	1.11e-2	7.95e-3	5.44e-3	3.58e-3	2.34e-3	1.53e-3	9.78e-4	6.18e-4	3.97e-4	2.52e-4	1.57e-4
250	5.88e-4	8.41e-4	1.36e-2	1.34e-2	1.12e-2	9.25e-3	6.93e-3	4.84e-3	3.29e-3	2.18e-3	1.42e-3	9.19e-4	5.91e-4	3.80e-4	2.42e-4	1.52e-4
300	5.12e-4	2.86e-4	7.63e-3	1.05e-2	8.96e-3	7.55e-3	5.90e-3	4.33e-3	3.01e-3	2.00e-3	1.33e-3	8.65e-4	5.66e-4	3.62e-4	2.32e-4	1.46e-4
350	4.51e-4	1.93e-4	2.04e-3	7.58e-3	7.13e-3	6.17e-3	4.97e-3	3.73e-3	2.67e-3	1.83e-3	1.21e-3	8.04e-4	5.29e-4	3.45e-4	2.21e-4	1.40e-4
400	3.89e-4	1.48e-4	2.09e-4	4.67e-3	5.67e-3	4.94e-3	4.14e-3	3.20e-3	2.35e-3	1.65e-3	1.13e-3	7.49e-4	4.92e-4	3.25e-4	2.08e-4	1.35e-4
450	3.43e-4	1.19e-4	1.10e-4	1.98e-3	4.22e-3	3.95e-3	3.35e-3	2.70e-3	2.04e-3	1.45e-3	1.01e-3	6.89e-4	4.58e-4	3.06e-4	1.97e-4	1.29e-4
500	2.97e-4	9.77e-5	7.48e-5	2.43e-4	2.78e-3	3.12e-3	2.72e-3	2.26e-3	1.76e-3	1.30e-3	9.09e-4	6.26e-4	4.27e-4	2.84e-4	1.87e-4	1.21e-4
550	2.56e-4	8.14e-5	5.49e-5	7.86e-5	1.46e-3	2.38e-3	2.22e-3	1.88e-3	1.50e-3	1.14e-3	8.17e-4	5.69e-4	3.93e-4	2.63e-4	1.73e-4	1.14e-4
600	2.22e-4	6.80e-5	4.31e-5	4.69e-5	4.12e-4	1.68e-3	1.77e-3	1.54e-3	1.26e-3	9.72e-4	7.25e-4	5.15e-4	3.57e-4	2.42e-4	1.63e-4	1.06e-4
650	1.92e-4	5.73e-5	3.39e-5	3.21e-5	6.54e-5	1.00e-3	1.37e-3	1.26e-3	1.06e-3	8.38e-4	6.44e-4	4.60e-4	3.21e-4	2.21e-4	1.52e-4	9.91e-5
700	1.65e-4	4.90e-5	2.76e-5	2.36e-5	3.27e-5	4.25e-4	1.01e-3	1.02e-3	8.82e-4	7.19e-4	5.54e-4	4.07e-4	2.93e-4	2.02e-4	1.36e-4	9.25e-5
750	1.43e-4	4.11e-5	2.24e-5	1.78e-5	2.08e-5	7.24e-5	6.52e-4	7.96e-4	7.34e-4	6.16e-4	4.78e-4	3.61e-4	2.62e-4	1.85e-4	1.27e-4	8.62e-5
800	1.21e-4	3.49e-5	1.85e-5	1.40e-5	1.45e-5	2.53e-5	3.39e-4	6.01e-4	6.03e-4	5.13e-4	4.13e-4	3.17e-4	2.32e-4	1.68e-4	1.17e-4	7.93e-5
850	1.04e-4	2.94e-5	1.55e-5	1.13e-5	1.07e-5	1.45e-5	1.01e-4	4.15e-4	4.80e-4	4.31e-4	3.55e-4	2.80e-4	2.08e-4	1.51e-4	1.07e-4	7.27e-5
900	8.94e-5	2.49e-5	1.28e-5	9.01e-6	8.11e-6	9.62e-6	2.12e-5	2.47e-4	3.69e-4	3.53e-4	3.04e-4	2.41e-4	1.84e-4	1.36e-4	9.55e-5	6.61e-5
950	7.59e-5	2.12e-5	1.07e-5	7.31e-6	6.29e-6	6.76e-6	1.06e-5	1.05e-4	2.66e-4	2.87e-4	2.54e-4	2.07e-4	1.60e-4	1.20e-4	8.66e-5	6.08e-5
1000	6.50e-5	1.79e-5	8.92e-6	5.98e-6	4.93e-6	5.00e-6	6.66e-6	2.28e-5	1.71e-4	2.24e-4	2.12e-4	1.77e-4	1.41e-4	1.07e-4	7.75e-5	5.59e-5

Table A.5: Cross section values of the simulated m_χ = 200 GeV, $m_{Z'}$ = 1000 GeV mass point, for g_χ and m_{d_H} (in GeV) varying.

g_χ \ m_{d_H}	10	20	40	60	80	100	120	140	160	180	200	220	240
0.1	1.16e-6	3.31e-6	2.96e-6	2.60e-6	2.33e-6	2.10e-6	1.77e-6	1.06e-6	1.62e-7	2.06e-8	9.32e-9	5.89e-9	4.06e-9
0.2	1.84e-5	5.30e-5	4.65e-5	4.09e-5	3.68e-5	3.31e-5	2.81e-5	1.68e-5	2.55e-6	3.23e-7	1.47e-7	9.35e-8	6.42e-8
0.3	9.11e-5	2.65e-4	2.32e-4	2.04e-4	1.84e-4	1.66e-4	1.41e-4	8.31e-5	1.29e-5	1.63e-6	7.36e-7	4.62e-7	3.18e-7
0.4	2.80e-4	8.11e-4	7.13e-4	6.31e-4	5.65e-4	5.13e-4	4.34e-4	2.58e-4	3.94e-5	5.00e-6	2.27e-6	1.43e-6	9.76e-7
0.5	6.65e-4	1.91e-3	1.69e-3	1.50e-3	1.35e-3	1.21e-3	1.02e-3	6.07e-4	9.39e-5	1.19e-5	5.36e-6	3.43e-6	2.32e-6
0.6	1.31e-3	3.80e-3	3.37e-3	3.01e-3	2.68e-3	2.45e-3	2.07e-3	1.23e-3	1.88e-4	2.38e-5	1.07e-5	6.78e-6	4.70e-6
0.7	2.32e-3	6.75e-3	5.97e-3	5.32e-3	4.76e-3	4.35e-3	3.67e-3	2.16e-3	3.35e-4	4.22e-5	1.92e-5	1.23e-5	8.32e-6
0.8	3.78e-3	1.09e-2	9.84e-3	8.65e-3	7.84e-3	7.03e-3	5.95e-3	3.55e-3	5.51e-4	6.94e-5	3.14e-5	2.00e-5	1.36e-5
0.9	5.67e-3	1.65e-2	1.49e-2	1.31e-2	1.19e-2	1.07e-2	9.17e-3	5.41e-3	8.32e-4	1.06e-4	4.85e-5	3.03e-5	2.07e-5
1.0	8.16e-3	2.37e-2	2.16e-2	1.92e-2	1.73e-2	1.57e-2	1.32e-2	7.91e-3	1.21e-3	1.53e-4	6.99e-5	4.42e-5	3.02e-5
1.1	1.12e-2	3.26e-2	2.97e-2	2.64e-2	2.36e-2	2.16e-2	1.84e-2	1.08e-2	1.68e-3	2.13e-4	9.68e-5	6.13e-5	4.22e-5
1.2	1.45e-2	4.30e-2	3.94e-2	3.54e-2	3.21e-2	2.92e-2	2.46e-2	1.48e-2	2.25e-3	2.85e-4	1.29e-4	8.28e-5	5.67e-5
1.3	1.87e-2	5.52e-2	5.10e-2	4.54e-2	4.10e-2	3.78e-2	3.22e-2	1.91e-2	2.92e-3	3.73e-4	1.71e-4	1.07e-4	7.28e-5
1.4	2.36e-2	7.01e-2	6.42e-2	5.83e-2	5.25e-2	4.78e-2	4.05e-2	2.42e-2	3.77e-3	4.72e-4	2.12e-4	1.37e-4	9.24e-5
1.5	2.88e-2	8.53e-2	7.92e-2	7.16e-2	6.49e-2	5.93e-2	5.08e-2	2.99e-2	4.62e-3	5.90e-4	2.66e-4	1.71e-4	1.16e-4
1.6	3.46e-2	1.03e-1	9.61e-2	8.70e-2	7.93e-2	7.22e-2	6.14e-2	3.70e-2	5.61e-3	7.19e-4	3.24e-4	2.06e-4	1.42e-4
1.7	4.09e-2	1.22e-1	1.15e-1	1.03e-1	9.48e-2	8.65e-2	7.39e-2	4.36e-2	6.81e-3	8.61e-4	3.91e-4	2.47e-4	1.70e-4
1.8	4.76e-2	1.43e-1	1.34e-1	1.22e-1	1.12e-1	1.02e-1	8.73e-2	5.25e-2	7.98e-3	1.02e-3	4.59e-4	2.93e-4	2.00e-4
1.9	5.53e-2	1.64e-1	1.57e-1	1.43e-1	1.30e-1	1.19e-1	1.02e-1	6.14e-2	9.39e-3	1.19e-3	5.41e-4	3.40e-4	2.34e-4
2.0	6.24e-2	1.87e-1	1.77e-1	1.64e-1	1.50e-1	1.38e-1	1.18e-1	7.10e-2	1.08e-2	1.38e-3	6.26e-4	3.97e-4	2.72e-4

Table A.6: Cross section values of the simulated m_χ = 300 GeV, $m_{Z'}$ = 1500 GeV mass point, for g_χ and m_{d_H} (in GeV) varying.

g_χ \ m_{d_H}	10	20	40	60	80	100	120	140	160	180	200	220	240
0.1	4.34e-7	1.31e-6	1.24e-6	1.14e-6	1.06e-6	9.92e-7	8.71e-7	5.24e-7	8.13e-8	1.04e-8	4.79e-9	3.01e-9	2.09e-9
0.2	6.92e-6	2.07e-5	1.97e-5	1.79e-5	1.68e-5	1.57e-5	1.36e-5	8.30e-6	1.29e-6	1.65e-7	7.59e-8	4.82e-8	3.32e-8
0.3	3.42e-5	1.03e-4	9.71e-5	9.05e-5	8.35e-5	7.80e-5	6.78e-5	4.08e-5	6.34e-6	8.15e-7	3.74e-7	2.40e-7	1.65e-7
0.4	1.05e-4	3.17e-4	2.99e-4	2.77e-4	2.59e-4	2.39e-4	2.10e-4	1.26e-4	1.96e-5	2.54e-6	1.16e-6	7.44e-7	5.07e-7
0.5	2.49e-4	7.44e-4	7.02e-4	6.56e-4	6.06e-4	5.71e-4	4.96e-4	2.99e-4	4.64e-5	5.97e-6	2.77e-6	1.74e-6	1.21e-6
0.6	4.94e-4	1.48e-3	1.42e-3	1.32e-3	1.22e-3	1.14e-3	9.93e-4	5.98e-4	9.39e-5	1.21e-5	5.52e-6	3.50e-6	2.40e-6
0.7	8.68e-4	2.63e-3	2.50e-3	2.34e-3	2.17e-3	2.04e-3	1.76e-3	1.07e-3	1.66e-4	2.14e-5	9.78e-6	6.27e-6	4.29e-6
0.8	1.40e-3	4.26e-3	4.08e-3	3.78e-3	3.55e-3	3.32e-3	2.87e-3	1.75e-3	2.70e-4	3.49e-5	1.60e-5	1.02e-5	7.04e-6
0.9	2.15e-3	6.44e-3	6.20e-3	5.78e-3	5.38e-3	5.05e-3	4.39e-3	2.66e-3	4.15e-4	5.34e-5	2.43e-5	1.58e-5	1.08e-5
1.0	3.05e-3	9.37e-3	8.90e-3	8.42e-3	7.78e-3	7.32e-3	6.37e-3	3.87e-3	5.98e-4	7.74e-5	3.55e-5	2.28e-5	1.56e-5
1.1	4.20e-3	1.29e-2	1.23e-2	1.15e-2	1.08e-2	1.01e-2	8.89e-3	5.32e-3	8.40e-4	1.08e-4	4.93e-5	3.12e-5	2.16e-5
1.2	5.58e-3	1.71e-2	1.65e-2	1.55e-2	1.43e-2	1.36e-2	1.18e-2	7.20e-3	1.12e-3	1.44e-4	6.62e-5	4.21e-5	2.89e-5
1.3	7.16e-3	2.20e-2	2.12e-2	2.00e-2	1.86e-2	1.77e-2	1.53e-2	9.29e-3	1.47e-3	1.88e-4	8.57e-5	5.46e-5	3.79e-5
1.4	8.96e-3	2.76e-2	2.67e-2	2.56e-2	2.37e-2	2.23e-2	1.94e-2	1.18e-2	1.86e-3	2.38e-4	1.09e-4	6.97e-5	4.80e-5
1.5	1.11e-2	3.38e-2	3.29e-2	3.17e-2	2.98e-2	2.78e-2	2.43e-2	1.48e-2	2.29e-3	2.95e-4	1.36e-4	8.70e-5	5.97e-5
1.6	1.33e-2	4.12e-2	4.00e-2	3.81e-2	3.59e-2	3.40e-2	2.94e-2	1.79e-2	2.80e-3	3.61e-4	1.65e-4	1.05e-4	7.30e-5
1.7	1.58e-2	4.88e-2	4.76e-2	4.53e-2	4.29e-2	4.04e-2	3.54e-2	2.14e-2	3.33e-3	4.32e-4	1.99e-4	1.27e-4	8.72e-5
1.8	1.86e-2	5.64e-2	5.62e-2	5.31e-2	5.05e-2	4.76e-2	4.16e-2	2.54e-2	4.00e-3	5.10e-4	2.35e-4	1.50e-4	1.05e-4
1.9	2.18e-2	6.59e-2	6.56e-2	6.25e-2	5.96e-2	5.54e-2	4.89e-2	2.95e-2	4.66e-3	6.01e-4	2.76e-4	1.76e-4	1.21e-4
2.0	2.46e-2	7.49e-2	7.49e-2	7.09e-2	6.89e-2	6.45e-2	5.66e-2	3.41e-2	5.37e-3	6.95e-4	3.19e-4	2.05e-4	1.40e-4

Bibliography

[1] S. Weinberg, "The Making of the standard model", *Eur. Phys. J. C* **34** (2004) 5–13, doi:10.1140/epjc/s2004-01761-1, arXiv:hep-ph/0401010.

[2] A. Pich, "The Standard Model of Electroweak Interactions", in *2010 European School of High Energy Physics*, pp. 1–50. 1, 2012. arXiv:1201.0537.

[3] S. Novaes, "Standard model: An Introduction", in *10th Jorge Andre Swieca Summer School: Particle and Fields*, pp. 5–102. 1, 1999. arXiv:hep-ph/0001283.

[4] Particle Data Group Collaboration, "Review of Particle Physics", *Phys. Rev. D* **98** (2018), no. 3, 030001, doi:10.1103/PhysRevD.98.030001.

[5] W. Rolnick, "The Fundamental particles and their interactions". 10, 1994.

[6] A. Pich, "Flavour Dynamics and Violations of the CP Symmetry", *CERN Yellow Rep. School Proc.* **4** (2018) 63, doi:10.23730/CYRSP-2018-004.63, arXiv:1805.08597.

[7] S. Marzani, G. Soyez, and M. Spannowsky, "Looking inside jets: an introduction to jet substructure and boosted-object phenomenology", volume 958. Springer, 2019. doi:10.1007/978-3-030-15709-8.

[8] R. Kogler et al., "Jet Substructure at the Large Hadron Collider: Experimental Review", *Rev. Mod. Phys.* **91** (2019), no. 4, 045003, doi:10.1103/RevModPhys.91.045003, arXiv:1803.06991.

[9] "LHC Machine", *JINST* **3** (2008) S08001, doi:10.1088/1748-0221/3/08/S08001.

[10] ALICE Collaboration, "The ALICE experiment at the CERN LHC", *JINST* **3** (2008) S08002, doi:10.1088/1748-0221/3/08/S08002.

[11] ATLAS Collaboration, "The ATLAS Experiment at the CERN Large Hadron Collider", *JINST* **3** (2008) S08003, doi:10.1088/1748-0221/3/08/S08003.

[12] CMS Collaboration, "The CMS Experiment at the CERN LHC", *JINST* **3** (2008) S08004, doi:10.1088/1748-0221/3/08/S08004.

[13] LHCb Collaboration, "The LHCb Detector at the LHC", *JINST* **3** (2008) S08005, doi:10.1088/1748-0221/3/08/S08005.

[14] V. Drollinger, "Getting ready for physics at the LHC with the CMS detector", in *21st Lake Louise Winter Institute: Fundamental Interactions*, pp. 187–192. 4, 2006. arXiv:physics/0604110. doi:10.1142/9789812772541_0020.

[15] CMS Collaboration, "Precision measurement of the structure of the CMS inner tracking system using nuclear interactions", *JINST* **13** (2018), no. 10, P10034, doi:10.1088/1748-0221/13/10/P10034, arXiv:1807.03289.

[16] CMS Collaboration, "CMS Technical Design Report for the Pixel Detector Upgrade", doi:10.2172/1151650.

[17] C. Biino, "The CMS Electromagnetic Calorimeter: overview, lessons learned during Run 1 and future projections", *J. Phys. Conf. Ser.* **587** (2015), no. 1, 012001, doi:10.1088/1742-6596/587/1/012001.

[18] CMS Collaboration, "CMS Technical Design Report for the Phase 1 Upgrade of the Hadron Calorimeter", doi:10.2172/1151651.

[19] CMS Collaboration, "The CMS muon system in Run2: preparation, status and first results", *PoS* **EPS-HEP2015** (2015) 237, doi:10.22323/1.234.0237, arXiv:1510.05424.

[20] CMS Collaboration, "The CMS trigger system", *JINST* **12** (2017), no. 01, P01020, doi:10.1088/1748-0221/12/01/P01020, arXiv:1609.02366.

[21] G. Bertone and D. Hooper, "History of dark matter", *Rev. Mod. Phys.* **90** (2018), no. 4, 045002, doi:10.1103/RevModPhys.90.045002, arXiv:1605.04909.

[22] S. Profumo, "An Introduction to Particle Dark Matter". Advanced textbooks in physics. World Scientific, 2017. ISBN 9781786340009.

[23] V. Rubin, N. Thonnard, and J. Ford, W.K., "Rotational properties of 21 SC galaxies with a large range of luminosities and radii, from NGC 4605 /R = 4kpc/ to UGC 2885 /R = 122 kpc/", *Astrophys. J.* **238** (1980) 471, doi:10.1086/158003.

[24] E. Corbelli and P. Salucci, "The Extended Rotation Curve and the Dark Matter Halo of M33", *Mon. Not. Roy. Astron. Soc.* **311** (2000) 441–447, doi:10.1046/j.1365-8711.2000.03075.x, arXiv:astro-ph/9909252.

[25] M. Persic, P. Salucci, and F. Stel, "The Universal rotation curve of spiral galaxies: 1. The Dark matter connection", *Mon. Not. Roy. Astron. Soc.* **281** (1996) 27, doi:10.1093/mnras/278.1.27, arXiv:astro-ph/9506004.

[26] J. F. Navarro, C. S. Frenk, and S. D. White, "The Structure of cold dark matter halos", *Astrophys. J.* **462** (1996) 563–575, doi:10.1086/177173, arXiv:astro-ph/9508025.

[27] D. Clowe et al., "A direct empirical proof of the existence of dark matter", *Astrophys. J. Lett.* **648** (2006) L109–L113, doi:10.1086/508162, arXiv:astro-ph/0608407.

[28] WMAP Collaboration, "Nine-Year Wilkinson Microwave Anisotropy Probe (WMAP) Observations: Cosmological Parameter Results", *Astrophys. J. Suppl.* **208** (2013) 19, doi:10.1088/0067-0049/208/2/19, arXiv:1212.5226.

[29] Planck Collaboration, "Planck 2015 results. I. Overview of products and scientific results", *Astron. Astrophys.* **594** (2016) A1, doi:10.1051/0004-6361/201527101, arXiv:1502.01582.

[30] Planck Collaboration, "Planck 2018 results. VI. Cosmological parameters", arXiv:1807.06209.

[31] J. L. Cervantes-Cota and G. Smoot, "Cosmology today-A brief review", *AIP Conf. Proc.* **1396** (2011), no. 1, 28–52, doi:10.1063/1.3647524, arXiv:1107.1789.

[32] L. Baudis, "Direct dark matter detection: the next decade", *Phys. Dark Univ.* **1** (2012) 94–108, doi:10.1016/j.dark.2012.10.006, arXiv:1211.7222.

[33] S. M. Griffin et al., "Multichannel direct detection of light dark matter: Target comparison", *Phys. Rev. D* **101** (2020), no. 5, 055004, doi:10.1103/PhysRevD.101.055004, arXiv:1910.10716.

[34] XENON Collaboration, "Dark Matter Search Results from a One Ton-Year Exposure of XENON1T", *Phys. Rev. Lett.* **121** (2018), no. 11, 111302, doi:10.1103/PhysRevLett.121.111302, arXiv:1805.12562.

[35] LUX, LZ Collaboration, "Recent Results from LUX and Prospects for Dark Matter Searches with LZ", *Universe* **5** (2019), no. 3, 73, doi:10.3390/universe5030073.

[36] Y. Guardincerri et al., "DarkSide-50: status of the detector and results", *PoS* **ICHEP2016** (2016) 225, doi:10.22323/1.282.0225.

[37] SuperCDMS Collaboration, "New Results from the Search for Low-Mass Weakly Interacting Massive Particles with the CDMS Low Ionization Threshold Experiment", *Phys. Rev. Lett.* **116** (2016), no. 7, 071301, doi:10.1103/PhysRevLett.116.071301, arXiv:1509.02448.

[38] J. M. Gaskins, "A review of indirect searches for particle dark matter", *Contemp. Phys.* **57** (2016), no. 4, 496–525, doi:10.1080/00107514.2016.1175160, arXiv:1604.00014.

[39] Fermi-LAT Collaboration, G. Vianello and N. Omodei, "The First 100 LAT Gamma-Ray Bursts: A New Detection Algorithm and Pass 8", in *5th International Fermi Symposium*. 2, 2015. arXiv:1502.03122.

[40] H.E.S.S. Collaboration, "Constraints on an Annihilation Signal from a Core of Constant Dark Matter Density around the Milky Way Center with H.E.S.S.", *Phys. Rev. Lett.* **114** (2015), no. 8, 081301, doi:10.1103/PhysRevLett.114.081301, arXiv:1502.03244.

[41] MAGIC Collaboration, J. M. Paredes, "MAGIC Highlights", in *13th Frascati Workshop on Multifrequency Behaviour of High Energy Cosmic Sources*. 3, 2020. arXiv:2003.03841.

[42] ANTARES, IceCube Collaboration, "Combined search for neutrinos from dark matter self-annihilation in the Galactic Centre with ANTARES and IceCube", arXiv:2003.06614.

[43] D. Abercrombie et al., "Dark Matter Benchmark Models for Early LHC Run-2 Searches: Report of the ATLAS/CMS Dark Matter Forum", *Phys. Dark Univ.* **27** (2020) 100371, doi:10.1016/j.dark.2019.100371, arXiv:1507.00966.

[44] A. Albert et al., "Recommendations of the LHC Dark Matter Working Group: Comparing LHC searches for dark matter mediators in visible and invisible decay channels and calculations of the thermal relic density", *Phys. Dark Univ.* **26** (2019) 100377, doi:10.1016/j.dark.2019.100377, arXiv:1703.05703.

[45] J. Abdallah et al., "Simplified Models for Dark Matter Searches at the LHC", *Phys. Dark Univ.* **9-10** (2015) 8–23, doi:10.1016/j.dark.2015.08.001, arXiv:1506.03116.

[46] ATLAS Collaboration, "Search for dark matter in association with a Higgs boson decaying to b-quarks in pp collisions at $\sqrt{s} = 13$ TeV with the ATLAS detector", *Phys. Lett. B* **765** (2017) 11–31, doi:10.1016/j.physletb.2016.11.035, arXiv:1609.04572.

[47] CMS Collaboration, "Search for dijet resonances in proton–proton collisions at $\sqrt{s} = 13$ TeV and constraints on dark matter and other models", *Phys. Lett. B* **769** (2017) 520–542, doi:10.1016/j.physletb.2017.02.012, arXiv:1611.03568. [Erratum: Phys.Lett.B 772, 882–883 (2017)].

[48] CMS Collaboration, "Search for associated production of dark matter with a Higgs boson decaying to $b\bar{b}$ or $\gamma\gamma$ at $\sqrt{s} = 13$ TeV", *JHEP* **10** (2017) 180, doi:10.1007/JHEP10(2017)180, arXiv:1703.05236.

[49] CMS Collaboration, "Search for high mass dijet resonances with a new background prediction method in proton-proton collisions at $\sqrt{s} = 13$ TeV", *JHEP* **05** 033, doi:10.1007/JHEP05(2020)033, arXiv:1911.03947.

[50] CMS Collaboration, "Search for dark photons in decays of Higgs bosons produced in association with Z bosons in proton-proton collisions at $\sqrt{s} = 13$

TeV", *JHEP* **10** (2019) 139, doi:10.1007/JHEP10(2019)139, arXiv:1908.02699.

[51] ATLAS Collaboration, "Search for dijet resonances in events with an isolated charged lepton using $\sqrt{s} = 13$ TeV proton-proton collision data collected by the ATLAS detector", arXiv:2002.11325.

[52] ATLAS Collaboration, "Search for heavy particles decaying into a top-quark pair in the fully hadronic final state in pp collisions at $\sqrt{s} = 13$ TeV with the ATLAS detector", *Phys. Rev. D* **99** (2019), no. 9, 092004, doi:10.1103/PhysRevD.99.092004, arXiv:1902.10077.

[53] CMS Collaboration, "Search for dark matter particles produced in association with a Higgs boson in proton-proton collisions at $\sqrt{s} = 13$ TeV", *JHEP* **03** (2020) 025, doi:10.1007/JHEP03(2020)025, arXiv:1908.01713.

[54] V. A. Mitsou, "Overview of searches for dark matter at the LHC", *J. Phys. Conf. Ser.* **651** (2015), no. 1, 012023, doi:10.1088/1742-6596/651/1/012023, arXiv:1402.3673.

[55] A. Boveia and C. Doglioni, "Dark Matter Searches at Colliders", *Ann. Rev. Nucl. Part. Sci.* **68** (2018) 429–459, doi:10.1146/annurev-nucl-101917-021008, arXiv:1810.12238.

[56] M. Felcini, "Searches for Dark Matter Particles at the LHC", in *53rd Rencontres de Moriond on Cosmology*. 9, 2018. arXiv:1809.06341.

[57] M. Duerr et al., "Hunting the dark Higgs", *JHEP* **04** (2017) 143, doi:10.1007/JHEP04(2017)143, arXiv:1701.08780.

[58] M. Duerr et al., "How to save the WIMP: global analysis of a dark matter model with two s-channel mediators", *JHEP* **09** (2016) 042, doi:10.1007/JHEP09(2016)042, arXiv:1606.07609.

[59] A. Alves, S. Profumo, and F. S. Queiroz, "The dark $Z^{'}$ portal: direct, indirect and collider searches", *JHEP* **04** (2014) 063, doi:10.1007/JHEP04(2014)063, arXiv:1312.5281.

[60] ATLAS Collaboration, "Search for heavy particles decaying into a top-quark pair in the fully hadronic final state in pp collisions at $\sqrt{s} = 13$ TeV with the

ATLAS detector", *Phys. Rev. D* **99** (2019), no. 9, 092004, doi:10.1103/PhysRevD.99.092004, arXiv:1902.10077.

[61] ATLAS Collaboration, "Search for new resonances in mass distributions of jet pairs using 139 fb^{-1} of pp collisions at $\sqrt{s} = 13$ TeV with the ATLAS detector", *JHEP* **03** (2020) 145, doi:10.1007/JHEP03(2020)145, arXiv:1910.08447.

[62] J. Alwall et al., "The automated computation of tree-level and next-to-leading order differential cross sections, and their matching to parton shower simulations", *JHEP* **07** (2014) 079, doi:10.1007/JHEP07(2014)079, arXiv:1405.0301.

[63] T. Sjostrand, S. Mrenna, and P. Z. Skands, "PYTHIA 6.4 Physics and Manual", *JHEP* **05** (2006) 026, doi:10.1088/1126-6708/2006/05/026, arXiv:hep-ph/0603175.

[64] T. Sjöstrand et al., "An Introduction to PYTHIA 8.2", *Comput. Phys. Commun.* **191** (2015) 159–177, doi:10.1016/j.cpc.2015.01.024, arXiv:1410.3012.

[65] GEANT4 Collaboration, "GEANT4: A Simulation toolkit", *Nucl. Instrum. Meth. A* **506** (2003) 250–303, doi:10.1016/S0168-9002(03)01368-8.

[66] DELPHES 3 Collaboration, "DELPHES 3, A modular framework for fast simulation of a generic collider experiment", *JHEP* **02** (2014) 057, doi:10.1007/JHEP02(2014)057, arXiv:1307.6346.

[67] CMS Collaboration, "Search for new physics in final states with an energetic jet or a hadronically decaying W or Z boson and transverse momentum imbalance at $\sqrt{s} = 13$ TeV", *Phys. Rev. D* **97** (2018), no. 9, 092005, doi:10.1103/PhysRevD.97.092005, arXiv:1712.02345.

[68] A. Buckley et al., "LHAPDF6: parton density access in the LHC precision era", *Eur. Phys. J. C* **75** (2015) 132, doi:10.1140/epjc/s10052-015-3318-8, arXiv:1412.7420.

[69] R. D. Ball et al., "Parton distributions with LHC data", *Nucl. Phys. B* **867** (2013) 244–289, doi:10.1016/j.nuclphysb.2012.10.003, arXiv:1207.1303.

[70] M. Cacciari, G. P. Salam, and G. Soyez, "FastJet User Manual", *Eur. Phys. J. C* **72** (2012) 1896, doi:10.1140/epjc/s10052-012-1896-2, arXiv:1111.6097.

[71] M. Cacciari, G. P. Salam, and G. Soyez, "The anti-k_t jet clustering algorithm", *JHEP* **04** (2008) 063, doi:10.1088/1126-6708/2008/04/063, arXiv:0802.1189.

[72] N. Lavesson and L. Lonnblad, "Merging parton showers and matrix elements: Back to basics", *JHEP* **04** (2008) 085, doi:10.1088/1126-6708/2008/04/085, arXiv:0712.2966.

[73] J. Alwall et al., "Comparative study of various algorithms for the merging of parton showers and matrix elements in hadronic collisions", *Eur. Phys. J. C* **53** (2008) 473–500, doi:10.1140/epjc/s10052-007-0490-5, arXiv:0706.2569.

[74] CMS Collaboration, "Identification of b-Quark Jets with the CMS Experiment", *JINST* **8** (2013) P04013, doi:10.1088/1748-0221/8/04/P04013, arXiv:1211.4462.

[75] CMS Collaboration, "Identification of b quark jets at the CMS Experiment in the LHC Run 2", Technical Report CMS-PAS-BTV-15-001, CERN, Geneva, 2016. http://cds.cern.ch/record/2138504.

[76] CMS Collaboration, "Particle-flow reconstruction and global event description with the CMS detector", *JINST* **12** (2017), no. 10, P10003, doi:10.1088/1748-0221/12/10/P10003, arXiv:1706.04965.

[77] G. P. Salam, "Towards Jetography", *Eur. Phys. J. C* **67** (2010) 637–686, doi:10.1140/epjc/s10052-010-1314-6, arXiv:0906.1833.

[78] D. Krohn, J. Thaler, and L.-T. Wang, "Jet Trimming", *JHEP* **02** (2010) 084, doi:10.1007/JHEP02(2010)084, arXiv:0912.1342.

[79] "CMS Delphes card". https://cp3.irmp.ucl.ac.be/projects/delphes/browser/git/cards/delphes_card_CMS.tcl.

[80] S. Catani, Y. L. Dokshitzer, M. Seymour, and B. Webber, "Longitudinally invariant K_t clustering algorithms for hadron hadron collisions", *Nucl. Phys. B* **406** (1993) 187–224, doi:10.1016/0550-3213(93)90166-M.

[81] S. D. Ellis and D. E. Soper, "Successive combination jet algorithm for hadron collisions", *Phys. Rev. D* **48** (1993) 3160–3166, doi:10.1103/PhysRevD.48.3160, arXiv:hep-ph/9305266.

[82] CMS Collaboration, "Identification of b-Quark Jets with the CMS Experiment", *JINST* **8** (2013) P04013, doi:10.1088/1748-0221/8/04/P04013, arXiv:1211.4462.

[83] CMS Collaboration, "Identification of heavy-flavour jets with the CMS detector in pp collisions at 13 TeV", *JINST* **13** (2018), no. 05, P05011, doi:10.1088/1748-0221/13/05/P05011, arXiv:1712.07158.

[84] S. Frixione, E. Laenen, P. Motylinski, and B. R. Webber, "Angular correlations of lepton pairs from vector boson and top quark decays in Monte Carlo simulations", *JHEP* **04** (2007) 081, doi:10.1088/1126-6708/2007/04/081, arXiv:hep-ph/0702198.

[85] P. Artoisenet, R. Frederix, O. Mattelaer, and R. Rietkerk, "Automatic spin-entangled decays of heavy resonances in Monte Carlo simulations", *JHEP* **03** (2013) 015, doi:10.1007/JHEP03(2013)015, arXiv:1212.3460.

[86] "Hunting the Dark Higgs - UFO File". https://gitlab.cern.ch/darkhiggs/truth_studies/-/tree/master/signal_generation.

[87] ATLAS Collaboration, "Search for dark matter in association with a Higgs boson decaying to b-quarks in pp collisions at $\sqrt{s} = 13$ TeV with the ATLAS detector", *Phys. Lett. B* **765** (2017) 11–31, doi:10.1016/j.physletb.2016.11.035, arXiv:1609.04572.

[88] F. Febres Cordero, L. Reina, and D. Wackeroth, "W- and Z-boson production with a massive bottom-quark pair at the Large Hadron Collider", *Phys. Rev. D* **80** (2009) 034015, doi:10.1103/PhysRevD.80.034015, arXiv:0906.1923.

[89] ATLAS Collaboration, "Search for new phenomena in final states with an energetic jet and large missing transverse momentum in pp collisions at $\sqrt{s} = 13$ TeV using the ATLAS detector", *Phys. Rev. D* **94** (2016), no. 3, 032005, doi:10.1103/PhysRevD.94.032005, arXiv:1604.07773.

[90] G. Punzi, "Sensitivity of searches for new signals and its optimization", *eConf* **C030908** (2003) MODT002, arXiv:physics/0308063.

[91] T. Junk, "Confidence level computation for combining searches with small statistics", *Nucl. Instrum. Meth. A* **434** (1999) 435–443, doi:10.1016/S0168-9002(99)00498-2, arXiv:hep-ex/9902006.

[92] B. Schmidt, "The High-Luminosity upgrade of the LHC: Physics and Technology Challenges for the Accelerator and the Experiments", *J. Phys. Conf. Ser.* **706** (2016), no. 2, 022002, doi:10.1088/1742-6596/706/2/022002.